博 士 学 位 論 文

論 文 題 目　Development of Proton Range Verification Framework for Proton Therapy with Positron Emission Mammography

（陽電子マンモグラフィを用いた陽子線治療評価フレームワークの開発）

提 出 者　東北大学大学院医工学研究科

医工学専攻

氏　　名　ISLAM MD RAFIQUL

指　導　教　員	渡部　浩司	教授
審　査　委　員 （○印は主査）	○ 1　渡部　浩司	2　西條　芳文
	3　小玉　哲也	4
	5	6

TOHOKU UNIVERSITY

DOCTORAL THESIS

Development of Proton Range Verification Framework for Proton Therapy with Positron Emission Mammography

Author:
Md. Rafiqul ISLAM

Supervisor:
Prof. Hiroshi WATABE

A Dissertation Submitted in Fulfillment of the Requirements
for the Award of the Degree of Doctor of Philosophy in Biomedical Engineering

in the

Department of Biomedical Engineering
Graduate School of Biomedical Engineering
Tohoku University

August 19, 2022

TOHOKU UNIVERSITY

Abstract

Doctor of Philosophy in Biomedical Engineering

Development of Proton Range Verification Framework for Proton Therapy with Positron Emission Mammography

by Md. Rafiqul ISLAM

Radiotherapy is one of the main treatment modalities for cancer. It uses ionizing radiation to eradicate malignant tumor cells, either as a standalone treatment or in conjunction with surgery or chemotherapy. Proton therapy which has gained lots of attention in recent years, as a cancer treatment mode. Protons with different energies allow the high-dose region to conform to the tumor region. Considering the proton therapy, a major obstacle would be the uncertainties associated with the range of the proton beam, at which largest dose gradient is located. The uncertainties could be due to many factors such as; error in the estimated proton range, unexpected anatomical changes and issues with the patient or accelerator setup. A fully developed non-invasive range verification method could lead to reduced beam range uncertainties and providing a safe volume of dosage of proton therapy. Therefore, a reliable way to verify the range predicted either directly during the treatment or after the treatment, would be highly desirable for achieving the actual benefit of the proton therapy.

The goal of this thesis was to fully exploit the advantages of proton beams and enhance accuracy and precision of proton therapy by reducing range uncertainty. In order to verify the range of proton, a method for the quantitative determination of proton induced radioisotopes using a spectral analysis approach (SA) was proposed. The generated positron emitters as a result of proton interaction with major nuclei found in human tissues were quantified using the SA approach; this was investigated from both theoretical and experimental aspects. The PHITS (Particle and Heavy Ion Transport code System) Monte Carlo method was employed in this study to simulate the proton irradiation of a homogeneous, inhomogeneous slab and MIRD anthropomorphic phantoms. Positron emitting radioisotopes such as ^{15}O, ^{11}C and ^{13}N were scored for different energies. It was found, among other radioisotopes the ^{13}N produce a considerable peak near to the actual Bragg peak, whereas the ^{11}C and ^{15}O peaks are far away of that. The simulation results showed the offset distances between the generated ^{13}N peak and the actual Bragg peak with 1 to 2 mm for the homogeneous, inhomogeneous slab and MIRD anthropomorphic phantom studies, respectively. In the experimental study, a small scale prototype PEM (PEMGRAPH) system was used for detecting positron annihilated photons with 3D acquisition system. Experimental irradiation for a water-gel phantom was

performed using an azimuthally varying field (AVF) cyclotron with an 80 MeV monoenergetic pencil beam. The detected gamma rays produced there are two peaks. In addition to these two peaks, a small tail peak was observed at the end of proton beam path and vanished rather quickly.

The SA was performed based on the "analysis scheme" to the dynamic time-course activity data findings from simulations and experimental studies. For both the simulation and experimental studies the SA technique was applied to the 40 frames (from 15 to 55 minutes; considering 15 minutes after proton irradiation) to quantify the positron emitting radioisotopes and also to predict the half-life of them in the different regions of interest (ROIs). The proposed scheme successfully extracted the 3D spatial distributions of positron emitting radioisotopes, ^{15}O, ^{11}C and ^{13}N, respectively. The half-life of the SA extracted radioisotopes were confirmed by the ROIs analysis. In case of experimental data, the SA analysis confirmed the activity in the distal falloff region of proton induced ^{13}N radioisotopes. The ROIs study also confirmed that the ^{13}N radioisotope makes the highest contribution in the Bragg region. A quantitative comparison was performed between SA extracted and MC simulated radioisotopes. The results show there is no offset distance at the distal depth region between the SA extracted and the MC simulated radioisotopes along the beam direction. It is observed that the offset distances between the SA extracted ^{13}N peak and the actual Bragg peak with 1 to 2 mm, whereas the ^{11}C and ^{15}O peaks are very far away from the real Bragg peaks for the homogeneous, inhomogeneous slab and MIRD anthropomorphic phantom studies which is a good agreement with MC radioisotopes. On the other hand, when compared to the actual Bragg peak for the simulated homogeneous water-gel, the offset distance between the SA extracted ^{13}N peak from the experimental data is 3 mm. The simulated Bragg peak is very sharp, while the experimental ^{13}N peak is rather wide, indicating reasonable agreement with the simulation results. This distinct ^{13}N as well as the offset values could be used as an index for non-invasive PEM-based proton range verification using SA approach.

The SA extraction with 3D visualization showed promising results for proton induced radioisotope distribution. The proposed scheme and developed tools would be useful for the extraction and 3D visualization of positron emitting radioisotopes and in turn for proton range monitoring and verification. Future investigations into proton range monitoring for therapeutic purposes would benefit from the results obtained. It is concluded that using the developed tools, the obtained offset distance of the absolute proton range appears feasible for clinical proton fields delivered using pencil like protons beam. Further developments of the PEM system (PEMGRAPH) to facilitate an in-beam clinical trial would be recommended.

Acknowledgements

I am especially indebted to my supervisor, Professor Hiroshi Watabe, who have been supportive of my PhD studies and who worked actively to provide me with the protected academic time to pursue those goals. I would like to express immeasurable appreciation and deepest gratitude to Dr. Mehrdad Shahmohammadi Beni (JSPS fellow, CYRIC, Tohoku University) for his advice and help in completing my PhD project.

I would like to thank Mr. Masayasu Miyake for supporting me a lot during experiments and all other activities.

I thank all my lab mates for their advice, comments, participation and support within the lab. I wish to thank all the staffs of Radiation Informatics for Medical Imaging laboratory as well as Cyclotron and Radioisotopes Center (CYRIC) and Graduate School of Biomedical Engineering (BME) at Tohoku University for their cooperation especially in case of dealing with Japanese documents and computer troubleshooting.

Special acknowledgment to the Ministry of Education, Culture, Sports, Science and Technology (MEXT), Japanese Government for providing me with the scholarship to study in Japan and experience Japanese culture.

I wish to thank Bangladesh Atomic Energy Commission authorities and all of my colleagues specially to Dr. Mahabubur Rahman, Dr. Shahidul Islam for their cooperation at the starting time of my PhD in Japan. As well, I am grateful for the advice and encouragement of Prof. A.K. Fazlul Haque (visiting research professor, CYRIC, Tohoku University), Department of Physics, University of Rajshahi.

One a more personal level, I would like to thank my family, in particular my parents and brothers for their consistent supports and encouragements for this higher studies. I also want to thank my wife Jannatul Ferdous my beloved daughters for their sweet love and company here in Japan. Special thanks to my Father-in-law and Mother-in-law for their encouragement.

Last but not least, I want to express my sincere thanks to Ms. Watanabe, secretary of BME, TU, for the support and assistance with all our administration problems during all these four years in Japan.

Contents

Abstract **iii**

Acknowledgements **v**

Contents **ix**

List of Figures **xiii**

List of Tables **xv**

Abbreviations **xv**

1 Introduction **1**

1.1 Overview of cancer treatment 1
1.1.1 Cancer 1
1.1.2 Treatment modalities 2
1.2 Protons for cancer treatment 3
1.2.1 Proton therapy 3
1.2.2 Physical concept of proton therapy 4
1.2.3 Nuclear reactions in proton therapy 6
1.3 Range verification in proton therapy 11
1.3.1 Proton range 11
1.3.2 Range uncertainties 12
1.3.3 Range verification techniques 13
1.4 Positron emission tomography for range verification 15
1.4.1 Basic concept of PET 15
1.4.2 Particle therapy-PET 17
1.4.3 Positron emission mammography 19
1.5 Monte Carlo simulations 24
1.5.1 Monte Carlo simulations in proton therapy 24
1.6 Spectral Analysis approach 26
1.7 Motivation and objectives of the thesis 27
1.8 Structure of the thesis 28

2 Simulation of positron emitting radioisotopes during proton therapy 31
2.1 Monte Carlo simulation of positron emitting radioisotopes 31
2.2 PHITS Monte Carlo code 32
2.2.1 PHITS structure 33
2.2.2 PHITS GUI for simulation of positron emitting radioisotopes 35
2.3 Phantom irradiation for positron emitting radioisotopes 36
2.3.1 Simulation in a homogeneous phantom 37
2.3.2 Simulation in an inhomogeneous phantoms 39
Inhomogeneous slab phantom 39
MIRD anthropomorphic phantom 40
2.4 Results and discussion 41
2.4.1 Homogeneous phantom: 42
Depth dose profile 43
Depth activity profile 44
Bragg peak offset 50
2.4.2 Inhomogeneous phantoms: 52
Depth dose and activity profiles 52
2.5 Conclusions 58

3 Detection of positron annihilation photons by PEM 59
3.1 Device for detecting positron annihilation photons 59
3.2 Dual-head PEM 60
3.2.1 Experiments with homogeneous water-gel phantom 62
3.3 Results and discussion 64
3.3.1 Homogeneous water-gel phantom 64
3.4 Conclusions 66

4 Quantification of proton induced radioisotopes using SA approach 67
4.1 Spectral Analysis approach 67
4.2 Application of the SA approach in proton therapy 68
4.2.1 Scheme for extraction and 3D visualization of positron emitting radioisotopes 69
4.3 Results and discussion 71
4.3.1 Simulation studies 71
4.3.2 Experimental studies 79
4.4 Conclusions 81

5 Quantitative comparison and proton range verification 83
5.1 Quantitative comparison 83
5.1.1 Comparison between simulated and SA results 83

5.1.2 Comparison between experimental and SA results 86
5.2 Conclusions 88

6 Conclusions and future prospects **89**

Bibliography **91**

A Input codes **99**
A.1 Homogeneous phantom 99
A.2 Inhomogeneous slab phantom 101
A.3 MIRD anthropomorphic phantom 105
A.4 PeakCalib 119
A.5 Scripts 126

B Research achievements **133**
B.1 Journal papers 133
B.2 Conference abstracts and presentations 134

List of Figures

1.1 Comparison of the depth dose profiles for different beams 4
1.2 Stopping power of protons in water 5
1.3 A MC simulated Bragg peak positron emitters of 58 MeV protons on a PMMA target 9
1.4 Nuclear reaction cross sections of ^{11}C, ^{15}O, and ^{13}N from the different resources 10
1.5 Cross sections data of JENDL 11
1.6 Correlation between particle fluence and dose; range-energy relationship 12
1.7 Illustration the principal of the PET acquisition 17
1.8 Mounted PET system in the proton treatment room 18
1.9 PEM-I system with schematic weighted backprojection 20
1.10 Illustration of the LBNL PEM scanner 22
1.11 Illustration of the full-scaled PEMGRAPH 23
1.12 Illustration of the newly developed PEM by MIRAI and PEMGRAPH 24

2.1 A map of the physics models and data libraries recommended for use in PHITS 32
2.2 The illustration of the input parameters for the PHITS code using a txt-file 34
2.3 Basic of PHITS geometries 34
2.4 Different types of geometrical mesh of the PHITS Tally 34
2.5 PHITS input generator GUI for proton irradiation 35
2.6 Test case 1: for dose deposition radioisotopes production using PHITS GUI 36
2.7 A homogeneous water-gel phantom with 3D visualization was irradiated with monoenergetic proton beam. 37
2.8 A three-dimensional schematic view of a inhomogeneous slab phantom. 40
2.9 The modeled MRID anthropomorphic phantom with tumor location. 41
2.10 The normalized 1D profile of the fluence and the LET for the 80 MeV proton beam 42

2.11 Track of particles in the water-gel for 80 MeV of incident proton energy 43
2.12 The 1D, 2D, and 3D dose distribution with depth for 80, 160, and 240 MeV incident proton energies, respectively 44
2.13 The 1D normalized distribution of positron emitting radioisotopes for 80, 160, and 240 MeV incident proton energies. 46
2.14 The 2D and 3D distributions of positron emitting radioisotopes immediately after proton irradiation (i.e., t = 0) for only 80 MeV incident proton energy. 47
2.15 The 2D (left column) and 1D (right column) time-course activity in a range of 15 to 55 minutes of positron emitters in the homogeneous phantom only for 80 MeV proton energy 48
2.16 The 1D and 2D dose and activity profile with depth for a spread-out Bragg peak 49
2.17 Bragg peak and ^{13}N peak location in water-gel phantom with offset distance for 80, 160, and 240 MeV incident proton energies. 52
2.18 The 1D and 2D profiles of the depth dose and positron emitting radioisotopes for inhomogeneous slab phantom for pristine and SOBP distributions. 53
2.19 1D and 2D profiles of the depth dose and positron emitting radioisotopes for MIRD anthropomorphic phantom. 55
2.20 The 2D and 1D time-course activity profiles in a range of 15 to 55 minutes of positron emitters in the inhomogeneous phantom for pristine and SOBP distributions. 56
2.21 The 2D and 1D time-course activity profiles in a range of 15 to 55 minutes of positron emitters in the inhomogeneous phantom for pristine and SOBP distributions. 57

3.1 Illustration of the prototype PEMGRAPH system with detector components 60
3.2 The schematic view of data acquisition system. 61
3.3 The PEMGRAPH system network, schematic view and the real one . 61
3.4 The PEM heads and an HPDE box containing water-gel are depicted in this schematic diagram. 62
3.5 Experimental setup for water-gel phantom irradiation and scanning the irradiated phantom using a dual-head PEMGRAPH system. . . . 63
3.6 Reconstructed 3D and 2D PEMGRAPH images 64
3.7 The 1D, 2D, and 3D time-course activity covering 15 to 55 minutes data sets obtained from the PEMGRAPH measurements 65

4.1 An illustration of the four regions of interest (ROIs) 69
4.2 The 1D, 2D, and 3D profiles of SA extracted radioisotopes for the homogeneous phantom that irradiated with 80 MeV pristine proton beam 72
4.3 The 1D, 2D, and 3D profiles of SA extracted radioisotopes for the homogeneous phantom irradiated with SOBP filed. 73
4.4 The 1D, 2D, and 3D profiles of SA extracted radioisotopes for the inhomogeneous phantom irradiated with 80 MeV beam 73
4.5 The 1D, 2D, and 3D profiles of SA extracted radioisotopes for the inhomogeneous phantom irradiated with SOBP filed 74
4.6 The 1D, 2D, and 3D profiles of SA extracted radioisotopes for the MIRD anthropomorphic phantom. 74
4.7 The spectral analysis (SA) results for different ROIs of the homogeneous phantom for pristine and SOBP. 76
4.8 The spectral analysis (SA) results for different ROIs of the inhomogeneous phantom for pristine and SOBP. 77
4.9 The spectral analysis (SA) results for different ROIs of the MIRD anthropomorphic phantom. 78
4.10 The 1D, 2D, and 3D profiles of SA extracted radioisotopes for the PEMGRAPG measured data of the homogeneous water-gel phantom irradiated with 8o MeV beam. 80
4.11 The spectral analysis (SA) results for different ROIs of the PEMGRAPH measured data. 80

5.1 Comparisons of the 1D profiles between the MC simulated and SA extracted radioisotopes and dose of homogeneous phantom for pristine and SOBP distributions 84
5.2 Comparisons of the 1D profiles between the MC simulated and SA extracted radioisotopes and dose of inhomogeneous slab phantom for pristine and SOBP distributions 85
5.3 Comparison of the 1D profiles between the MC simulated and SA extracted radioisotopes and dose of MIRD anthropomorphic phantom 86
5.4 Comparison of the 1D profiles between the MC simulated dose and SA extracted radioisotopes of the PEMGRAPH measurement. 87
5.5 A 2D comparison the SA extracted (SA_^{11}C, SA_^{15}O and SA_^{13}N) radioisotopes. 88

A.1 ^{13}N and Bragg-peak offset distance 120

List of Tables

1.1 The most important reaction channels of positron emitters in proton therapy 8

2.1 Material composition and density of the homogeneous water-gel phantom (weight %). 38
2.2 Material composition and density of the inhomogeneous slab phantom (weight %). 40
2.3 Material composition and density of the MIRD anthropomorphic phantom (weight %) [Goldstone, 1990]. 41
2.4 Proton range for the three different incident energies in water-gel. . . 43
2.5 Comparison between actual Bragg peak and ^{13}N peak location in water-gel phantom with offset distance 51

3.1 Material composition and density of the HDPE container and water-gel used in the experiment. 62

List of Abbreviations

AVF	**A**zimuthally **V**arying **F**ield
ASCII	**A**merican **S**tandard **C**ode for **I**nformation **I**nterchange
CT	**C**omputed **T**omography
DICOM	**D**igital **I**maging and **C**ommunications in **M**edicine
DNA	**D**eoxyribo**n**uclei**a**cid
DOI	**D**epth **o**f **I**nteraction
EBRT	**E**xtrarnal **B**eam **R**adiation **T**herapy
FDG	**F**luoro**d**eoxy**g**lucose
FOV	**F**ield **o**f **V**iew
GUI	**G**raphical **U**ser **I**nterface
HDPE	**H**igh **D**ensity **P**oly**e**thylene
ICRU	**I**nternational **C**ommission on **R**adiation **U**its
IMPT	**I**ntensity **M**odulated **P**roton **T**herapy
IORT	**I**ntra-**O**perative **R**adiation **T**herapy
KE	**K**inetic **E**nergy
LET	**L**inear **E**nergy **T**ransfer
LOR	**L**ine **o**f **R**esponse
MC	**M**onte **C**arlo
MLEM	**M**aximum **L**ikelihood **E**xpectation **M**aximization
MRI	**M**agnetic **R**esonance **I**maging
NIST	**N**ational **I**nstitute of **S**tandards and **T**echnology
PEM	**P**ositron **E**mission **M**ammography
PET	**P**ositron **E**mission **T**omography
PGI	**P**rompt **G**amma-ray **I**maging
PHITS	**P**article and **H**eavy **I**on **T**ranport code **S**ystem
PMMA	**P**oly**m**ethyl**m**etha **a**crylate
PT	**P**roton **T**herapy
PTV	**P**rimary **T**arget **V**olume
PT-PET	**P**article **T**herapy- **P**ositron **E**mission **T**omography
PS-PMT	**P**osition **S**ensitive **P**hoto **M**ultiplier **T**ube
PTCOG	**P**article **T**herap **C**o-**O**perative **G**roup
RBE	**R**elative **B**iological **E**ffectiveness

ROI	**R**egion **o**f **I**nterest
RT	**R**adiation **T**herapy
SA	**S**pectral **A**nalysis
SOBP	**S**pread-**o**ut **B**ragg **P**eak
TAC	**T**ime **A**ctivity **C**urve
1D	**O**ne **D**imensional
2D	**T**wo **D**imensional
3D	**T**hree **D**imensional

"This work is dedicated to my academic supervisor Prof. Hiroshi Watabe who taught me how to finish a hard work in a simple way"

Chapter 1

Introduction

1.1 Overview of cancer treatment

1.1.1 Cancer

Cancer is expected to become a more common cause of illness and fatality in most parts of the world. Even if present worldwide cancer rates remain stable over the next two decades, the predicted incidence of 12.7 million new cancer cases in 2008 will rise to 21.4 million by 2030, owing to projected changes in population demography [Ferlay et al., 2013]. Cancer treatments are being continuously improved, thanks to the ongoing research and development in the field. However, in 2020 an estimated 9.0 million deaths due to cancer are the second leading cause of death in the world after heart disease [Sung et al., 2021].

Actually, the origin and advancement of cancer depend on many factors inside the cell (mutations, immune conditions, and hormones) as well as external factors from the environment (smoking, chemicals, infectious organism, and radiations). In realistic situations, all these factors would contribute abnormal cell behavior and uncontrolled proliferation. Cancer can be defined as a disease in which a group of abnormal cells grow uncontrollably against the normal rules of cell division. Generally, human cells are renewed at a moderate rate by controlling their division and death with a complex system of biological signals. However, mutations of the DNA (Deoxyribonucleic acid) may occur from time to time due to environmental factors, viruses, or errors during the DNA replication [Friedberg, 2003]. These mutations may have no effect or may cause the cell to function abnormally. In particular, the mutation can disrupt the system that controls cell division, triggering a malignant process. The affected cell can divide indefinitely, proliferating and developing a tumor, which is a cluster of cancerous cells. Some malignant cells have the ability to spread and migrate throughout the body, resulting in distant secondary tumors known as metastasis.

1.1.2 Treatment modalities

The treatment of cancer includes one or more treatment modalities based on the type of cancer, its location, and stage of progression. Cancer treatment modalities can be divided into two categories: conventional and advanced (i.e., new or modern). Surgery, radiation-based surgical knives, chemotherapy, and radiotherapy are some of the traditional and most widely used treatment methods. Some of the modern modalities include hormone-based therapy, anti-angiogenic modalities, stem cell therapies, immunotherapy, and dendritic cell-based immunotherapy [Charmsaz et al., 2019]. These treatments are employed against the cancer of the cerebrum, prostate, lung, breast, colorectal, pancreatic, liver, head and neck, bladder, skin, ovarian, and renal malignancy [Dorai et al., 2004].

Radiotherapy or Radiation Therapy (RT) is one of the most successful treatment options for cancer, alongside surgery and/or chemotherapy. Radiotherapy uses high doses of ionizing radiation to induce damage to the DNA of cancer cells, which ultimately leads to death of cancer cell. Radiotherapy plays an essential role in cancer management with around 50% patients receiving RT at a certain point of their treatment [Abdel-Wahab et al., 2021]. The delivery of radiation therapy can be subdivided in multiple categories. For internal radiotherapy called brachytherapy, the source of radiation is placed inside the patient, whereas for external beam radiation therapy (EBRT), the target is irradiated using a beam of radiations generated outside the patient. Different types of ionizing radiations/particles would be used in the external radiotherapy. Uses photons or electrons as primary source of radiation; this is the most used technique throughout the world. Intra-operative radiation therapy (IORT) is an another treatment technique in which a high radiation dose is given directly to the tumor or tumor bed during a surgery. IORT is frequently used in conjunction with EBRT or chemotherapy for breast cancer [Hensley, 2017; Islam et al., 2020].

Despite technological advances, such as image guidance to monitor the patient anatomy in conventional radiotherapy, photons are limited by their depth dose distribution. As a result, a continuous exponential attenuation results after an initial maximum at a shallow depth. To overcome these limitations, heavy charged particles like carbon ions and protons can be regarded as an advanced form of RT, which is meanwhile widely developed and used in state-of-the-art centers.

1.2 Protons for cancer treatment

1.2.1 Proton therapy

The goal of radiotherapy is to maximize the dose to malignant cells while minimizing exposure to healthy cells. Cancer treatment with protons offers a number of significant advantages over conventional treatment with x-rays or electron beams shown in Figure 1.1. Protons penetrating a medium, lose energy through Coulombic and nuclear interactions. Protons of a given energy have a finite and well-defined range in water and tissue, whereas the range of x-rays is theoretically infinite and poorly defined. While other ions like ^{12}C have a tail after the Bragg peak, protons do not, since only target fragmentation occurs in collisions between protons and other atoms. The rate of energy loss is most rapid in the last few millimeters of penetration. As protons traverse matter such as a column of water or the body of a patient, their kinetic energy decreases, and the dose deposition rate increases. The kinetic energy of the proton is lowest at the end of its range, while there is a sharp increase in dose deposition, known as the Bragg peak, just before the beam stops. This is followed by a sharp dose falloff distal to the Bragg peak. The penetration depth of the Bragg peak is directly related to the initial energy of the charged particle. For irradiation of a tumor, the proton beam energy and intensity are varied to distribute the Bragg peak over the whole tumor volume.

The history of proton therapy began in 1946 when Robert Wilson published a paper in which he proposed to use accelerator-produced beams of protons to treat deep-seated tumors in humans [Wilson, 1946]. The first patient treatments were performed during the 1950s at the Lawrence Berkeley Radiation Laboratory [Tobias et al., 1958]. However, it was not until 1990 that the first hospital-based proton facility in Loma Linda University, USA, was created. Since then, the number of therapy centers has increased steadily. The creation of a dedicated hospital-based proton facility was the milestone motivating the expansion of facilities and patient treatments around the world, which gathered the attention of the radiation oncology community [Das et al., 2015]. According to the Particle Therapy Co-Operative Group (by June 2021 of ***PTCOG***) there are about 96 active facilities providing treatments using protons and approximately 30 under construction and meanwhile 13 with carbon ions, some of which are combined facilities for both carbons and protons, all over the world.

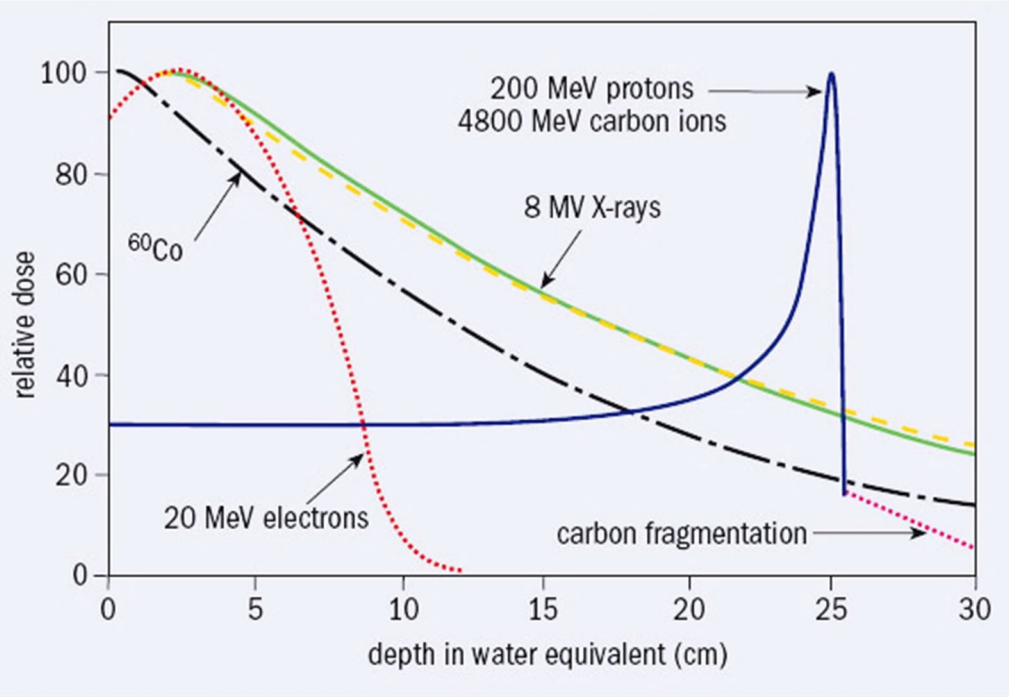

Figure 1.1: Comparison of the depth dose profiles for electron, photon, ^{60}Co, proton, and carbon beams [Amaldi et al., 2006].

1.2.2 Physical concept of proton therapy

The most important interactions of particles with the matter are actually well defined by physics models [Newhauser et al., 2015]. The characteristics of electromagnetic and nuclear interactions of the projectiles with the target medium determine the favourable dose deposition of proton for radiotherapy, presenting a peak that can be used to deliver conformal dose to a tumor while sparing surrounding tissues (see Figure 1.1). This part covers the fundamentals of physical interactions, emphasizing the components that have the greatest impact on therapy.

Electromagnetic Coulomb interactions occur when protons traverse matter, resulting in a continuous loss of kinetic energy. These interactions lead to the ionization and excitation of atoms and set free electrons that ionize other atoms in the neighborhood. Although the protons lose little energy and almost no deflection in these individual interactions, they experience thousands of interactions per centimeter [Goitein, 2007]. The rate at which they lose energy, transferring it to the tissue, increases with the penetration depth and is described by the mass stopping power. The total stopping power of protons shown in Figure 1.2 consists of electronic, nuclear and radiative stopping power. For proton therapy, the nuclear

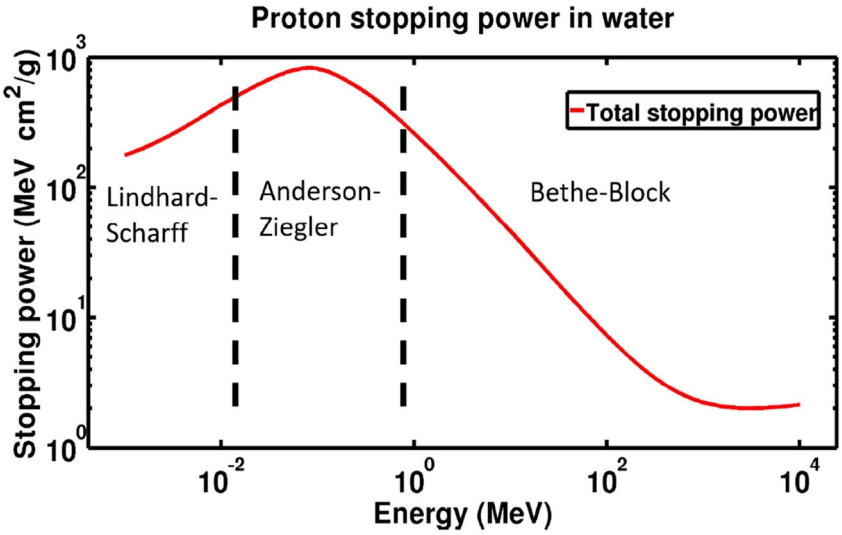

Figure 1.2: Stopping power of protons in water as a function of the kinetic energy made using NIST data, last updated in July 2017 [Berger et al., 2017].

and radiative stopping power are negligible. The electronic stopping power is described by the well-known Bethe-Bloch equation (valid only for energies higher than 1 MeV/u):

$$\frac{S_{el}}{\rho} = -4\pi N_A \tau_e^2 m_e c^2 \frac{Z}{A}\frac{z^2}{\beta^2}[ln\frac{2m_e C^2\gamma^2\beta^2}{I} - \beta^2 - \frac{\delta}{2} - \frac{C}{Z}] \tag{1.1}$$

in which S_{el} is the linear electronic stopping power, which describes the average rate at which protons lose energy dE per unit path length dx due to inelastic interactions with the atomic electrons:

$$\frac{S_{el}}{\rho} = \frac{dE}{dx}[MeVcm^{-1}] \tag{1.2}$$

and where ρ is the density of the material, N_A is the Avogadro number, τ_e is the classical electron radius, m_e is the electron mass, Z is the atomic number of the medium, A is the atomic mass number, c is the speed of light, z is the charge of the particle ($z = 1$ in the case of proton), β is a kinetic term equal to v/c, where v is the velocity of the incident particle, $\gamma = (1-\beta^2)^{-1/2}$ is the Lorentz factor, I is the mean excitation energy of the medium, δ and C are absorber dependent density and shell corrections respectively. When the protons slow down, i.e. β is comparable to the velocity of the orbital electrons, the Bethe-Bloch equation is no longer valid to predict the stopping power. In this region, so-called Lindhard region, the energy loss is proportional to the β, and can be described by the model of Anderson and Ziegler [Ziegler et al., 1985].

The *dose* (Gy) can be defined by the average energy dE (J) absorbed per unit mass $dm(kg)$:

$$dose = \frac{dE}{dm} \tag{1.3}$$

In most practical conditions secondary electron equilibrium prevails, that means the energy carried in and out of a volume of interest by secondary electrons is on average the same. Under this assumption the macroscopic *dose* can be linked to the particle fluence spectrum times the mass stopping power, integrated over the entire energy range:

$$dose = \sum_i \frac{\Phi_{E,i}}{\rho}(\frac{dE_i}{dx})dE \tag{1.4}$$

where the $\Phi_{E,i} = \frac{d\Phi_i}{dE}$ is the fluence spectrum of all primary and secondary i-th heavy charged particles (mostly protons). The amount of energy loss is a function of the incident proton particle's kinetic energy therefore, when the proton traverses a medium, its energy loss is often quantified as the linear energy transfer (LET). The linear energy transfer (LET), $(L_\Delta, keV/\mu m)$, depending on the material as well as the type and energy of the incident charged particle, is given by:

$$L_\Delta = \frac{dE_\Delta}{dx} \tag{1.5}$$

where L_Δ is the mean energy lost due to electronic interactions in traversing the distance dx, minus the kinetic energies in excess of Δ of all electrons released by the incident particle. LET is a characteristic related to the radiation type that describes the energy deposited per unity of distance and is commonly used to compare biological effects from different radiation types [Kraft et al., 1992]. The relative biological effectiveness (RBE) increases as LET increases near the end range of the incident proton [Paganetti et al., 2002]. RBE is the ratio of a dose of photons to a dose of any other incident particle to produce the same biological effects like cell killing, tissue damage, and mutations. RBE is defined as:

$$RBE = \frac{D_i}{D_\gamma} \tag{1.6}$$

where D_i and D_γ are the absorbed dose of the incident particle beam and photon radiation that causes the same amount of biological damage, respectively.

1.2.3 Nuclear reactions in proton therapy

As discussed in the above sections protons lose their energy mainly via Coulomb interactions with atomic electrons. Anyway, also nuclear interactions between the proton and the irradiated target take place in proton therapy. Incident protons can

interact with atomic nuclei via the nuclear force, resulting in a reduction of the primary fluence. The target can break up, be excited, or yield a particle transfer reaction.

There are three types of nuclear interaction: **elastic, nonelastic and inelastic**. In an elastic interaction total kinetic energy is conserved and target nuclei and projectile are unchanged by the reaction. Such interactions hardly influence the beam. In nonelastic and inelastic interactions total kinetic energy is not conserved. While in inelastic interactions final nucleus are the same as the bombarded nuclei in nonelastic reactions the target can undergo breakup and produce non-stable isotopesor can be excited in higher quantum state.

For describing the probability of projectile-target inelastic nuclear reactions, the reaction cross section σ_R must be known. Considering an initial number N_0 of particles impinging on a slab of thickness x, the expected number of particles exiting the absorber follows the usual exponential law, $N(x) = N_0 e^{-x/\lambda}$, where the mean free path λ is related to the cross section via the relation:

$$\lambda = \frac{M_{mol}}{N_a \rho \sigma_R} \tag{1.7}$$

In the latter equation also dependences on target density ρ, and molecular mass M_{mol}, are present (N_a is the Avogadro number). Due to their importance in nuclear physics, reaction cross sections have been extensively measured in the last decades and various parametrizations are available. One of the most convenient is a modified version of the Bradt-Peters equation, which is a good representation of the observed total reaction cross section [Sihver et al., 1993].

$$\sigma_R = \pi r_0^2 c_1(E)[A_p^{1/3} + A_t^{1/3} - c_2(E)]^2 \tag{1.8}$$

where A_p and A_t are the atomic masses of projectile and target, r_0 is a fixed parameter and c_1; c_2 are energy dependent parameters. This expression indicates that, for a given projectile, the cross section increases for increasing target atomic mass. For high-energy protons the equation Eq. 1.8 can be further simplified [Bichsel, 2013].

$$\sigma \approx 53. A_t^{2/3} mb. \tag{1.9}$$

Thus, if a water target is considered, the resulting mean free path for proton with an energy of hundreds of MeV is $\lambda \approx 82.0$ cm, meaning that more than 20% of the protons in the terapeutic beam undergo nuclear interactions in a deep tumor treatment case, i.e., when the beam crosses an equivalent thickness of $\sim$20.0 cm of water [Tommasino et al., 2015].

Table 1.1: The most important nuclear reaction channels for the creation of positron emitters in proton therapy [Kitwanga et al., 1989; Zhu et al., 2013].

Isotope	Half-life (minutes)	Reaction Channel	Threshold energy (MeV)
^{11}C	20.383	^{12}C(p,pn)^{11}C	20.61
		^{16}O(p,3p3n)^{11}C	59.64
		^{14}N(p,2p2n)^{11}C	3.220
^{10}C	0.317	^{12}C(p,p2n)^{10}C	35.00
		^{16}O(p,3p4n)^{10}C	72.00
^{15}O	2.032	^{16}O(p,pn)^{15}O	16.79
^{13}N	9.936	^{16}O(p,2p2n)^{13}N	5.560
		^{14}N(p,pn)^{13}N	11.44
^{30}P	2.498	^{31}P(p,pn)^{30}P	19.70
^{38}K	7.636	^{40}Ca(p,2p2n)^{38}K	21.20

Nuclear interactions products have a wide range of therapeutic implications. In reality, secondary fragments contribute to the overall dose, distorting the SOBP and charged fragments enhance significantly the RBE modifying. Furthermore, nuclear processes can generate neutrons, which can deposit a dose outside the treatment volume. Finally, secondary emissions can be recognized, and beam-delivery information can be collected. Since, the PET (Positron Emission Tomography) technology also known as Particle Therapy Positron Emission Tomography (PT-PET) is used in this study, the emphasis is on the creation of positron emitter unstable isotopes. It is useful to know which nuclear reactions the positron emitters cause in order to comprehend their creation in terms of location and abundance. The most frequently generated positron emitter isotopes in a human body treated with proton therapy, as well as their half-lives, production thresholds, and reaction channels, are shown in Table 1.1. Depending on their decay time, these isotopes emit positrons that annihilate in the body, resulting in two back-to-back gammas that can be detected with a PET detector. The relationship between the deposited dose and the activity of the isotopes produced is difficult, because dose deposition and nuclear reactions are dependent on proton energy and material composition in fundamentally different ways are shown in Figure 1.3. The distal end of the 1D activity profile (i.e., the projection of the generated activity along the beam axis) will be less deep than the depth dose profile, because the creation of positron emitters is a threshold process.

During PT, many isotopes are produced through different nuclear reactions. When protons are introduced into a human body which is mainly composed of Oxygen (65.0%), Carbon (18.0%), Hydrogen (10.0%), Nitrogen (3.0%), Calcium (1.4%), Phosphorus (1.1%), Potassium (0.2%) and others (1.3%) nuclei they react with all

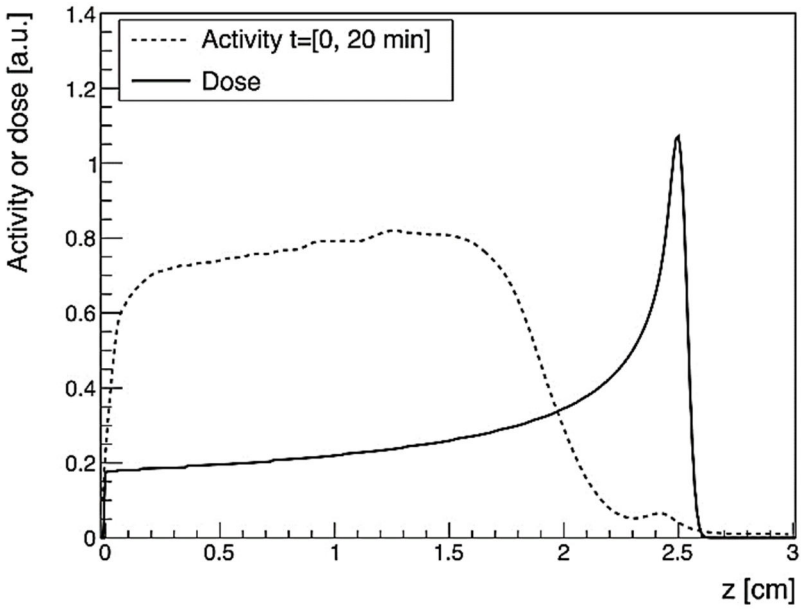

Figure 1.3: A MC simulated representation of the relation between the Bragg peak and positron emitters of 58 MeV protons on a PMMA target [Kraan et al., 2014].

elements which can result in the production of positron emitter isotopes (^{10}C, ^{11}C, ^{13}N, ^{14}O, ^{15}O, ^{38}K, ^{38}Ca, and ^{39}Ca). Among them the ^{11}C, ^{13}N, and ^{15}O are the three main positron emitters produced and is important to estimate the range and exposure dose distribution in the patient's body. The cross sections of ^{11}C, ^{13}N, and ^{15}O were measured at several proton energies. On the other hand, due to the very small quantities of production the cross sections of (^{10}C, ^{14}O, ^{38}K, and ^{39}Ca) were measured only at few points. If the incoming proton beam flux and target density are fixed, the positron emitters production is determined by the cross section data. Though, the cross section data are limited but several resources ICRU-63 [Malmer, 2001], [EXFOR], TERA [Mukhopadhyay et al., 1995], [JENDL], and others provided important data that are used by the researchers[Beebe-Wang et al., 2002, Parodi et al., 2001, Del Guerra et al., 1994 and Litzenberg, 1997] so on, as shown in Figures 1.4 and 1.5, respectively.

Table 1.1 shows a brief summary of the data availability of the main cross sections or production yields. Here one can see how there are some reactions that have been sufficiently measured, e.g. ^{16}O(p,2p2n)^{13}N or ^{12}C(p,pn)^{11}C. However, from the Figures 1.4 (c) and 1.5, it is observed that the ^{16}O(p,2p2n)^{13}N interaction cross section has a relatively low energy threshold ($\sim$9 MeV) and exhibits a narrow peak at around 12 MeV. At these energies the residual proton range is only few millimeter. This is a distinct property that distinguishes it from the others, given that all other interaction cross sections have broad peaks with interaction energy thresholds of

approximately 20 MeV or higher. This study focused on proton range verification by extracting the ^{13}N peak following the ^{16}O(p,2p2n)^{13}N interaction cross section using a spectral analysis approach from the Monte Carlo simulations data and the experimental measurement of highly sensitive Positron Emission Mammography (PEM) system.

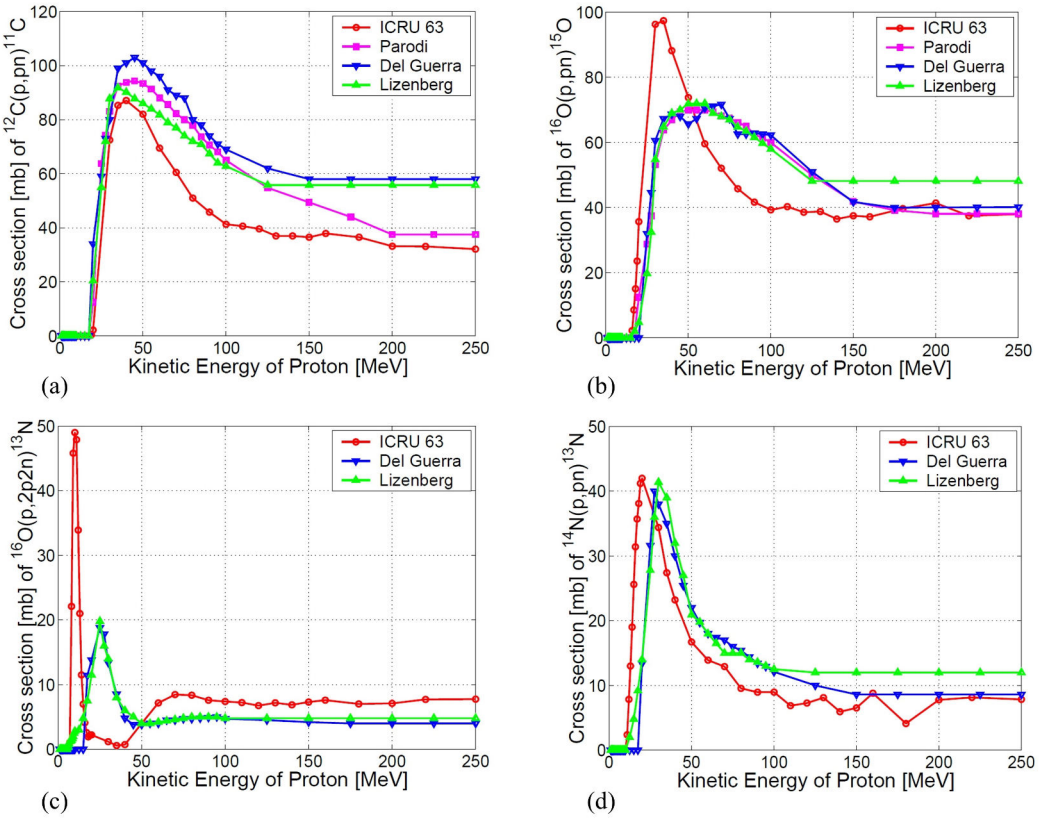

Figure 1.4: Nuclear reaction cross sections of (**a**) ^{12}C(p,pn)^{11}C, (**b**) ^{16}O(p,pn)^{15}O, (**c**) ^{16}O(p,2p2n)^{13}N, and (**d**) ^{14}N(p,pn)^{13}N are presented from the different resources.

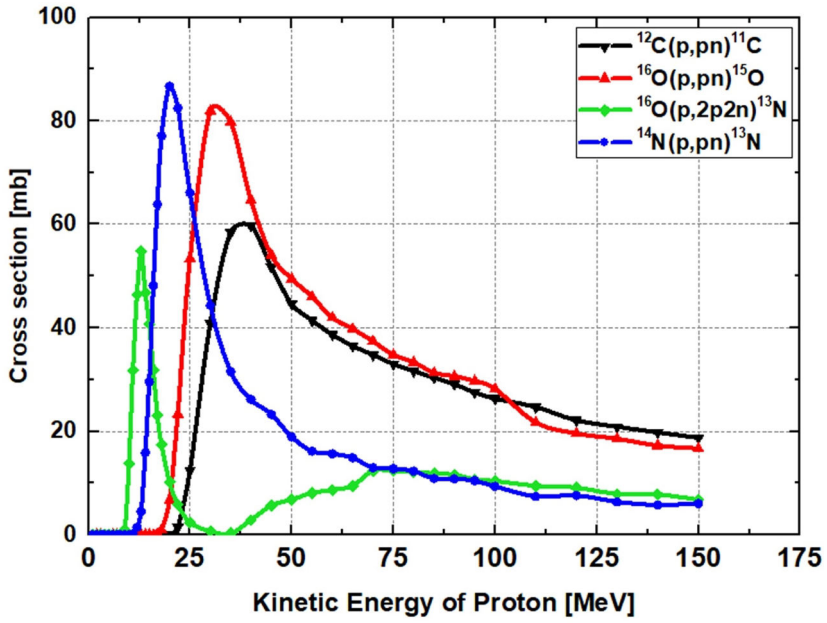

Figure 1.5: Cross sections of the four most common proton nuclear interactions in the body during proton therapy [JENDL].

1.3 Range verification in proton therapy

1.3.1 Proton range

Once a proton departs the accelerator, it begins to lose energy in proportion to the medium's stopping power. When a proton loses all of its energy and comes to a complete stop, it is said to be at the end of its route or range. The penetration depth of protons as well as ions in matter is characterized by the range (or the mean range). Range is defined as the depth at which half of the particles (protons in this case) incident in the absorber have come to rest. This is inherently an average quantity defined for a beam and not for individual particles. If protons are considered to loose energy continously and straight ahead (neglecting lateral scattering), the range can be calculated by:

$$R(E_0) = \int_{E_0}^{0} \frac{1}{(dE/dx)} dE \tag{1.10}$$

where E_0 is the initial kinetic energy of proton. This integral approximates the finite average path length traveled by an ion (proton in this case) in a substance very well. As physical interactions are stochastic (random), the number of collisions along the ion range varies, so that all ions do not stop at exactly the same depth. This effect is known as range straggling (or energy straggling). The most probable proton energy loss in individual collisions is of the order of 20 eV [ICRU-49]. The inelastic

Coulomb interaction with atomic electrons is almost entirely responsible for stumbling. Elastic nuclear collisions and charge exchanges, on the other hand, start to contribute significantly to range straggling at energies below around 1 MeV. The range straggling increases with the penetration depth in a given material, resulting in Bragg-peak of larger width and smaller height for higher initial energies of the same ion type.

Range measurements are possible using a fluence meter such as a Faraday cup. Since depth dose profiles are commonly measured, a relationship between the range and a specific dose point was required. For protons, the range has been shown to correlate to the distal 80% dose point [Gottschalk, 2004], as shown in Figure 1.6 (a). This point is almost insensitive to the energy dispersion, making it extremely valuable. For safety, clinicians seek to change the Bragg-Peak range, also known as the distal 90% dose point (clinical range), while treating patients. As a result, when discussing range, one must be cautious because two different definitions are employed. A common range-energy relationship used in ICRU-49 or NIST tables is based on the Continuous-Slowing-Down Approximation (CSDA). A logarithmic relationship between the proton energy and range has been established in [Bortfeld, 1997], based on the ICRU-49 tables, so that $ln(Energy) \propto ln(range)$ (Figure 1.6 (b)).

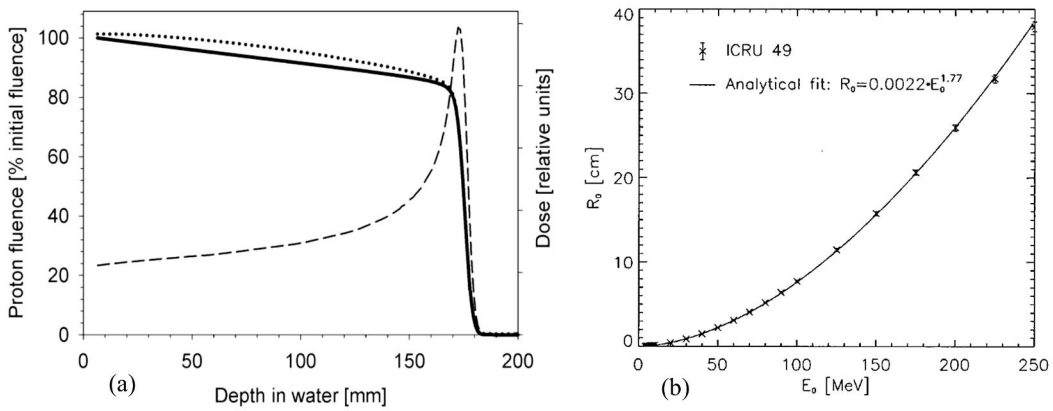

Figure 1.6: Figure (**a**) presents the correlation between particle fluence and dose [Gottschalk, 2004]; and (**b**) Range energy relationship [Bortfeld, 1997].

1.3.2 Range uncertainties

The main advantage of proton therapy cannot be fully exploited if the proton range is not exactly known. Uncertainty can cause the proton beam to overshoot, potentially damaging surrounding healthy tissue [Knopf et al., 2013; Paganetti, 2012]. Range uncertainties can generate notable inhomogeneities in the administered dose, especially in Intensity Modulated Proton Therapy (IMPT), where all the fields are

added together to produce the desired total dose. There are several sources of uncertainty that mention below when it comes to predicting proton range.

- Stopping power ambiguity due to degeneracy of Hounsfield (CT number) values depending on tissue composition.
- Patient misalignment.
- Anatomy changes between or during treatment fractions, as cavity filling, change of weight, tissue swelling or tumor shrinkage.
- Organ motion e.g. respiration and peristaltic motion in the thoracic and abdominal region can cause local density variations, which a proton beam is very sensitive to.
- Biological factors affecting the effective dose in tissue.

Range uncertainties are unique to heavy charged-particle therapy (such as proton therapy) and require margins along the beam path (whereas uncertainties in conventional therapy can be considered as isotropic expansion of the volume to be treated). As a consequence, the PTV concept is not sufficient in proton therapy and it is necessary to apply an additional margin in the beam direction. However, this advantage can only be fully utilized if the range is indeed well known to within at least a few millimeters.

1.3.3 Range verification techniques

While traditional radiation can be measured directly using photons or electrons that pass through the patient's body (portal imaging), heavy charged particles stop inside the patient, making direct measurements difficult. In fact, what can be measured are the secondary emissions due to the interaction of the beam and the irradiated tissue. A number of techniques have been proposed during the last twenty years. Few have been implemented in individual clinical treatments, while many are still at the research stage. Each of these has advantages and disadvantages, and no ultimate or combined solution is yet available in the market. The available approaches are summarized below:

- **Beam probe:** It requires irradiation with a short but highly energetic proton beam that passes through the patient [Mumot et al., 2010]. When comparing the expected and measured residual range, misalignment of the patient or anatomical changes may be detected indirectly. However, the maximum range of current clinical accelerators may not be sufficient in some cases to pass through the patient.

- **Diode arrays:** This is a direct but invasive measurement technique. By implanting a limited number of micro dosimeters with wireless reading in the treated area, it is possible to verify in real time whether the beam is delivered as planned [Lu et al., 2010]. The main concern is to limit this technique to some cancerous locations where such markers may be implanted.

- **Magnetic Resonance Imaging (MRI):** The effect of irradiation on tissue can be analyzed due to the high spatial resolution MRI after treatment [Gensheimer et al., 2010]. However, the range of particles can only be inferred indirectly and a posteriori, and has considerable uncertainties.

- **Proton radiography:** In this technique, protons mainly provide enough energy to the patient to reconstruct planary (two-dimensional, 2D) or tomographic (three-dimensional, 3D) images [Poludniowski et al., 2015]. In this transmission imaging technique, radiography images are created using the input and output coordinates provided by a sensing detector. The major disadvantage of radiography and proton tomography is the scatter effect, which reduces the resolution of the resulting images.

- **Bremsstrahlung imaging:** The secondary electron bremsstrahlung can be used for the verification of the proton range , which uses bremsstrahlung photons generated by the deceleration of charge particles in matter [Yamaguchi et al., 2016]. As these photons are of low energy, the method applies only to the monitoring of irradiation of superficial tumors (i.e. shallow depths). Additionally, the continuous energy spectrum of bremsstrahlung photons makes it difficult to detect and separate from background radiation, unlike positron annihilation photons, which have discrete energies.

- **Prompt Gamma-ray Imaging (PGI):** Prompt gamma imaging is an another widely employed method for verifying the proton range. It uses prompt gamma rays emitted from excited nuclei during the inelastic interactions of incident protons with the target [Min et al., 2006]. This concept of measurement inherently in real time faces technical challenges because of high $\gamma - ray$ rates (detector load and data acquisition rate), neutron background, polychromatic energy spectrum and high $\gamma - ray$ energies. Several PGI solutions based on active and passive collimation have been proposed and some camera prototypes are being clinically translated.

- **Ionoacoustics:** In this technique, the irradiated volume is heated following the radiation dose deposited, and pressure waves are therefore emitted [Hayakawa et al., 1995]. Acoustic pressure waves are characterised by their amplitude,

frequency and shape, which are governed by absorbed dose and target material. The ionoacoustic technique gives a direct approach to the verification of the proton range. However, as regards the relatively weak amplitudes of the acoustic signals, this task becomes more difficult. Furthermore, the complexities of coupling between acoustic sensors and human skin exist, making this technique laborious. On the other hand, it is doubtful or still needs to be investigated if the concept is equally applicable to heterogeneous tissues.

- **Positron Emission Tomography (PET):** It is another interesting and non-invasive technique for protons range verification. Actually it is an auto-activation procedure in where positron emitters such as ^{11}C, ^{13}N, and ^{15}O are produced due to the nuclear interaction between protons and tissues in the patient's body. Following therapy, the activity can be reconstructed using conventional PET scanners and compared to the expected one [Parodi et al., 2001]. It is one of the most promising approaches and has been implemented in several clinical treatments, but a quantitative dosimetry seems not feasible. Online PET scanning during treatment delivery is technically challenging, whereas offline scanning degrades the original distribution due to metabolic washout (long half life of isotopes) and slows down slightly the clinical workflow.

1.4 Positron emission tomography for range verification

1.4.1 Basic concept of PET

Positron Emission Tomography (PET) is a molecular diagnostic imaging technique that detects positrons employing computer processing to visualize various pathological conditions or the behavior of biological substances in the body. Despite the fact that some PET devices have been around since 1950, Dr. Michael Phelps is credited with developing the first PET brain camera at Washington University in St. Louis in 1973 [Phelps et al., 1975]. The PET system detects coincidence i.e., back-to-back gammas produced by positron-electron annihilation. The positron derives from positron emitter unstable isotopes that are either given to the patient during traditional diagnostics or produced in the patient during the particle therapy beam delivery. The most common application of PET is diagnosis. Injected into the patient's body is a radioactively labeled substance known as radiotracer. Fludeoxyglucose (FDG) is the most popular tracer. FDG: is based on ^{18}F ($T_{1/2} \simeq 110$ minutes) bound to a common sugar (deoxyglucose). Tumoros cells have a different metabolism than healthy cells, and they consume more energy. As a result, the tracer will primarily travel to cancerous tissue.

Since, in particle therapy positron emitters (β^+ decay) occur due to nuclear fragmentation when the ion beam interacts with the tissue, without exposing the patient to additional dose from a radioactive tracer. The beta decay is a weak process consisting in the transformation of a nuclear proton into a neutron (n) via the reaction. During beta-decay, the radioactive nucleus emits a positron (β^+) and an electron neutrino (ν_e), according to Eq. (1.11)

$$A(Z,N) \rightarrow A(Z-1,N+1) + \beta^+ + \nu_e \tag{1.11}$$

where Z is the atomic number and N represents the number of neutrons. The positron, the anti-particle of the electron (e^-), is ejected from the nucleus with kinetic energy (KE) in addition to a rest mass of 511 keV. In case of proton the Eq.(1.11) can be written as:

$$energy + p \rightarrow n + \beta^+ + \nu_e + K.E \tag{1.12}$$

The positron particles travel in a random walk manner, interacting with surrounding atoms until they lose most of their energy. The distance traveled depends on the kinetic energy of the particle. During the random walk, the positron range is expressed by the distance between the nucleus and the position of annihilation, not by the total distance traveled. For example, a positron from ^{15}O with have a kinetic energy of 1.73 MeV will travel about 0.50 mm, from ^{13}N with 1.20 MeV will travel 0.28 mm while 0.19 mm will travel for 0.96 MeV kinetic energy from ^{11}C from the nucleus in water. The emitted positron annihilates within 10^{-10} s of its formation with an electron in the body and produces a pair of annihilation photons with 511 KeV each.

$$\beta^+ + e^- \rightarrow 2\gamma \tag{1.13}$$

Annihilation photons travel with 511 KeV in opposing directions (180^o). Sine, the 511 keV annihilation photons are highly penetrating and will leave the body with a high probability of not being absorbed or scattered. These photons can now be detected by the PET scanner's detectors, as shown Figure 1.7. When two detectors simultaneously detect one 511 keV photon each, a positron must have annihilated on a straight line connecting those two detectors. Such an event is called a coincidence and the line is the *line of response* (LOR). There are four possible types of coincidences: true, scattered, random and multiple coincidences. Photons are detected by means of scintillator (typically BGO, LSO or LYSO) crystals which convert each $\gamma - ray$ into visible photons. These photons are in turn collected and converted into an electrical current by photomultiplier tubes (PMTs). The generated electrical pulse is subsequently elaborated by the readout electronics and, if two gammas are

detected in coincidence, a LOR is generated. Given a collection of LORs, a tomographic image (usually 3D) of the activity can be reconstructed deploying several techniques ranging from filtered backprojection to MLEM algorithms.

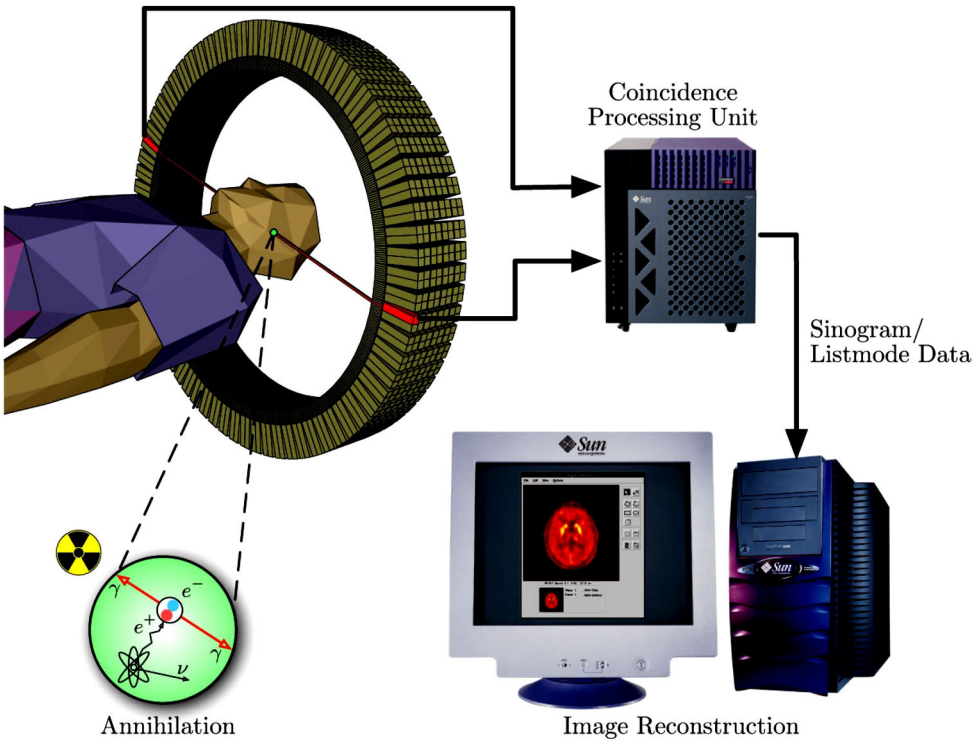

Figure 1.7: Illustration the principal of the PET acquisition, [Langner, 2003].

1.4.2 Particle therapy-PET

This section will provide an overview of the different types of PET that are used for proton range verification. As previously mentioned, in proton beam therapy, a beam monitoring tool is particularly desirable. The idea of employing PET for dose verification in hadron therapy was proposed by Maccabee et al in 1969 [Zhu et al., 2013]. And the first application of PET was took place in the 1980s at Lawrence Berkeley Laboratory(LBL) [Rohling, 2015]. The idea of PET monitoring is based on measuring the activity of the positron emitters created by interactions between the beam particles and tissue atoms. In proton therapy dose verification is usually confined to range verification, since the location of the maximum energy deposition is highly dependent on the proton range. The distal dose fall off and activity fall offs in cavities of the distributions of annihilation sites of observed and anticipated data are compared during range verification. It can be done in one of two ways: point-by-point or by shifting it.

Mainly there are three different PET data acquisition strategies; *in-beam PET*, *in-beam PET*, and *offline PET* are applied to proton range monitoring with PET. With *in-beam PET*, the monitoring takes places quasi-simultaneously to the therapy, by measuring in the pauses of the pulsed irradiation. The PET scanner is integrated in the treatment room. The *in-room PET* is a separate device, but located in the same room. Therefore, the time to transport the patient to the PET scanner after the irradiation is relatively short, and can be done by a robot. There is no need to move the patient. In *offline PET* case data are acquired after patient irradiation with a commercial PET-CT scanner outside the treatment room. In this method a transport time of 5-10 minutes must be taken into account. Figure 1.8 (a) and (b) show the PET systems mounted with proton beam port in the treatment room for range verification.

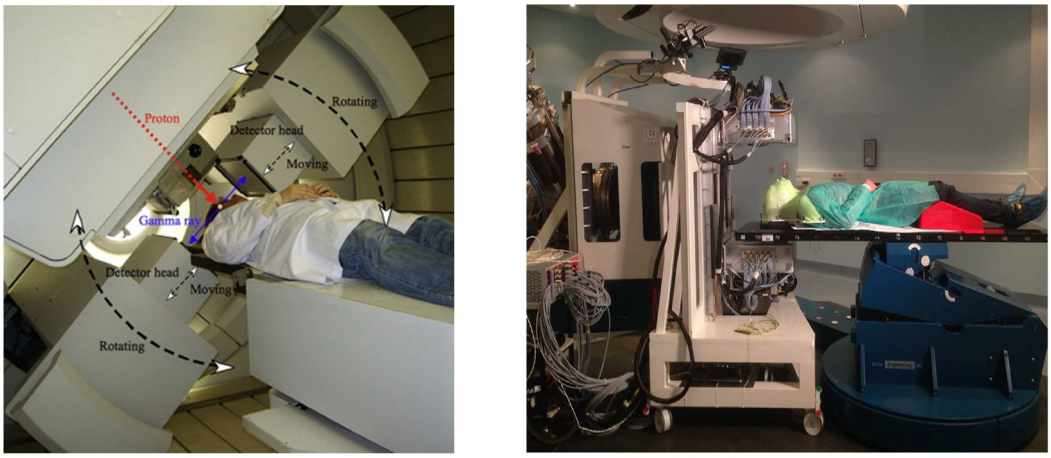

(a) (b)

Figure 1.8: (**a**) PET is mounted on the rotating gantry port [Nishio et al., 2010]; and (**b**) The inside system with detector panels positioned above and below the patient. [Fiorina et al., 2018].

There are various configured PET system such as; full-ring, dual-ring, non-ring, slant angle and so on that have been used in the mentioned strategies [Nishio et al., 2010; Parodi et al., 2007; Tashima et al., 2012; Weinberg et al., 2002; Yamaya et al., 2008]. For example, full-ring scanners which were found to have high detection efficiency but at the same time to incorporate a full-ring PET system into beam delivery, which is technically tedious particularly when there are geometric constraints. Non-ring PET systems were developed to circumvent the drawback of full-ring scanners by providing a higher degree of freedom for better patient positioning and installation. These non-ring PET systems include the DoPET (Dosimetry-PET) system [Vecchio et al., 2009], which is a compact prototype in-beam PET scanner [Shao et al., 2014], a compact planar PET prototype [Kraan et al., 2014] and a modularized

acquisition-based dual-head PET with wider detectors [Sportelli et al., 2013]. The main drawbacks associated with these non-ring PET systems are mainly the limited angular coverage and artifacts in the reconstructed images.

While each method makes a compromise between several factors, a general rule to keep in mind is that the scan should be as long as possible and as quickly as possible after irradiation to achieve an optimal image. One problem all methods have to deal with is that biological processes transport the positron emitter isotopes away from their place of creation. This process is called washout. Washout degrades the signal. However, the overall major challenge of PET monitoring is the low activity in the PET measurements. For these reasons a high sensitive dedicated PET system can ba good tool for proton range verification.

1.4.3 Positron emission mammography

Positron Emission Mammography (PEM) is a dedicated PET system that shares its basics principles with the conventional whole body PET. PEM scanners uses high resolution and high sensitivity detection technology for imaging the breast. PEM was developed to overcome the limitations of PET for detecting breast cancer tumors. PEM allows for the detection of lesions as small as two to three millimeters. Three-dimensional reconstruction of the PEM images is also possible. A design of a dedicated PEM system was first proposed by Thompson et al in 1994 as a feasibility study for a positron emission mammography unit [Thompson et al., 1994]. Since then, more than ten other systems have been developed which are descried below. Some of which have become commercially available. These systems differ in terms of the number, geometry, and mobility of the detectors used, which has an impact on patient positioning; the ability or inability to perform biopsy; the different radiation detection schemes used, including different scintillation crystals; and the strategies used for image reconstruction from measured projections. The photon sensitivity, spatial, energy, and temporal resolutions of a PET/PEM scanner are importances to its performance. The geometry of the detector crystals, as well as the system's electronics, all have an impact on these parameters. This paragraph will highlight the main factors that influence these parameters, emphasizing the most noteworthy differences between traditional clinical and high resolution scanners.

Some dedicated PEM system

An overview of the main PEM equipments will be presented in this paragraph, emphasizing the different approaches followed in their design;

- **The PEM-I system:**
  For the first time, Thompson of McGill University's Montreal Neurological

Institute presented a design for a dedicated positron emission imaging system for breast cancer as a feasibility study for a positron emission mammography unit [Thompson et al., 1995]. The developed scanner was designed to suit a mammographic unit, in order that conventional mammograms could even be performed within the same gantry, thus allowing exact registration of the emission and of the traditional mammographic images. A schematic diagram of the scanner is shown in the Figure 1.9 (a). In the diagram the detector plates (white areas) mounted on a conventional mammographic unit (gray areas).

The scanner is made up of two planar 2×2 detector arrays of blocks of bismuth germanate (BGO) crystals placed above and below the compressed breast. The detector blocks measure 3.6 cm $\times$ 3.6 cm $\times$ 2.0 cm and are segmented into 0.19 cm $\times$ 0.19 cm pixels. The system uses position sensitive photomultiplier tubes (PS-PMT) that are optically coupled to the crystal blocks. Although the PS-PMTs cover a surface of 7.2 cm $\times$ 7.2 cm, their useful field-of-view (FOV) is only of 6.5 cm $\times$ 5.5 cm. The separation between the detector heads is adjusted to match the thickness of the breast. The images from this system are obtained by performing a limited-angle weighted-backprojection algorithm is shown in the Figure 1.9 (b). This consists on dividing the image into several equidistant planes and backprojecting the lines-of-response (LOR) onto those planes. With this technique, the image plane closest to the site of the tumor has the most focused image, while all the other planes present more blurred images.

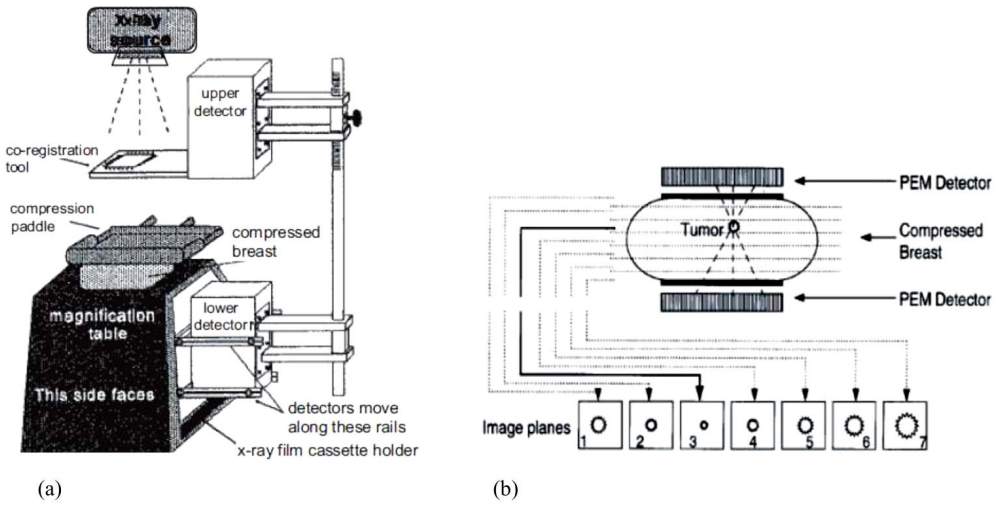

(a) (b)

Figure 1.9: (**a**) Diagram of the PEM-I system [Thompson et al., 1995]; and (**b**) Weighted backprojection used in the PEM-I scanner [Murthy et al., 2000].

❒ **The Naviscan PEM system:**

The Naviscan PET System was based on Thompson's original idea for a PEM system, which was further developed by Weinberg et al. The Naviscan PEM Flex is a steriotactic mammography system that comprises of two 5.6 cm $\times$ 17.3 cm opposed detector heads [Weinberg et al., 2002]. This system allows emission and transmission scans at the same time. Each detector head has twelve 13 $\times$ 13 crystal blocks, each of which is connected to a small PS-PMT. The crystals are a mixed-lutetium silicate with a volume of 0.2 cm $\times$ 0.2 cm $\times$ 1.0 cm. The PEM Flex system placed in a stereotactic X-ray mammography equipment. Data acquisition is performed by moving the detectors along a linear path to image as much of the breast as possible. The translation of the PEM detector allows imaging of an area equal to the entire X-ray field of view.

❒ **The Clear-PEM system:**

The Clear-PEM system was developed at CERN ("Conseil Européen pour la Recherche Nucléaire", or European Council for Nuclear Research) as part of the CrystalClear cooperation. The system consists of a dual-plate detector head mounted in a robotic mechanical gantry.

The patient is in the prone position for the breast examination, with the breast hanging through an aperture in the patient's body. The detector heads can be positioned at different separation distances, allowing for the accommodation of different breast sizes.The detector heads cover a 16.2 cm $\times$ 14.1 cm FOV. Each detector head holds 96 detector modules, is constituted of a total of 48 $\times$ 64 = 3072 LYSO:Ce crystals, each crystal having 0.2 cm $\times$ 0.2 cm $\times$ 2.0 cm. In this system images are reconstructed using 3D statistical iterative algorithms or 2D algebraic techniques.

❒ **The LBNL PEM system:**

The PEM scanner developed at the Lawrence Berkeley National Laboratory (LBNL) differs from the ones described here in two ways: it has a rectangular geometry, with four detector plates enclosing the breast as shown in Figure 1.10, and it can measure Depth of Interaction [Wang et al., 2006]. Depth of Interaction (DOI) allows higher signal-to-noise ratio for detection task. The LBNL PEM system consists of four detector plates that cover a rectangular 8.2 cm $\times$ 6.0 cm $\times$ 5.0 cm field of view. The detector modules contain arrays of 0.3 cm $\times$ 0.3 cm $\times$ 3.0 cm LSO crystals that are connected to a single photomultiplier tube (PMT) in one end and to a photodiode array (PD) on the other end. Initially, image reconstruction was performed with a filtered back-projection based reconstruction algorithm that took into account the existence

of DOI information and the irregular angular sampling of the scanner. Later, a list mode penalized maximum likelihood algorithm using Gaussian priors was developed.

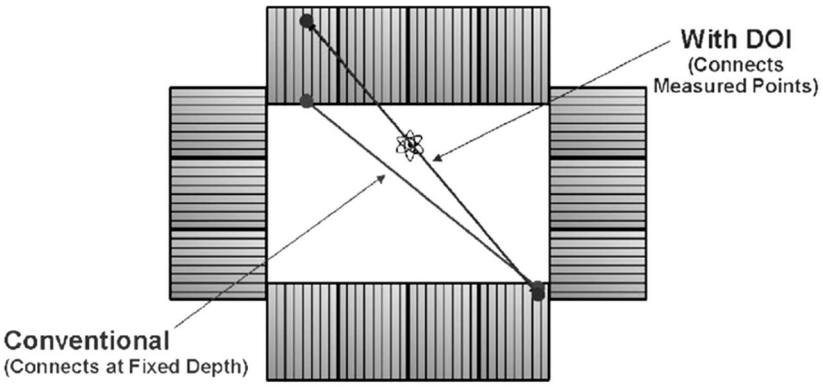

Figure 1.10: Illustration of the geometry of the LBNL PEM scanner with DOI measurement [Wang et al., 2006].

❒ **The Shimadzu dbPET system:**

Shimadzu (Elmammo) dbPET (dedicated breast PET) system [Miyake et al., 2014], developed by Shimadzu Co. and designed with three contiguous rings allowing a larger FOV and confirmed high resolution images with four layers of DOI measurement capability. This system was developed with the goal of allowing simultaneous emission and transmission scans. The system consists of 36 detector blocks arranged in 3 contiguous rings, with a crystal ring diameter of 18.5 cm and an axial extent of 15.55 cm.

Each detector block is composed of a 32×32 array of lutetium oxyorthosilicate (LGSO) crystals coupled to a 64-channel position-sensitive photomultiplier tube via a light guide. Each crystal is 0.45 cm long and has a cross-sectional area of 0.144 cm $\times$ 0.144 cm. The DOI information of 4 layers is extracted from one 2-dimensional position histogram made by Anger-type calculation, which is achieved by insertion of the reflector between crystal elements to control the behavior of scintillation photons. In this system the acquired list-mode data reconstructed by 2-dimensional filtered backprojection with a ramp filter cut-off at the Nyquist frequency.

❒ **The PEMGRAPH system:**

A research group of the Tohoku University collaboratively with Mirai Imaging Inc., Fukushima, Japan was developed a highly sensitive with high-resolution PEM system namely: PEMGRAPH for breast cancer diagnosis [Yanagida et al., 2010]. The PEMGRAPH consists of a dedicated to opposite dual-head PEM

system with Pr:LuAG (Praseodymium-dopped Lutetium Aluminum Garnet) crystal and the $BaSO_4$(Barium sulfate) was used as a reflector as shown in Figure 1.11. The Pr:LuAG scintillator is preferred for angular coverage due to its high light yield, short decay time, and good energy resolution, while $BaSO_4$ is used as a reflector with the crystal to efficiently reflect scintillation photons from Pr:LuAG. In this system one camera unit consisted of 20×64 scintillator pixels optically coupled with three hamamatsu (H8500-03) multi anode photomultipliers. The Pr:LuAG pixel size is 0.21 cm $\times$ 0.21 cm $\times$ 1.5 cm . Four planar cameras are placed at both sides. Therefore, eight cameras were installed at both sides of the instrument. In PEMGRAPH the acquired list-mode data 3-dimensional tomographic image reconstructed by ML-EM algorithm. PEM-

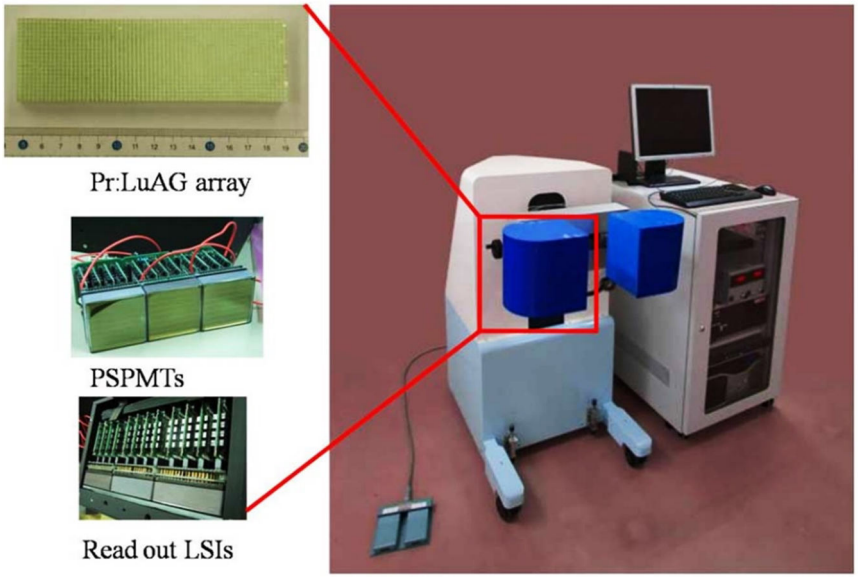

Figure 1.11: Illustration of the detector components with full-scaled PEMGRAPH [Yanagida et al., 2010].

GRAPH showed a high spatial resolution of 2.0 mm (FWHM) in the detector plane and a higher detection sensitivity for breast cancer when compared to whole-body PET [Yanai et al., 2018]. For the better performance with high sensitivity and high spatial resolution recently PEMGRAPH becomes commercially available with new appearance [MIRAI] as shown in Figure 1.12 (a). Presently PEMGRAPH and other mentioned PEM devices have been studied primarily for use in pre-surgical planning and evaluation of breast lesions. Following the development focusing the proton range monitoring a dual-head prototype PEMGRAPH is developed with the collaboration of MIRAI Imaging and Watabe's Radiation Informatics for Medical Imaging laboratory of Tohoku University as shown in Figure 1.12 (b). Due to an open system with

higher sensitivity, it is hypothesized that the developed PEMGRAPH could be a good tool for monitoring the proton therapy.

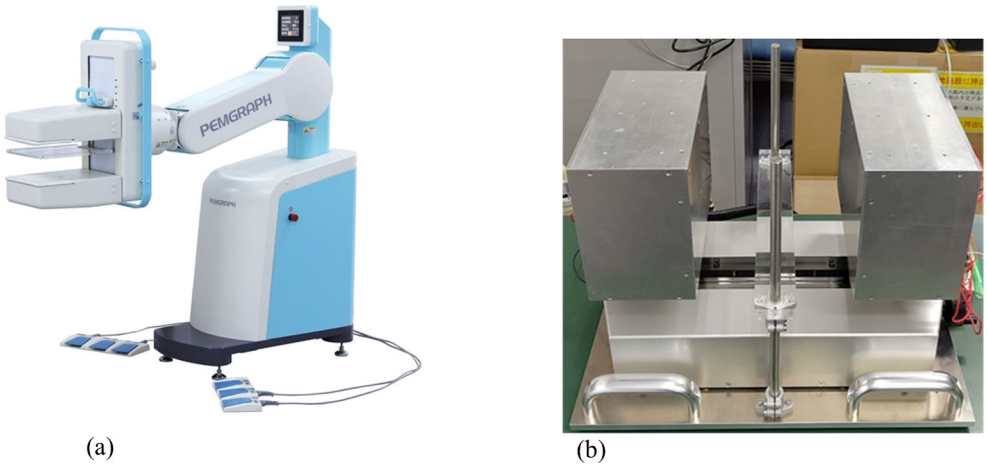

(a) (b)

Figure 1.12: (**a**) Illustration the appearance of newly developed PEM by MIRAI; (**b**) Prototype PEMGRAPH developed by Watabe's laboratory.

1.5 Monte Carlo simulations

PET monitoring relies heavily on simulations of projected PET data. Only precise simulations can ensure the most accurate monitoring. Most of the PT-PET simulations are based on the relatively slow but, sophisticated Monte Carlo method (MC method).

1.5.1 Monte Carlo simulations in proton therapy

The MC method is a numerical technique that generates solutions by applying statistical laws. It has been used for decades in a variety of scientific fields, including particle transport [Carter et al., 1975]. The ENIAC (Electronic Numerical Integrator and Computer) [Anderson, 2014] was built on the concepts of MC techniques pioneered in the 1930s. The MC method relies on random number sampling to address complicated problems where a deterministic solution is either unattainable or too time intensive. Individual values are chosen at random from probability distributions in a stochastic model. The quantity of random values is chosen in a trade-off with the execution time. The more random values used, the more accurate the answer, but the longer the execution time.

Monte Carlo simulations (MC simulations) are still the most reliable method for predicting PET activity distribution [Zhu et al., 2013]. However, two major sources

of uncertainty. The precision of the cross-section data utilized for the models is critical in MC simulations. It was revealed that published cross-section data sets have large differences. The CT conversion is another source. The most commonly used particle transportations packages for calculating predicted activity distributions are FLUKA, MCNP and GEANT4, PHITS.

FLUKA (FLUktuierende KAskade) is another MC simulation code that can be used for a variety of purposes. It's written in FORTRAN and was developed in collaboration with a number of European research institutes [Ferrari et al., 2005]. FLUKA is frequently used in activation, dosimetry, and particle treatment simulations.

MCNP (Monte Carlo N-Particle Transport) [Carter et al., 1974] is a general-purpose code designed to track many particle types over broad ranges of energies and is developed by Los Alamos National Laboratory. MCNP is written in FORTRAN90. This code is used in different areas such as; radiation protection and dosimetry, radiation shielding, radiography, medical physics, nuclear criticality safety, detector design and analysis, accelerator target design, fission and fusion reactor design.

GEANT4 (GEometry ANd Tracking) is an open-source code originally for Large Hadron Collider (LHC) experiments, but later used in many fields of physics. GEANT4 is written in C++ [Agostinelli et al., 2003].

PHITS (Particle and Heavy Ion Transport code System) is a general purpose Monte Carlo particle transport simulation code developed under collaboration between JAEA, RIST, KEK and several other institutes [Iwase et al., 2002, Sato et al., 2018]. PHITS is written in FORTRAN. It can deal with the transport of all particles including simulating proton and heavy ion treatments over wide energy ranges, using several nuclear reaction models and nuclear data libraries. Ionization processes are simulated with the continuous slowdown approximation. For low energy neutron induced reactions, PHITS employs the cross sections from the JENDL[1] nuclear data library. For nuclear reactions of higher energy neutrons and other particles, various sophisticated models are available, including the Microscopic Transport Model (JAM), the JAERI Quantum Molecular Dynamics Model (JQMD), and the INCL model, and the INCLELF model [Niita et al., 2001]. PHITS can also determine profiles of all secondary particles, including prompt 's, and perform microdosimetric calculations. In Chapter 2 will be detailed about PHITS.

[1] **https://wwwndc.jaea.go.jp/jendl/j40/j40.html**.

1.6 Spectral Analysis approach

Different approaches such as, the spills and pauses-based model [Parodi et al., 2001], the Gaussian filter function approach [Parodi et al., 2006], the deconvolution-based approach [Remmele et al., 2011], the kinetic model [Grogg et al., 2015], and many more have been proposed for proton range verification by quantifying proton-induced activity. Each approach/method has their own benefits and drawbacks. In this study, a new approach 'Spectral Analysis' was applied for the analysis and presentation of results obtained from dynamic positron emission tomography (PET) of proton beam irradiation. In dynamic PET studies, the term spectral analysis indicates a single-input/single-output model used for the data quantification. Spectral analysis (SA) allows the quantification of dynamic data by relating the radioactivity measured by the scanner in time to the underlying physiological processes of the investigated system. The SA approach was initially developed in 1993 as a method for mathematical modeling for kinetic analysis of PET studies [Cunningham et al., 1993].

This approach allows a tracer's tissue time-activity curves (TACs) to be described in terms of an ideal subset of kinetic components chosen from a much larger set. The larger set samples the range of possible components visible in the data; it usually consists of convolution integrals of the input function with decaying exponentials, allowing the selected components to be connected to a suitable compartmental model for the system under investigation. The SA can be used in a framework where kinetic data is measured in regions of interest (ROI) or single pixels. The SA approach can apply to both homogeneous and heterogeneous without any previous hypotheses; this makes it useful for the analysis of tracer kinetics of PET data with the limited spatial resolution of the scanner [Turkheimer et al., 1994]. Furthermore, this approach also provides an estimate of the rate constant of trapping of tracer in the tissue as well as the amplitudes and decay constants of the reversible components. This information can be used for subsequent specification of a kinetic model, or it can be used to estimate selected parameters of the system that do not depend on the specific model configuration, such as the total volume of distribution of the tracer. However, the spectral analysis technique cannot be used for all linear compartmental systems; a set of conditions must be met in order for it to be used. In this study, the SA approach was applied for quantification of different isotopes of positron emitters such as ^{11}C, ^{13}N, and ^{15}O that are produced by inelastic nuclear interactions of protons with the target elements during proton irradiation. More details about SA approach will be explained in Chapter 4.

1.7 Motivation and objectives of the thesis

Radiation therapy is one of the most common cancer treatment along with surgery and systemic therapy. The ultimate goal of radiation therapy is to deliver a certain amount of radiation dose to the targeted organs while not affecting healthy organs and cells. In this regard, the use of high-energy proton beams has garnered significant attention worldwide owing to their low lateral scattering, no exit dose, and high dose deposition in the Bragg peak region. Considering the proton therapy, a major obstacle would be the uncertainties associated with the range of the proton beam, at which largest dose gradient is located. Several techniques for proton range monitoring have been introduced and discussed. Most of these methods are based on the byproduct of proton beam irradiation on patients.

Auto-activation positron emission tomography (PET) is an interesting and non-invasive technique that can be used for the range verification of protons; it focuses on measuring photons annihilated from generated positron emitters such as ^{15}O, ^{11}C and ^{13}N as a result of nuclear interaction between protons and tissues in the body of the patient. Recently, reported that the ^{16}O(p,2p2n)^{13}N reaction has a relatively low threshold energy (5.660 MeV) [Cho et al., 2017]. Therefore, by computing the gradient between early and late PET scans, one can extract the ^{13}N creation, which is discovered to be associated closely with the Bragg peak. Considering this property and the high sensitivity and spatial resolution of some previously developed PET systems, it would be useful to extensively investigate the underlying mechanism and feasibility of the ^{16}O(p,2p2n)^{13}N nuclear reaction and the generated ^{13}N peak. Monitoring proton therapy sensitivity of the PET/PEM imaging device is a significant issue where a small number of positron emitters (such as ^{15}O, ^{11}C and ^{13}N) are produced only for target fragmentation [Kraan et al., 2014; Shao et al., 2014; Sportelli et al., 2013; Vecchio et al., 2009]. The positron emission mammography (PEM) system, which is a dedicated PET system for detecting breast cancer, is another notable device that has higher spatial resolution and sensitivity than previously introduced systems. Although it was shown that highly sensitive PEM has the same mechanism of PET and presently using only for breast cancer diagnosis purposes. In order to make the proposed procedure suitable for real PET acquisition data, it is crucial to take into account some aspects regarding the Spectral Analysis approach.

The primary objective of this research is to develop the simulation, experimental, and analysis tools for the extraction of PET isotope production for range verification in proton therapy. These are to be applied in a first phase to the production

of ^{15}O, ^{11}C and ^{13}N for protons of 80 MeV at the AVF (azimuthally varying field) cyclotron. The activity measurements will be performed with a highly sensitive dual-head PEM (PEMGRAPH) scanner. For the purposes of proton range monitoring, this thesis initially investigated the distribution of positron emitting radioisotopes near the distal edge. The spatial distribution of secondary particles was to be simulated using PHITS Monte Carlo code. Subsequently, the results from the simulations were in a second step used to evaluate the setup and performance of a highly sensitive prototype PEM system for experimental measurements. As a final step, the SA approach was used to extract proton induced radioisotopes and compared to simulations.

1.8 Structure of the thesis

Following is the organization of this thesis:

Chapter 1: Introduction

It aims to introduce the concepts and physics of proton therapy, as well as the sources of uncertainty in proton range. A brief review of the proton range verification methods were discussed. An overview of PET including the most demanding aspect of the dedicated PEM systems are presented. This chapter also briefly discussed Monte Carlo codes and the spectral analysis approach. The motivations and objectives of the thesis are also presented.

Chapter 2: Simulation of positron emitting radioisotopes during proton therapy

The second chapter describes the materials and methods, along with the results of the simulations studies conducted in this study, including the PHITS Monte Carlo Code extensively used for particle transport and interaction.

Chapter 3: Detection of positron annihilation photons by PEM

The third chapter describes the geometry and mechanism of a positron emission mammography (PEM) as well as the experimental setup and results for proton beam range verification.

Chapter 4: Quantification of proton-induced radioisotopes using SA Approach

The fourth chapter goes into detail about the SA approach, including mathematical equations for proton therapy verification. This chapter also discusses the application of the SA approach to the simulation results as well as experimental measurements..

Chapter 5: Quantitative comparison and proton range verification

The fifth chapter describes the quantitative comparison of the simulated and SA extracted results. The SA extracted radioisotopes from the measured data also compared to the simulated dose for proton range verification.

Chapter 6: Conclusions and future prospects

The final chapter of this PhD thesis work concludes with a general conclusion and a look into the future perspective.

Chapter 2

Simulation of positron emitting radioisotopes during proton therapy

2.1 Monte Carlo simulation of positron emitting radioisotopes

A method on the use of positron emission tomography (PET) for verifying the range of a clinical proton radiotherapy beam has been proposed: measuring photons annihilated from generated positron emitters such as ^{15}O, ^{11}C, and ^{13}N as a result of nuclear interaction between protons and tissues in the body of the patient. In this chapter, details about the performed simulations of proton induced nuclear reactions with the main elements of human tissue, ^{16}O, ^{12}C, and ^{14}N using the nuclear reaction models of the PHITS Monte Carlo (MC) code will be given. MC simulations, in particular, can be used for providing a complete simulation of radiation interactions, as well as the geometry of the treatment hardware and the anatomy of the patient. The calculation of positron activity distributions involves a wide range of probability distributions, including scatter processes, nuclear reactions, decay processes, capture cross sections and more discussed details in Chapter-1.

In this chapter, the simulation of positron emitters during proton irradiation in a homogeneous inhomogeneous slab and MIRD slab anthropomorphic targets was investigated using the PHITS code. Proton induced nuclear reactions in the 40 MeV to 250 MeV incident energy range on homogeneous phantom were studied focusing to calculate the offset distance between the distal edge positron emitting isotopes and the real Bragg peak. At the beginning of this chapter a brief introduction to the simulation software PHITS will be provided, followed by technical details and descriptions of the methods and simulations used.

2.2 PHITS Monte Carlo code

Particle and Heavy Ion Transport code System (PHITS) [Sato et al., 2018] is a general-purpose Monte Carlo particle and heavy ion transport code written in FORTRAN and the recommended compiler is Intel FORTRAN 11.1 (or later versions). PHITS can deal with the transport of nearly all particles, including neutrons, protons, heavy ions, photons, and electrons, over wide energy ranges using various nuclear reaction models and data libraries. Ionization processes are simulated with the continuous slow down approximation. For low energy neutron induced reactions, PHITS employs the cross sections from the **JENDL** nuclear data library. For nuclear reactions of higher energy neutrons and other particles, various sophisticated models are available, including the Microscopic Transport Model (JAM), the JAERI Quantum Molecular Dynamics Model (JQMD), the INCL model, and the INCL-ELF model [Niita et al., 2001] shown in Figure 2.1.

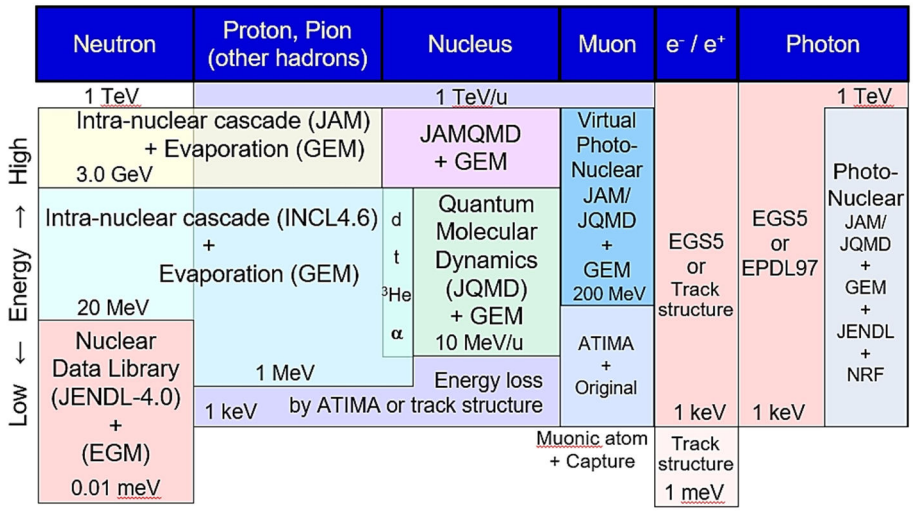

Figure 2.1: A map of the physics models and data libraries recommended for use in PHITS to simulate nuclear and atomic collisions, [Sato et al., 2018].

PHITS can be executed on the Windows, Mac, and Linux platforms. In the simulation, general geometry (GG) or combinatorial geometry (CG) must be set as the geometric configuration. PHITS can calculate numerous quantities using "**tally**" estimator functions, such as heat deposition, track length, and production yields. Additionally, users can calculate any information necessary for their own purposes, such as event lists of a certain type of nuclear reaction, by writing a custom tally program. The code also allows for drawing 2D and 3D figures of the calculated results and setup geometries using an original graphic tool named ANGEL. PHIG-3D (PHITS Interactive Geometry viewer in 3D) is the input geometry visualization

software for PHITS based on the Gxsview (Geometry and cross section viewer) [Ohnishi, 2021]. It can visualize 3D geometries and also export them to files as both 2D images (png, jpg, bmp) and 3D data (vtk, vtp, ply, stl) as well. In addition, users can deduce any information for their own needs, such as event lists of a certain type of nuclear reactions, by writing a user-defined tally program. Moreover, the time evolution of radioactivity can be estimated by using DCHAIN-SP, which is included in the PHITS package [Kai et al., 2001]. PHITS has several important features, such as an event-generator mode for low-energy neutron interaction, beam transport functions, a function for calculating the displacement per atom (DPA), and a microdosimetric tally function. Due to these features, it has been widely used for various applications. Calculation of the dose and dose equivalents in human bodies irradiated by various particles was carried out using PHITS in order to determine radiological protection needs and medical physics issues. A wide range of functions are available for medical physics applications, including radiation facility design, radiation therapy, and radiation protection. In radiotherapy, the RT-PHITS package is used to evaluate radiation doses generated by PHITS simulation. The RT-PHITS includes several modules that can be used to convert DICOM data into PHITS format so that PHITS simulations can be performed using these data.

2.2.1 PHITS structure

The PHITS code is an easy-to-use MC code written in FORTRAN, but its parameters are controlled by txt-files. Using txt-files, users can control geometry, particle source, materials, surface, cell, tally and graphical output without any previous knowledge of FORTRAN. Every command line in a txt-file has the same structure: [Title]; [Parameters]; [Source];.....[End]. Figure 2.2 shows an example of input parameters using a txt-file in the PHITS code.

In PHITS geometry is defined by [Material], [Surface], and [Cell] sections, and one can define a number of 3D geometrical components based on GG concepts. The basic of PHITS geometries structure are shown in Figure 2.3. PHITS simulates the motion of each particle using the Monte Carlo method. Various physical quantities, such as flux, particle track, heat deposition, energy deposition and yield production, can be calculated by using "Tally" to estimate their average behavior. The geometrical mesh structure of Tally's are shown in Figure 2.4.

```
[ T i t l e ]
PHITS input structure
[ P a r a m e t e r s ]
 icntl    =          0
 maxcas   =         50
 maxbch   =          2
 file(1)  = c:/phits
 file(6)  = phits.out
[ S o u r c e ]
    s-type =   1
     proj =  proton
      dir =   1.0
       r0 =   0.
       z0 =   0.
       z1 =   0.
       e0 =   150.

[ M a t e r i a l ]
mat[1]    H 2  O 1

[ S u r f a c e ]
  10  so      10.

[ C e l l ]
 100     1 -1.0  -10
 101    -1        10
```

```
[ T - T r a c k ]
     mesh =  xyz
   x-type =    2
       nx =  200
     xmin =  -20.
     xmax =   20.
   y-type =    1
       ny =    1
            -5.0  5.0
   z-type =    2
       nz =  200
     zmin =  -20.
     zmax =   20.
   t-type =    2
       nt =    1
     tmin =   0.0
     tmax =   1.0
     part =  all
   e-type =    1
       ne =    1
              0.0  1000.0
     unit =    1
     axis =   xz
     file = track_xz.out
    title = Track Detection using
    gshow =    3
   epsout =    1

[ E n d ]
```

Figure 2.2: The illustration of the input parameters for the PHITS code using a txt-file, [PHITS User Guide].

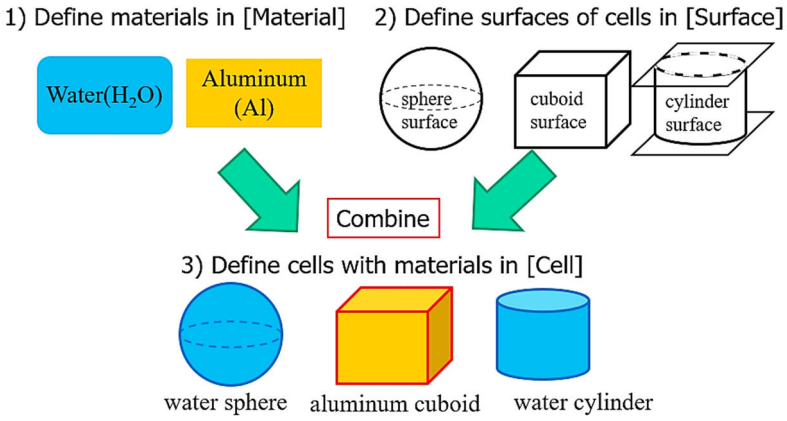

Figure 2.3: Basic of PHITS geometries, [PHITS User Guide].

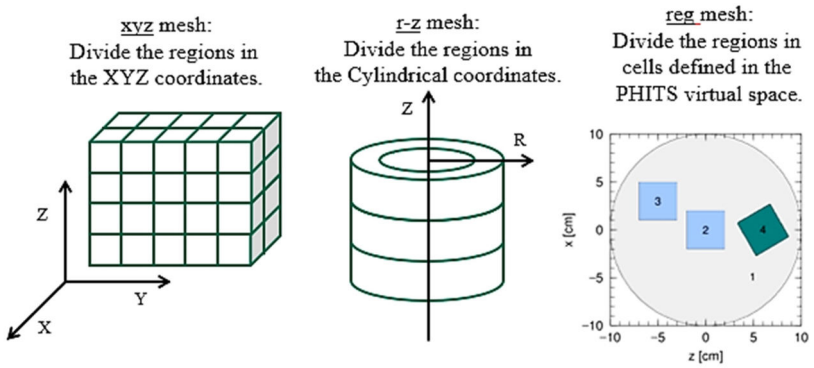

Figure 2.4: Different types of geometrical mesh of the PHITS Tally, [PHITS User Guide].

2.2.2 PHITS GUI for simulation of positron emitting radioisotopes

Applications of the PHITS code are becoming more popular in various fields including medical dosimetry. Many PHITS MC packages and modules such as RT-PHITS (radiotherapy package based on PHITS) [Sato et al., 2021], PHIG-3D (PHITS Interactive Geometry viewer in 3D) are being developed in order to make PHITS applications more user-friendly. In the progress of developing PHITS MC package, our group developed a PHITS GUI (graphical user interface) bundled with a custom-made 3D OpenGL visualizer for proton irradiation of a homogeneous phantom made of most commonly used biological materials [Beni et al., 2022]. The FORTRAN90 programming language was used to write the main program and all of the subroutines. On the other hand, the OpenGL 3D plotter program was written in C++ and read the output of the main GUI program to plot the 3D structure. However, no prior user experience is required to run the developed GUI program. The developed GUI program is shown in Figure 2.5. The developed GUI is an open-source program that allows users to freely download, modify, recompile and redistribute the program.

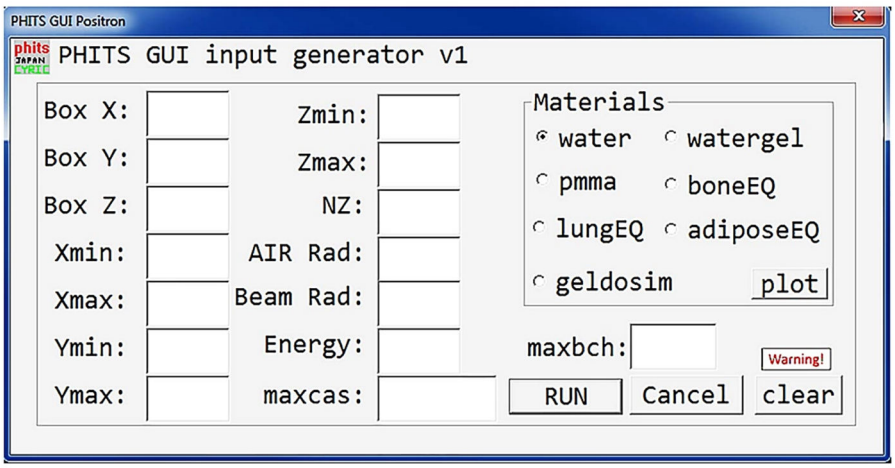

Figure 2.5: PHITS input generator GUI for proton irradiation of commonly used materials, [Beni et al., 2022].

Using the present GUI program, homogenous phantoms with one material among seven materials (water, water-gel, PMMA, bone equivalent, lung equivalent, adipose equivalent, and gel dosimeter) can be modeled for each simulation with a rectangular parallelepiped of user defined dimensions. Users can change the energy (MeV) of incident protons beam and its radius. Moreover, users can change source parameters such as particle type and direction manually in the generated PHITS script using the GUI program. The number of histories (maxcas, maxbch) and tallies parameters can be configured as desired by the user. Several test cases were

conducted to validate the developed GUI program. For example, the test results for a case are shown in Figure 2.6.

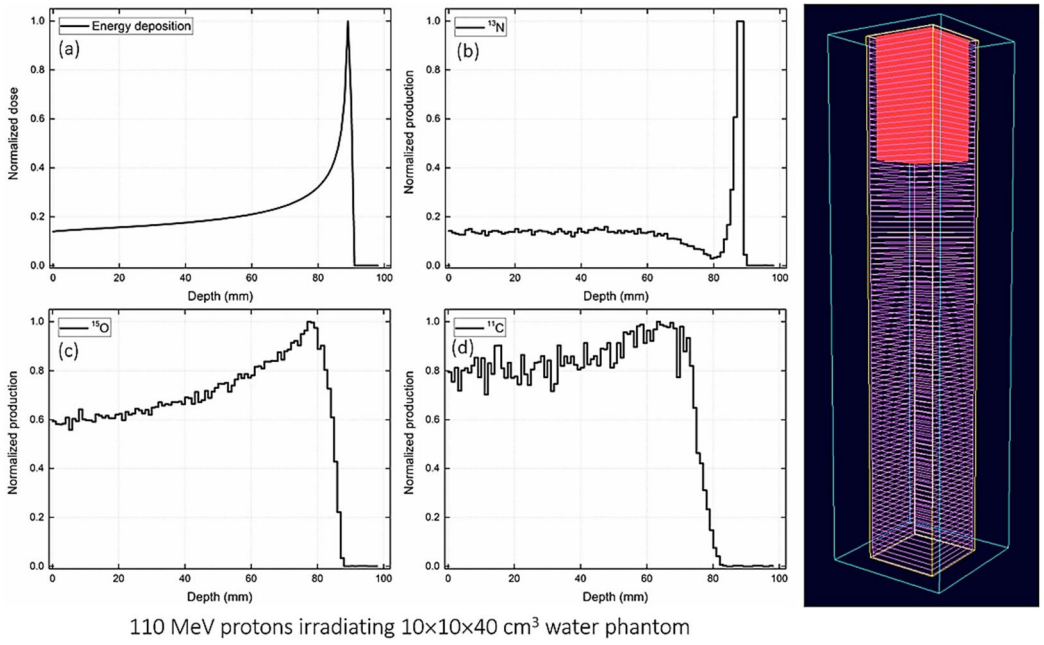

Figure 2.6: Test case 1: irradiation of water phantom with 110 MeV protons with (a) total energy deposition, distribution of (b) ^{13}N, (c) ^{15}O and (d) ^{11}C production. The 3D plot has been obtained from the OpenGL plotter program, [Beni et al., 2022].

The results shown in Figure 2.6, that the dose is increased with axial depth and stopped after producing the Bragg peak. These radioisotopes (^{15}O, ^{11}C, and ^{13}N) were generated as results of proton interaction with the phantom materials. The GUI program generated the tally card for scoring the production of these positron emitting radioisotopes automatically. A number of features are included in the present GUI program, including its fast execution, although the PHITS execution is highly dependent on the number of histories a user sets. The present GUI can reduce the possibility of errors as well as the time required to prepare input scripts for proton irradiation and proton induced radioisotopes.

2.3 Phantom irradiation for positron emitting radioisotopes

MC simulation for phantoms modeling and irradiation were performed using PHITS code. The simulations were done in two steps. The first parts included the construction of a homogeneous phantoms modeling. The second parts included for inhomogeneous slab and MIRD anthropomorphic phantoms. The phantoms were irradiated proton beams. A depth dose and positron emitting radioisotope were scored in both studies to assess the proton range. It was focused on the formation

of distal edges, which can be used to confirm proton range by comparing it to the real Bragg peak. This prediction was determined using PHITS, which produces list mode data files in the same format as the PET/PEM scanner, and can be reconstructed using the same method as measured PET/PEM images.

2.3.1 Simulation in a homogeneous phantom

Using the PHITS GUI a homogeneous water-gel phantom with 10.0 cm × 10.0 cm × 40.0 cm outer dimension was modeled. Figure 2.7 shows the diagram of the modeled phantom. An Appendix-A (A.1) contains the input parameters of the homogeneous phantom. The material composition of the modeled water-gel is presented in Table 2.1. The modeled proton beams with energies of 80, 160, and 240 MeV and diameters of 1.0 cm are used to produce the pristine Bragg peak. The beams were emitted along the positive z-axis. Figure 2.7 shows the location where the incident proton beam is irradiated. In the irradiation setup, a 25.0 cm air gap was used to account for the real situation of treatment. Total 10^9 protons were used from the modeled beam to reduce statistical errors associated with the MC technique. The Monte Carlo method can be used to consider the stochasticity of radiation interactions with matter; this is generally performed by employing random numbers to estimate the interaction with distinct nuclei and sampling the angular and energy distribution. Given this stochasticity, statistical analysis of the outcomes is critical, as low relative error in the estimated results is sought. Different positron emitters were formed when protons interacted with target atoms, which was mostly due to inelastic nuclear interactions that were explained in Table 1.1 of the Chapter-1.

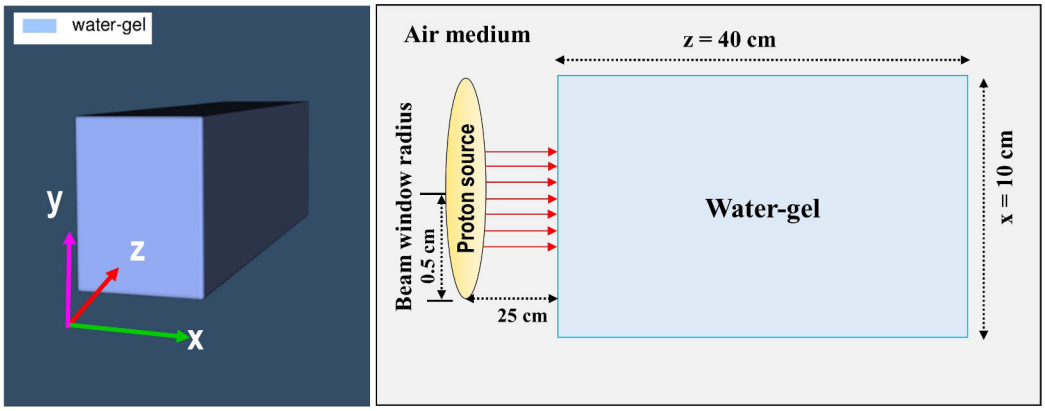

Figure 2.7: A homogeneous water-gel phantom with 3D visualization was irradiated with monoenergetic proton beam.

Table 2.1: Material composition and density of the homogeneous water-gel phantom (weight %).

Material	**Density (g cm^{-3})**	**^{1}H (%)**	**^{12}C (%)**	**^{16}0 (%)**
Water-gel	1.010	11.00	4.650	84.35

In addition to check the dose profile as well as activity distribution in case of SOBP distribution an energy modulated (70-80) SOBP fields were modeled. In reality, the particle accelerator produces a narrow near-monoenergetic beam of protons, known as a pencil beam, which when penetrating matter forms a pristine Bragg peak that is not deep enough to cover most treatment volumes. To deliver proton beams suitable for treating patients, the beam must be shaped and modulated, as well as broadened in depth in the beam direction through a patient. This is accomplished by combining several pristine Bragg peaks of varying energy (range) and summarizing their contributions to a treatment beam by applying a relative weight to each pristine Bragg peak. The net result of this composition is a spread out dose plateau region known as the Spread-out Bragg peak (SOBP).

To analyze LET, Fluence, and beam track in the water-gel for 80 MeV proton beam the PHITS tally functions mentioned in Appendix-A [A.1] was used. The absorbed dose verses depth and the spatial distribution of the positron emitting radioisotopes (i.e.,^{15}O, ^{11}C, and ^{13}N) were scored along the z-axis of the incident proton beam. Generally, the Monte Carlo simulation package normalizes tally results by primary source particle, as absolute values are meaningless. The obtained results were therefore normalized individually. The PHITS output data was then analyzed using our previously developed python based PyBLD module. PyBLD[1] is a program for evaluating scientific data, particularly time-course and multidimensional data. PyBLD is an interpreter-type language that runs on Python [Carson et al., 1981]. Based on the PET data acquisition protocol, the obtained data were converted to activity by calculating the half-life of each radionuclide. Two-dimensional (2D) images were reconstructed using PyBLD. A Medical Image Data Examiner (AMIDE[2]) was used to analyze the images that made using PyBLD. AMIDE is a completely free tool for viewing, analyzing, and registering volumetric medical imaging data sets. It's been written on top of GTK+, and runs on any system that supports this toolkit (Linux, Windows, Mac OS X, etc.). The three-dimensional (3D) scatter plot drawn with python scatter plot script. The one-dimensional (1D) depth dose and activity profiles were produced, providing information on the position and distribution of the activity. A comparison is also made between the pristine

[1] **http://www.rim.cyric.tohoku.ac.jp/software/pybld/pybld.htm**.
[2] **http://amide.sourceforge.net**.

Brag peak positions and the peak produced by the distal edge positron emitter. The 1D, 2D and 3D depth dose and the distribution of positron emitting radioisotopes plotted in case of monoenergetic proton beam field. Just for simplicity, a dynamic time-frames were constructed for every 1 minute up to 55 minutes only for 80 MeV incident proton energy. Furthermore, the 1D and 2D depth dose and the distribution of positron emitting radioisotopes also plotted in case of SOBP distributions.

2.3.2 Simulation in an inhomogeneous phantoms

Inhomogeneous slab phantom

To investigate the impact of phantom composition on positron emitting radioisotopes, in addition to the uniform phantom, an inhomoheneous slab phantom with four different materials was designed. The model of a inhomogeneous slab phantom focuses on two areas: the first is to produce pristine Bragg peaks at the interface regions of the two materials using a monoenergetic proton beam, and the second is to produce SOBP using an energy modulated beam. An ingomogeneous slab phantom composed by 2.0 cm PMMA (polymethyl methacrylate), 1.0 cm lung-equivalent (inflated), 1.0 cm water, and 2.0 cm bone-equivalent (cortical bone slab) thick materials with total 5.0 cm $\times$ 5.0 cm $\times$ 6.0 cm dimensions was modeled using PHITS. The PHITS GUI wasn't used here since that was developed only for homogeneous cases. An Appendix-A [A.2] contains the input parameters of inhomogeneous slab phantom. This configuration was chosen to prevent the maximum beam energies from passing through the PMMA/bone-equivalent interface. All slabs were arranged to form interfaces all positioned perpendicular beam direction except for the last two one, set parallel so that the Bragg peak is produced at the interface (PMMA/bone-equivalent). Table 2.2 shows the material composition of the modeled inhomogeneous slab phantom. The diagram of the modeled geometry is shown in Figure 2.8. The simulated phantom was irradiated with a pencil like (1.0 cm diameter) proton of an 80 MeV mono-energetic beam for producing pristine Bragg peak and with 1 MeV interval energy modulated beams (70-80 MeV) for spread-out Bragg peak (SOBP) fields. There was a 25.0 cm air gap between the proton beam and the phantom, and the beam was emitted along the positive z-axis as shown in Figure 2.8. Same as homogeneous, 10^9 protons were considered for irradiating in the pristine and SOBP fields. As a result of proton interactions with target elements, a variety of positron emitters were produced.

Table 2.2: Material composition and density of the inhomogeneous slab phantom (weight %).

Material	Density (g cm^{-3})	^{1}H (%)	^{12}C (%)	^{14}N (%)	^{16}O (%)	^{23}Na (%)	^{24}Mg (%)	^{31}P (%)	^{32}S (%)	^{40}Ca (%)
Water	1.000	11.10	-	-	88.90	-	-	-	-	-
PMMA	1.180	8.050	59.99	-	31.96	-	-	-	-	-
Lung	0.260	10.30	10.50	3.100	74.90	0.200	-	0.200	0.300	-
Bone	1.850	3.400	15.50	4.200	43.50	0.100	0.100	10.30	0.300	22.50

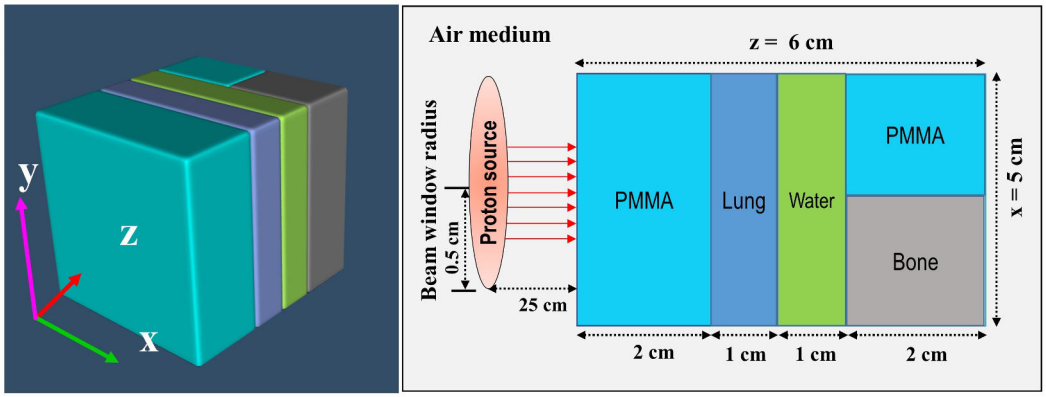

Figure 2.8: A three-dimensional schematic view of a inhomogeneous slab phantom.

MIRD anthropomorphic phantom

The Medical Internal Radiation Dose Committee (MIRD) anthropomorphic phantom was used to investigate the effect of inhomogeneities of human tissues on the obtained ^{13}N peak location and its offset with the Bragg peak. An Appendix-A [A.3] contains the input parameters of MIRD anthropomorphic phantom.The deposited proton dose and distribution of proton induced positron emitting radioisotopes were determined in a spherical tumor placed in the left lung of the MIRD anthropomorphic phantom. The radius of the spherical tumor was set to be 1.0 cm. The modeled MIRD anthropomorphic phantom, tumor location and irradiation zone are shown schematically in Figure 2.9. The densities and the material composition for the modeled MIRD anthropomorphic phantom were taken from Reference [Goldstone, 1990] and summarized in Table 2.3. Regarding the other elements (shown in the last column of Table 2.3), the stable isotopes (i.e., mass number shown in the periodic table) of these elements were considered. The tumor located in the left lung of the modeled MIRD anthropomorphic phantom was irradiated with 80 MeV monoenergetic incident proton beam (see Figure 2.9). The irradiation field size set to be a 1×1 cm^2 squared shaped source. The beam was perpendicular to the tumor volume along the negative y-axis. A total of 10^9 incident protons were launched from the source, to minimize the statistical uncertainties associated with MC computations.

Table 2.3: Material composition and density of the MIRD anthropomorphic phantom (weight %) [Goldstone, 1990].

Material	Density (g cm^{-3})	^{1}H (%)	^{12}C (%)	^{14}N (%)	^{16}O (%)	Others
Skin	1.090	10.00	20.40	4.200	64.50	0.2Na, 0.1P, 0.2S, 0.3Cl, 0.1K
Soft tissue	1.030	10.50	25.60	2.700	60.20	0.1Na, 0.2P, 0.3S, 0.2Cl, 0.2K
Heart tissue	1.050	10.40	13.90	2.900	71.80	0.1Na, 0.2P, 0.2S, 0.2Cl, 0.3K
Blood	1.060	10.20	11.00	3.300	74.50	0.1Na, 0.1P, 0.2S, 0.3Cl, 0.3K, 0.1Fe
Lung	0.260	10.30	10.50	3.100	74.90	0.2Na, 0.2P, 0.3S, 0.3Cl, 0.2K
Ribs (1^{th}- 9^{th})	1.410	6.400	26.30	3.900	43.60	0.1Na, 0.1Mg, 6.0P, 0.3S 0.1Cl, 0.1K, 13.1Ca
Ribs (10^{th}- 12^{th})	1.520	5.600	23.50	4.000	43.40	0.1Na, 0.1Mg, 7.2P, 0.3S 0.1Cl, 0.1K, 15.6Ca

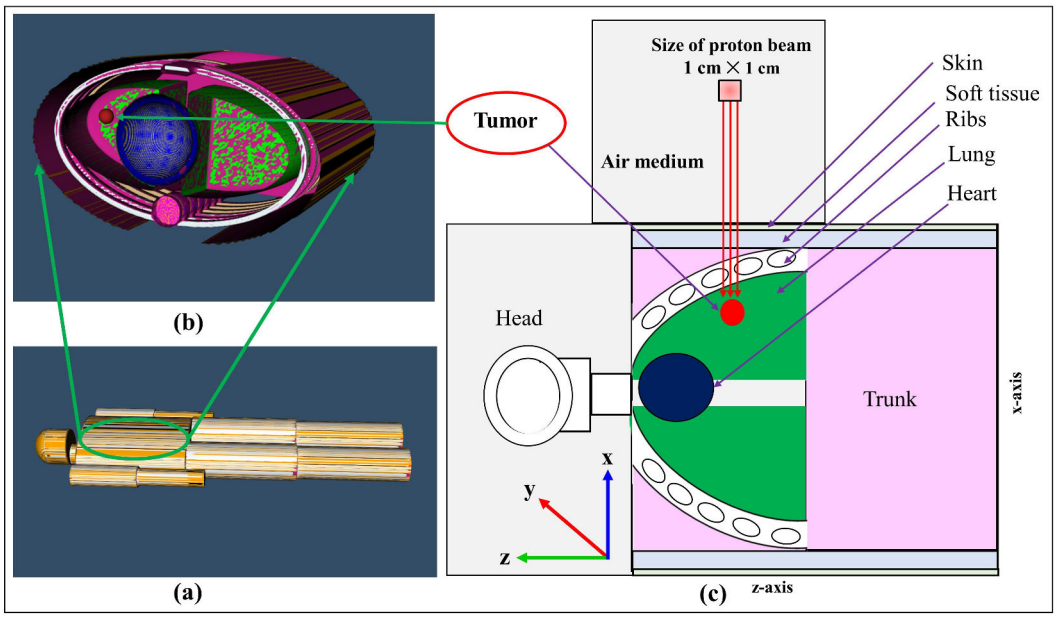

Figure 2.9: The modeled MRID anthropomorphic phantom with tumor location marked. The irradiation of the spherical tumor placed at left lung is also shown with a 1×1 cm^2 field size.

For both inhomogeneous slab and MIRD anthropomorphic phantoms the dose and positron emitting radioisotopes were scored with respect to the depth in the same way as the homogeneous data, and the data was analyzed using AMIDE and PyBLD.

2.4 Results and discussion

The simulation results are presented in this section. The results included depth dose profiles and positron emitter production profiles in 1D, 2D, and 3D, as well as PHITS results for a variety of geometry and materials.

2.4.1 Homogeneous phantom:

The PHITS MC simulated fluence distribution and LET (linear energy transfer) distribution with depth for an 80 MeV proton beam in the homogeneous water-gel phantom are shown in Figure 2.10. The normalized fluenece and LET are shown in solid black and dotted red lines the y-axis express their values. Due to the nuclear interactions of protons with target nuclei, the primary fluence reduces in proximity of the Bragg peak and then steeply falls down, where the highest LET values are achieved. For a beam of protons, the fluence of primary protons is very consistent towards the Bragg peak.

For 80 MeV of incident proton energy the particle track in the water-gel phantom is shown in Figure 2.11. The particle track indicts the fluence of the particle in the given region.

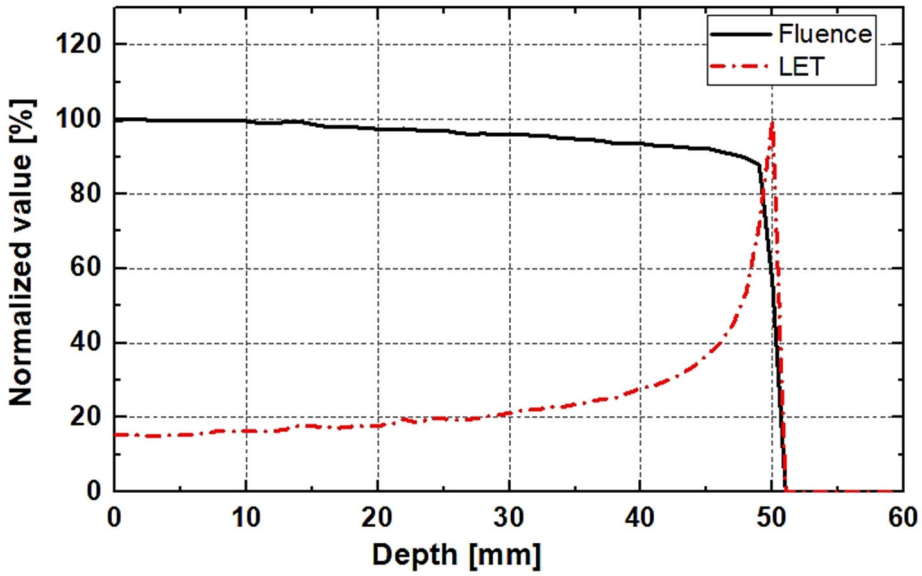

Figure 2.10: The normalized 1D profile of the fluence and the LET curves obtained for the 80 MeV proton beam.

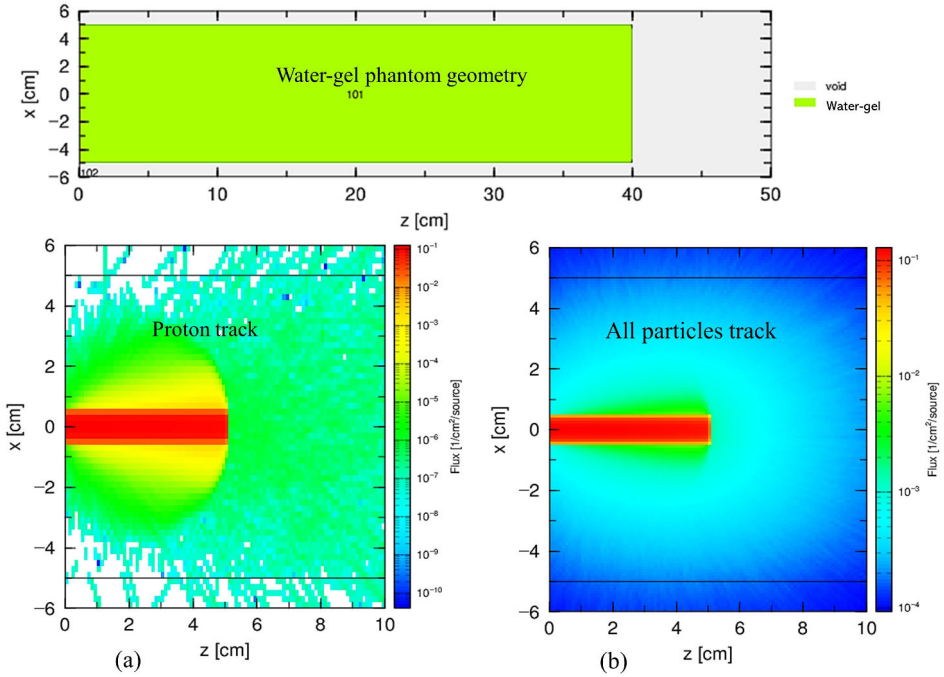

Figure 2.11: Track of particles in the water-gel for 80 MeV of incident proton energy; (a) for only proton, (b) for all particles. The geometry of the water-gel phantom shown at top. The z-axis represented as depth and x-axis for lateral distance.

Depth dose profile

Figure 2.12 shows the normalized 1D, 2D, and 3D profiles of dose vs. depth for the energies 80, 160, and 240 MeV, respectively. Based on the PHITS data, the protons range of three different incident energies in water-gel was calculated shown in Table 2.4. The range of the proton beam primarily depends on the incident proton energy, density, atomic number and mean ionization energy of the media traversed. The calculations were performed using three different energies of 80, 160, and 240 MeV emitting along the positive z-axis from a circular source with a diameter of 1.0 cm. The source was used to irradiate the water-gel phantom, and the results were obtained using the PHITS MC package.

Table 2.4: Proton range for the three different incident energies in water-gel.

Energy (MeV)	Range (mm)
80	59
160	199
240	389

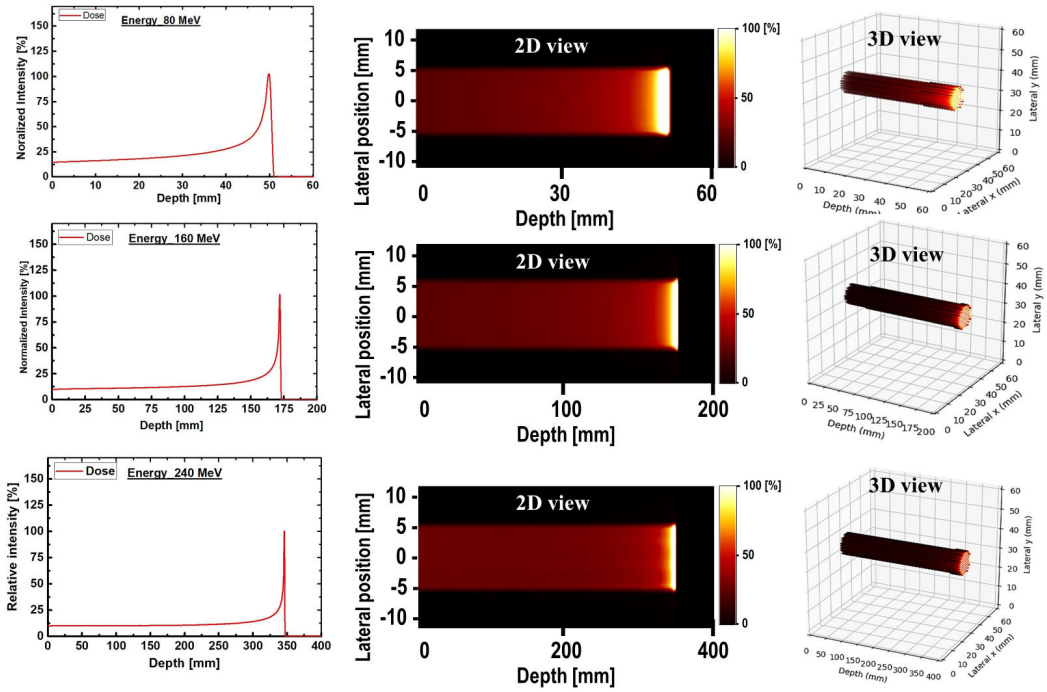

Figure 2.12: The 1D (first column), 2D (second column), and 3D (third column) dose distribution with depth obtained along incident beam direction for 80 (first row), 160 (second row), and 240 (third row) MeV incident proton energies, respectively.

Depth activity profile

The normalized distributions of positron emitting radioisotopes ^{15}O, ^{11}C, and ^{13}N were calculated along the incident proton beam. Figure 2.13 shows the normalized 1D profile of activity vs. depth for the energies 80, 160, and 240 MeV, respectively. And the Figure 2.14 shows the 2D and 3D distributions of positron emitting radioisotopes ^{15}O, ^{11}C , and ^{13}N obtained along incident beam direction, immediately after proton irradiation (i.e., t = 0) for only 80 MeV incident proton energy. The presented activities of ^{11}C ($T_{1/2} \approx 20$ minutes), ^{13}N ($T_{1/2} \approx 10$ minutes) and ^{15}O ($T_{1/2} \approx 2$ minutes) are immediately (at time t = 0) after proton irradiation. As shown in Figure 2.13, the production of ^{15}O and ^{11}C decreased before the Bragg peak and in the fallout before the Bragg region. However, the production of ^{13}N generated a peak near the Bragg peak region. The primary reason causing the earlier decline of ^{15}O and ^{11}C as compared with ^{13}N was that the threshold energy for the production of ^{11}C (20.61 MeV) and ^{15}O (16.79 MeV) was higher than that for ^{13}N (5.660 MeV). It is noteworthy that upon the interaction of protons with matter, the proton will lose energy; therefore, lower energy protons are to be expected in the deeper region of the water-gel phantom. At superficial depths, more high-energy protons will be present; therefore, the required threshold energy for ^{15}O and ^{11}C production will

be satisfied. However, as the depth increases and the proton energy decreases, the dominant production reaction will be ^{16}O(p,2p2n)^{13}N, which has a relatively lower threshold energy. Hence, the byproduct of this reaction (i.e., ^{13}N) is expected to be closer to the Bragg peak region.

Figure 2.15 shows the 2D time-course images of the simulated data only for 80 MeV incident proton energy covering 15 to 55 minutes. This time-course profile can help for long data acquisition process of real PET experiment a well as data analysis using spectral analysis approach. A scaling factor similar to that used to obtain the results shown in Figure 2.13 was used in this case, and the y-axis of the 1D profiles was labeled as the normalized intensity. The short-lived ^{15}O ($T_{1/2} \approx 2$ minutes) nuclei spectrum vanished almost completely after 30 minutes in the time-dependent profile data. The primary observable peak that was similar to the Bragg peak originated from the ^{13}N ($T_{1/2} \approx 10$ minutes) nuclei. In fact, the peak from the ^{13}N nuclei was present for most of the simulated time values up to 55 minutes. It is arguable that such long time durations (e.g., 55 minutes) will not benefit therapeutic applications; however, it is interesting to observe the presence of a ^{13}N peak up to 55 minutes intervals and the dominance by the long-lived ^{11}C ($T_{1/2} \approx 20$ minutes) radioisotopes for long time duration.

The 1D and 2D dose-activity profiles along incident beam direction, just after irradiation for energy modulated (70-80) MeV SOBP distributions of the homogeneous water-gel phantom are shown in Figure 2.16. The SOBP produced by adding for beams of different ranges. The highest energy, which constitutes the distal edge of the SOBP, is attributed the highest weight. In Figure 2.16 all the 10 beams are weighted in order to obtain an SOBP when the beams are added.

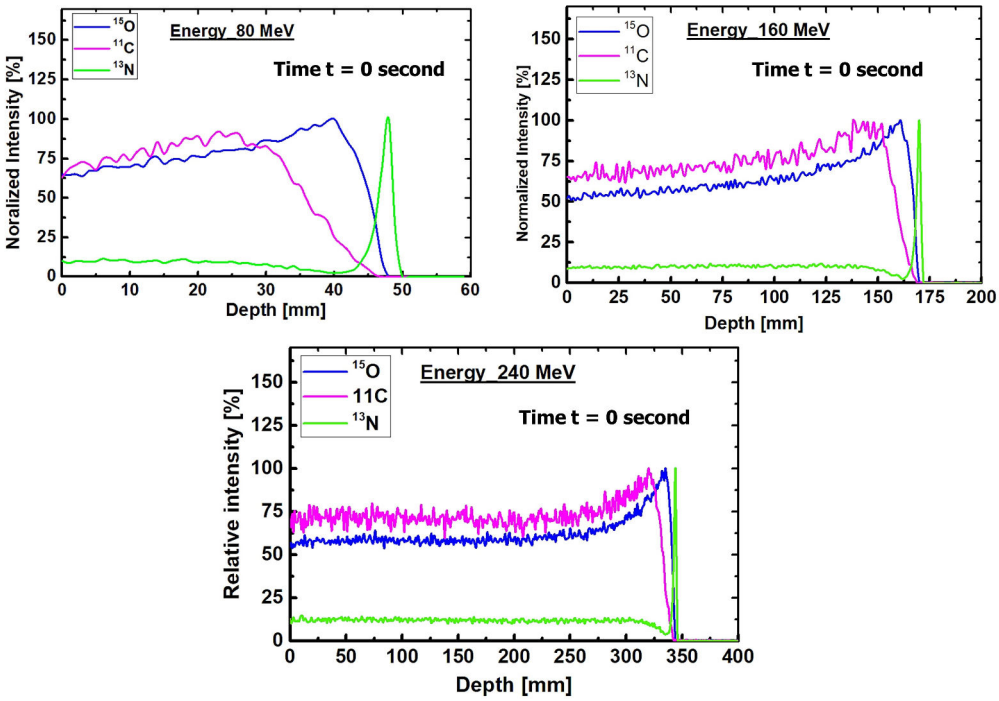

Figure 2.13: The 1D normalized distribution of positron emitting radioisotopes obtained along incident beam direction, immediately after proton irradiation (i.e., t = 0) for 80 (top-left), 160 (top-right), and 240 (bottom) MeV incident proton energies.

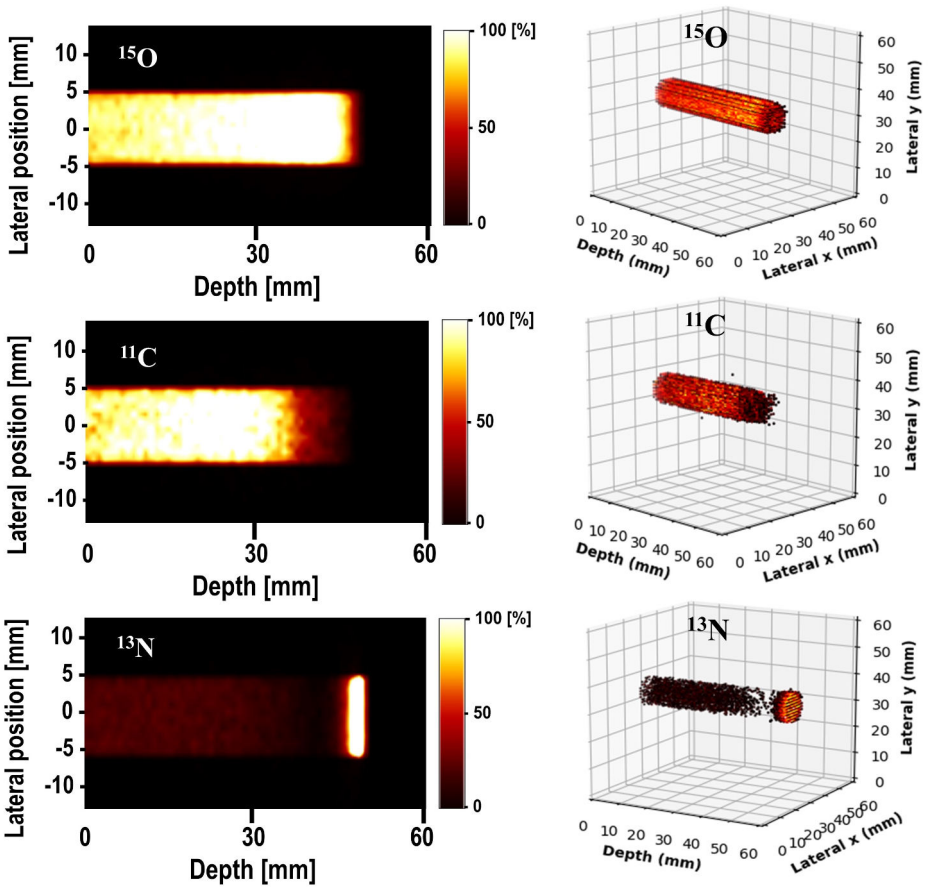

Figure 2.14: The 2D (left column) and 3D (right column) distributions of positron emitting radioisotopes ^{15}O (first row), ^{11}C (second row), and ^{13}N (third row) obtained along incident beam direction, immediately after proton irradiation (i.e., t = 0) for only 80 MeV incident proton energy.

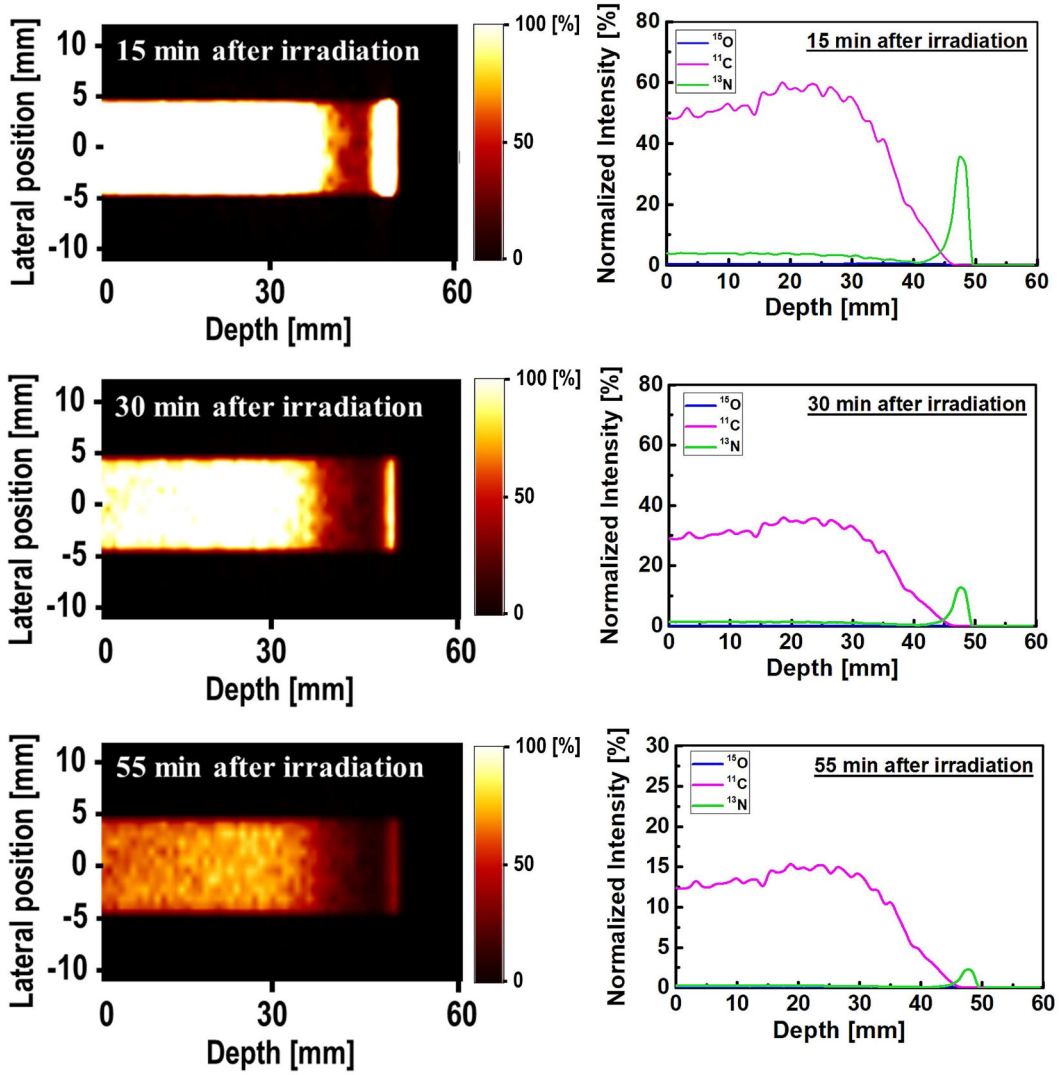

Figure 2.15: The 2D and 1D time-course activity in a range of 15 to 55 minutes of ^{15}O, ^{11}C, and ^{13}N positron emitters produced in the homogeneous phantom only for 80 MeV incident proton energy.

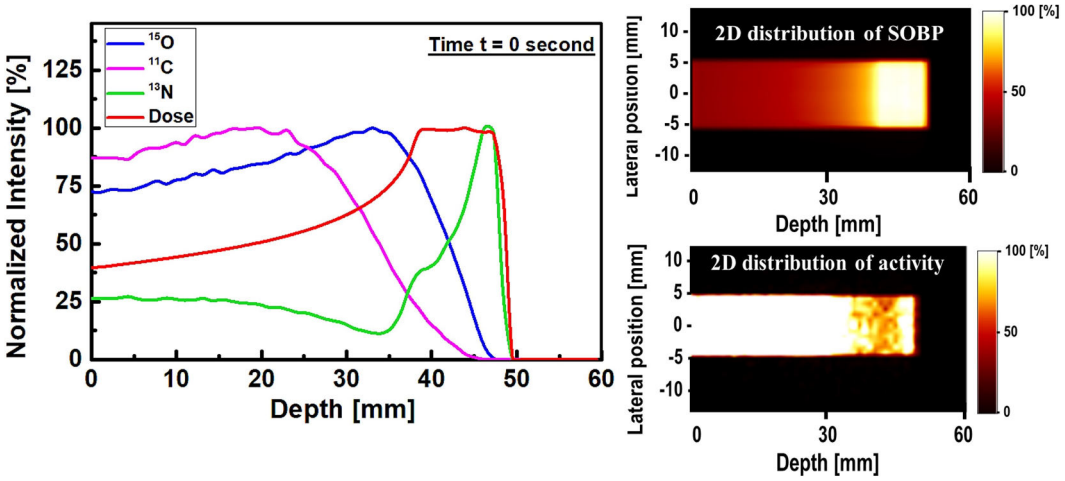

Figure 2.16: The 1D and 2D dose and activity profile with depth for a spread-out Bragg peak plotted with proton beam energies from 70 to 80 MeV in homogeneous water-gel phantom.

Bragg peak offset

Considering the Bragg peak and the peak at which the ^{13}N radioisotope was created, the distance offset was calculated to be 2.0, 2.0, and 2.0 mm for 80, 160, and 240 MeV, respectively are shown in Figure 2.17. In other words, the depths at which the Bragg peak and the peak from ^{13}N were observed were 49.8 and 47.8 for 80 MeV, 171.9 and 169.9 mm for 160 MeV, and 345.9 and 343.9 mm for 240 MeV of incident proton energies, respectively. The deviation or the distance offset between the Bragg peak and the ^{13}N peak was likely due to the threshold energy for the ^{16}O(p,2p2n)^{13}N reaction. Based on the definition of the Bragg peak, it is clear that the dose reaches its maximum value at a depth near the end of the particle range, which implies that the incident particle energy will reach its minimum and be lower than 5.660 MeV (i.e., ^{13}N produces the reaction threshold energy). Therefore, the peak from ^{13}N and the actual Bragg peak would be located at different depth positions in the water-gel phantom. However, our calculations show that the offset distance was insignificant.

Because an offset was present between the generated ^{13}N peak and the actual Bragg peak, a wider incident proton energy range should be considered to precisely verify the distance offset. Therefore, the developed 'PeakCalib' model (details about it in Appendix-A [A.4] was used to investigate the distance offset for incident proton energies ranging from 45 to 250 MeV with an interval of 5 MeV. This energy range encompassed the most widely used proton energies used in therapeutic applications. For simplicity, they were obtained immediately after proton irradiation (t = 0). The obtained numerical results for the actual Bragg peak, ^{13}N peak location, and distance offset (Bragg peak location – ^{13}N peak location) are shown in Table 2.5.

Table 2.5: Comparison between actual Bragg peak and ^{13}N peak location in water-gel phantom with offset distance (Bragg peak location – ^{13}N peak location)

Energy (MeV)	Bragg peak (mm)	^{13}N peak (mm)	offset (mm)
45	17.0	15.0	2.0
50	21.0	19.0	2.0
55	25.0	23.0	2.0
60	29.5	28.0	1.5
65	34.0	32.0	2.0
70	39.0	37.0	2.0
75	44.0	42.0	2.0
80	50.0	48.0	2.0
85	56.0	54.0	2.0
90	62.0	60.0	2.0
95	68.0	66.0	2.0
100	75.0	73.0	2.0
105	81.5	80.0	1.5
110	88.5	87.0	1.5
115	96.0	94.0	2.0
120	103.5	102.0	1.5
125	110.5	109.0	1.5
130	119.0	117.0	2.0
135	127.0	126.0	1.0
140	136.0	134.0	2.0
145	145.0	143.0	2.0
150	153.0	152.0	1.0
155	163.0	161.0	2.0
160	172.0	170.0	2.0
165	181.0	180.0	1.0
170	191.0	189.0	2.0
175	201.0	199.0	2.0
180	211.0	209.0	2.0
185	221.0	219.0	2.0
190	232.0	230.0	2.0
195	242.0	241.0	1.0
200	253.0	251.0	2.0
205	264.0	262.0	2.0
210	275.0	274.0	1.0
215	287.0	285.0	2.0
220	298.0	296.0	2.0
225	310.0	308.0	2.0
230	322.0	320.0	2.0
235	334.0	332.0	2.0
240	346.0	344.0	2.0
245	358.0	356.0	2.0
250	371.0	369.0	2.0

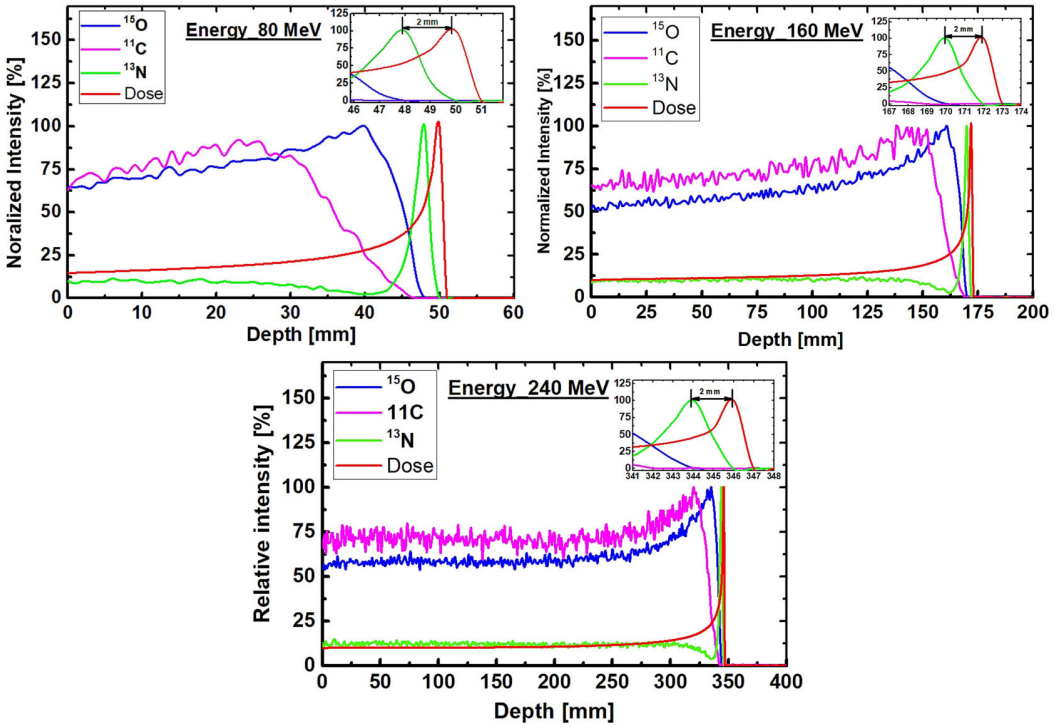

Figure 2.17: Bragg peak and ^{13}N peak location in water-gel phantom with offset distance for 80 (top left), 160 (top right), and 240 (bottom) MeV incident proton energies.

2.4.2 Inhomogeneous phantoms:

Depth dose and activity profiles

Figure 2.18 shows, the 1D and 2D profiles of the simulated depth dose and positron emitter distributions for the inhomogeneous slab target irradiated with pristine and SOBP fields, respectively. In Figure 2.18, the depth dose has been scaled as way (mentioned as normalized intensity [%]) so it can be plotted alongside the radioisotopes activities. From the Figure 2.18, it is observed the pristine Bragg peak is split into two peaks due to proton beam hardening effect at the interfaces (PMMA/bone-equivalent) region of two different materials. The primary reason is when protons travel through two different tissues, the denser material scatters the particles with greater angles, resulting in more protons ending up in the less dense material. As a result, the distributions are skewed or even double peaked, with the maximum located in the less dense material, as seen in Figure 2.18(a). On the other hand, this beam hardening effect is not observed for the SOBP filed, since many Bragg peak is summed over there.

The obtained results for the pristine and SOBP distribution show ^{11}C is more dominated at the PMMA region specially at the entrance. Since, PMMA has a higher carbon content than other elements, as well as a higher threshold (20.61

MeV) in the $^{12}C(p,pn)^{11}C$ nuclear reaction channel. The higher contribution of ^{15}O in the water region with higher oxygen concentration for the $^{16}O(p,pn)^{15}O$ channel. In that region higher oxygen concentration causes only a minor contribution of ^{11}C through the $^{16}O(p,3p3n)^{11}C$ channel with higher threshold (27.50 MeV). Generally, protons with a higher energy will be more abundant at shallower depths, which will satisfy the threshold energy for ^{11}C and ^{15}O production. At the interfaces (PMMA/bone-equivalent) region the contributions of ^{11}C and ^{15}O are almost equal. It is interesting that at the deeper depth the ^{13}N production is much more than others. In that depth the ^{13}N is produced much more due to the combined contribution from $^{16}O(p,2p2n)^{13}N$ and $^{14}N(p,pn)^{13}N$ which have energy threshold 5.660 MeV and 11.44 MeV, respectively. Due to the fact that protons lose energy during their interaction with matter, lower-energy protons can be expected in more deep-seated regions in inhomonegeous phantom. As a result, the byproduct of this reaction ^{13}N is expected to be more near to the pristine Bragg peak region and inside the SOBP as shown in Figure 2.18.

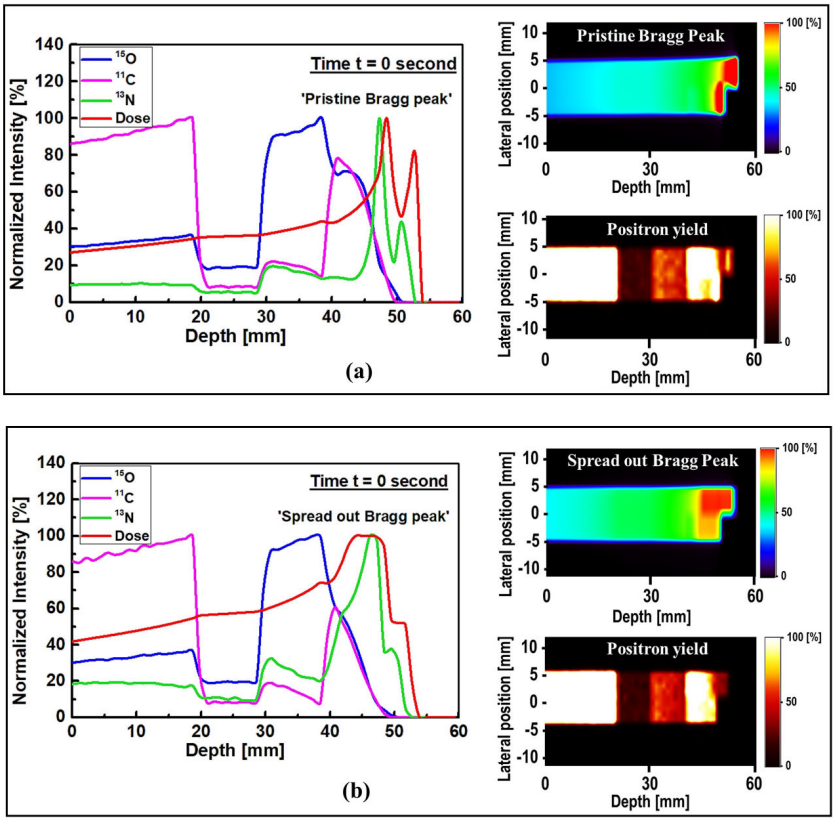

Figure 2.18: The 1D profiles of the simulated depth dose and positron emitting radioisotopes (^{15}O), ^{11}C, and ^{13}N for inhomogeneous slab phantom. The right column shows the 2D profiles of dose deposition and the distribution of the predicted positron emitters; (**a**) for pristine and (**b**) for SOBP distributions.

The results of the proton dose deposition and production of positron emitting radioisotopes (^{15}O, ^{11}C, and ^{13}N) in the modeled MIRD anthropomorphic phantom are shown in Figure 2.19. The distribution of deposited dose and positron emitting radioisotopes along the incident proton beam within the body of anthropomorphic phantom were visualized (see Figure 2.19). The 2D contour plot of dose and positron emitting radioisotopes were obtained and shown in Figure 2.19 (a) and (b). The 1D distribution of deposited dose and positron emit-ting radioisotopes versus depth in the body of MIRD anthropomorphic phantom is shown in Figure 2.19(c).

The dose deposition and production of positron emitting radioisotopes in the body of MIRD anthropomorphic phantom (see Figure 2.19) shows the fact protons interact along the beamline toward the tumor region. As a result of proton interaction and subsequent production of positron emitting radioisotopes through nuclear interaction, positron emitting radioisotopes would be generated. The number of these generated radioisotopes found to be highest along the proton beam, mainly due to higher number of nuclear interactions induced by protons. Interestingly, some of these generated radioisotopes would be dispersed in other regions of modelled MIRD anthropomorphic phantom. The 2D contour plot of deposited proton dose and positron emitting radioisotopes shown in Figure 2.19 (a) and (b), respectively proves the fact that protons would produce positron emitting radioisotopes along their path in the modelled MIRD anthropomorphic phantom. The offset in the final part of the 2D distribution shows the effect of beam interaction with spherical tumor, as can be seen from the curved end of simulated dose (Figure 2.19a) and positron emitter yield (see Figure 2.19b). The results of the positron emitting radioisotopes obtained in the body of modelled MIRD anthropomorphic phantom and 2D contour plots (i.e., Figure 2.19b) represent the total production of all positron emitting radioisotopes (^{15}O, ^{11}C, and ^{13}N).

In order to distinguish the contribution of each positron emitting radionuclide, the distribution of deposited dose by incident protons and individual tallied positron emitting radionuclide versus depth were obtained and shown in Figure 2.19(c). The distribution of ^{15}O and ^{11}C positron emitting radioisotopes was found to be highest at lower depths, mainly due to higher ^{16}O and ^{12}C contents in the soft tissue and lungs which enhances the ^{16}O(p,pn)^{15}O, ^{16}O(p,3p3n)^{11}C and ^{12}C(p,pn)^{11}C nuclear reactions. Another important reason would be proton energy, which would be higher at lower depth and in turn satisfy the energy threshold for ^{15}O and ^{11}C producing nuclear reactions. The produced ^{13}N peak is close to the Bragg peak (1 mm) mainly due to its low energy threshold. The offset between the Bragg peak and the generated ^{13}N peak was found to be about $\sim$1 mm, where the Bragg peak and the generated ^{13}N peak are located at 66 and 65 mm, respectively.

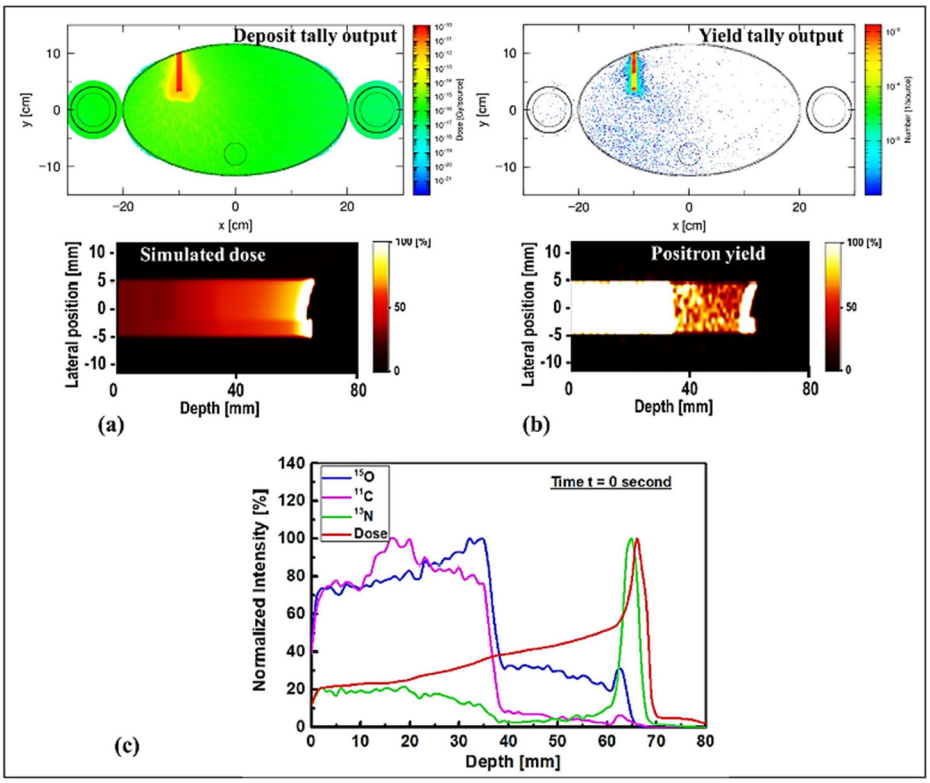

Figure 2.19: The energy deposition (top-left) and production of positron emitting radioisotopes (top-right) obtained in the modeled MIRD anthropomorphic phantom. The 2D distribution of (**a**) dose deposition of protons and (**b**) distributions of positron emitting radioisotopes determined along the incident proton beam track and (**c**) the distribution of deposited dose and positron emitting radioisotopes versus depth in the body of MIRD anthropomorphic phantom.

The ultimate goal of the present feasibility study is to apply the developed methods for realistic PET data obtained after proton irradiations. In realistic PET measurements of the signal produced by the positron emitting radioisotopes (^{15}O, ^{11}C, and ^{13}N), the detected signal will originate from different radioisotopes. In addition, the inhomogeneities of the target could in fact complicate the task of separating the signals from different positron emitting radioisotopes. Therefore, it would be pertinent to deconvolute these to obtain the ^{13}N peak for proton range monitoring and verification. To achieve this, the SA technique was applied to the simulated data for ordinary slab and MIRD anthropomorphic phantoms.

The obtained data for ordinary slab and MIRD anthropomorphic phantoms was converted into time-course images; this can be helpful for lengthy data acquisition process in realistic PET experiments. Figure 2.20 shows the 2D and a 1D time-course activity in a range of 15 to 55 minutes for ^{15}O, ^{11}C, and ^{13}N positron emitter radioisotopes in the inhomogeneous phantom for pristine and SOBP distributions,

respectively. In Figure 2.20, the y-axis of the 1D profiles was labeled as the relative intensity. Similar scaling factors were used to get the results (see in Figure 2.18). In the time-course profile data, the relatively short-lived ^{15}O spectrum which has half life 2.03 minutes almost vanished entirely after 20 minutes. A peak of ^{13}N near to real Bragg peak region from the combined contribution of ^{14}N(p,pn)^{13}N and ^{16}O(p,2p2n)^{13}N nuclear reaction channels which has a half-life of 9.93 minutes has been observed to decay over time, but remain visible for up to 55 minutes. Moreover, the activity of ^{11}C is the most dominated due to longer half-life about 20.33 minutes. But, the ^{11}C production decreased before to the real Bragg peak and in the fallout region, due to higher threshold energy.

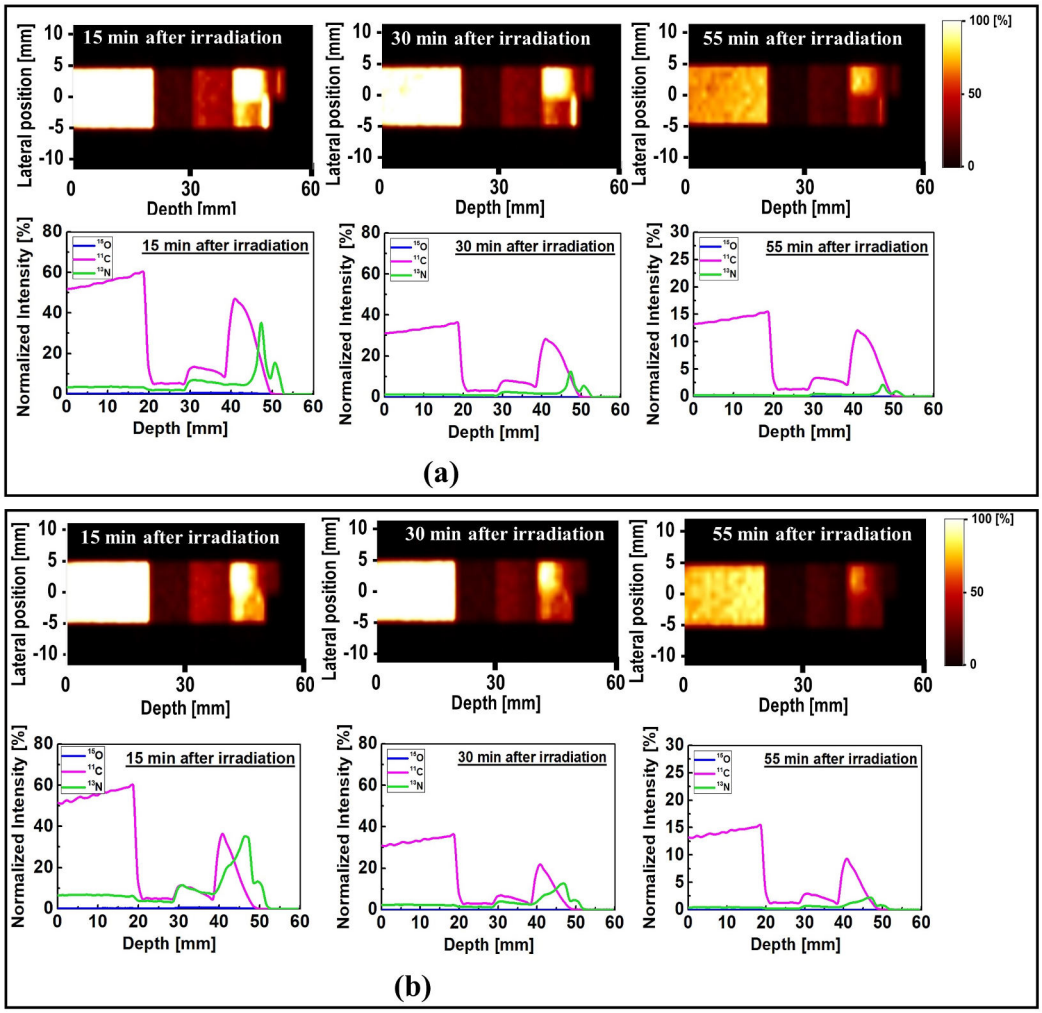

Figure 2.20: The 2D and 1D time-course activity profiles in a range of 15 to 55 minutes of ^{15}O ^{11}C, and ^{13}N positron emitters in the inhomogeneous slab phantom; (**a**) for pristine and (**b**) for SOBP distributions.

The 1D and 2D time-course activity in the time range of 15 to 55 minutes for ^{15}O

^{11}C, and ^{13}N positron emitting radioisotopes in the MIRD anthropomorphic phantom is shown in Figure 2.21. The y-axis of the 1D profiles was labeled as the relative intensity. Similar scaling factor as shown in Figure 2.19 was used. Similar to the time-course activity of inhomogeneous slab phantom shown in Figure 2.20, the relatively short-lived ^{15}O positron emitting radioisotopes were vanished 15 minutes after the irradiation and was not visible for longer time frames (i.e., t > 15 minutes). The spectrum of ^{11}C radionuclide was also found to be dominant in MIRD anthropomorphic phantom, as discussed this is mainly due to its long half-life of 20.33 minutes. However, the interesting difference in the spectrum of ^{11}C in ordinary slab and MIRD anthropomorphic phantoms is the shape of this spectrum. The shape of ^{11}C spectrum is rather more complex in the inhomogeneous slab phantom mainly due to presence of multiple domains with different sizes and material compositions. However, for the MIRD anthropomorphic phantom, the geometrical changes along the incident proton beam in more subtle given that protons experience lesser geometrical and chemical composition changes along their track when passing through thin layer of skin, soft tissue and ribs to reach the tumor region. Similarly, the spectrum of ^{13}N was found to be visible at higher depths and stayed detectable up to 55 minutes after the proton irradiation (see Figure 2.21). These results show that it would be possible to detect ^{13}N peak for proton range verification in realistic clinical applications by deconvoluting signals from different positron emitting radioisotopes using our proposed SA technique.

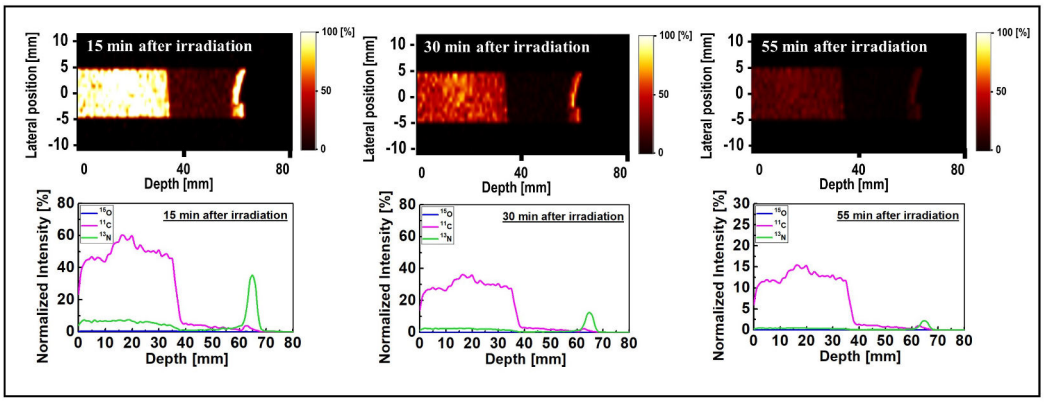

Figure 2.21: The 2D and 1D time-course activity profiles in a range of 15 to 55 minutes of ^{15}O ^{11}C, and ^{13}N positron emitters in the MIRD anthropomorphic phantom irradiated 80 MeV monoenergetic proton beam.

2.5 Conclusions

This chapter focused on the PHITS Monte Carlo simulation packages and their use in producing positron emitting radioisotopes in various configured geometries. The MC method with the PHITS package was used to generate positron emitting radioisotopes, namely ^{15}O, ^{11}C, and ^{13}N in the simulated homogeneous, inhomogeneous slab , and MIRD anthropomorphic phantoms. The performance of the code was examined by examining the fluence, LET, and particle track just for the 80 MeV of incident proton energy in the homogeneous phantom investigations. For the homogeneous studies with various incident proton energies, i.e., 45–250 MeV, a significant ^{13}N peak was found and compared to the actual Bragg peak, which is relevant for therapeutic applications. The offset distance between the ^{13}N peak and the actual Bragg peak was primarily due to the threshold energy of the ^{16}O(p,2p2n)^{13}N nuclear reaction. The inhomogeneous slab phantom studies show how changing the material density causes a shift in the depth dose distribution for the pristine filed. At the distal end of the dose profile, the starting point of the rapid dose falloff is shifted to a shallower depth after traversing the bone volume. The dose deposition and production of positron emitting radioisotopes in the MIRD anthropomorphic phantom's body demonstrate that protons interact along the beam-line toward the tumor region. The number of these radioisotopes produced was found to be highest along the proton beam. The generated ^{13}N peak in inhomogeneous targets such as slabs and MIRD humanoid phantoms is relatively close to the actual Bragg peak. The time-course activity in the time range 15 to 55 minutes for ^{15}O, ^{11}C, and ^{13}N were generated and the spectrum of ^{13}N was found to be visible at higher depths and stayed detectable up to 55 minutes after the proton irradiation. While the relatively short-lived ^{15}O spectrum which has half-life 2.03 minutes almost vanished entirely before 30 minutes after the irradiation. Moreover, the activity of ^{11}C is the most dominated at the shorter depth due to longer half-life about 20.33 minutes. For each case, 3D images were created in order to better visualize the Bragg peak and the other peaks from the proton induced radioisotopes. The 3D visualizations would benefit in the investigation of real inhomogeneous organs (those with irregular geometries) such as the human body's lungs, head, and neck. The simulated acquisition data obtained from the homogeneous water-gel phantom studies used for the experimental studies in Chapter 3.

Chapter 3

Detection of positron annihilation photons by PEM

3.1 Device for detecting positron annihilation photons

The experimental results of a positron emission mammography (PEM) for proton beam range verification are presented in this chapter. The results of studies using a water-gel phantom irradiated with proton pencil beams in a cyclotron beam port are presented. A PEM has the same mechanism as a positron emission tomography (PET), but with higher resolution and sensitivity. A PET scan can detect photons/γ-rays from the annihilation of positrons, which are emitted following the decay of certain radioisotopes produced as nuclear reaction products, such as ^{15}O, ^{11}C, and ^{13}N.

The MC simulations studies discussed in the Chapter-2 demonstrated that among the other positron emitter radioisotopes (such as, ^{15}O and ^{11}C) the ^{13}N has produced a peak near the end-of-range of the proton beam as a result of a ^{16}O(p,2p2n)^{13}N nuclear reaction due to low threshold energy of 5.660 MeV which can be used for proton range verification.

In this chapter, experimental setup and results are presented for a proton induced positron annihilation photons detection system. The dual-head PEM (PEM-GRAPH) system, phantom irradiation and data collecting system, and data analysis methods are described first. The energy spectrum and time-course of the positron annihilation photon events are then analyzed in 1D, 2D, and 3D visualization.

3.2 Dual-head PEM

A prototype dual-head PEM (PEMGRAPH) was developed with the collaboration of Mirai Imaging Inc., Fukushima, Japan. The PEMGRAPH system is a highly sensitive and high-resolution open dual-head system [Yoshikawa et al., 2010] that consists of two planar 17.5 cm $\times$ 21.3 cm detector heads, each composed of four modules. There are a total of eight modules implemented in this device. The gap between each module was 0.6 cm. Each module was composed of 20 $\times$ 64 crystal array of Pr:LuAG with dimensions of 0.21 cm $\times$ 0.21 cm $\times$ 1.5 cm and was optically isolated by a $BaSO_4$ reflector with a thickness of 0.1 cm. This adds up to a total of 20 $\times$ 64 $\times$ 8 = 10,240 Pr:LuAG crystal segments. Each side of the crystal matrix was optically coupled to three units of a 5.2 cm $\times$ 5.2 cm Hamamatsu H8500 position-sensitive photomultiplier tube (Hamamatsu Photonics Co., Ltd., Hamamatsu, Japan). The spatial resolution was 0.2 cm (at full width at half maximum (FWHM)) in the plane parallel to the detectors. The illustration of the prototype PEMGRAPH with detector components are shown in Figure 3.1. The schematic view of data acquisition system is shown in Figure 3.2. The system network of the PEMGRAPH shown in Figure 3.3.

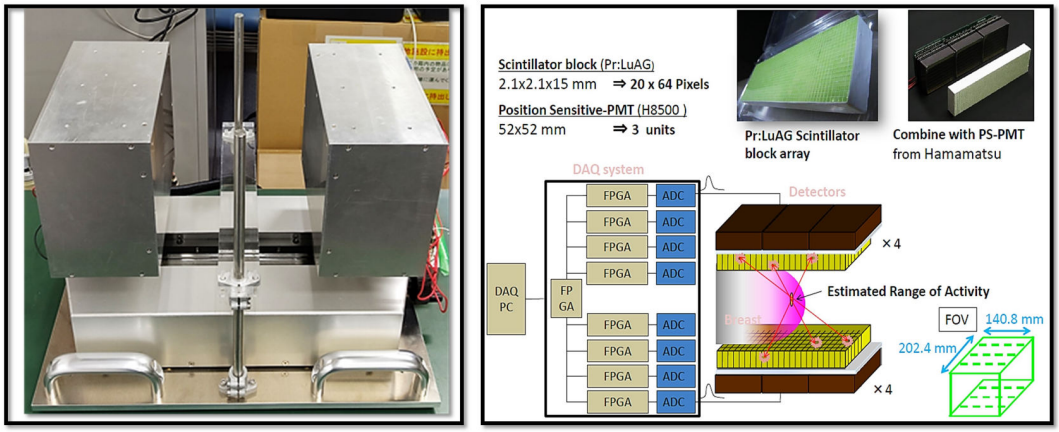

Figure 3.1: Illustration of the prototype PEMGRAPH system (left image) with detector components (right image).

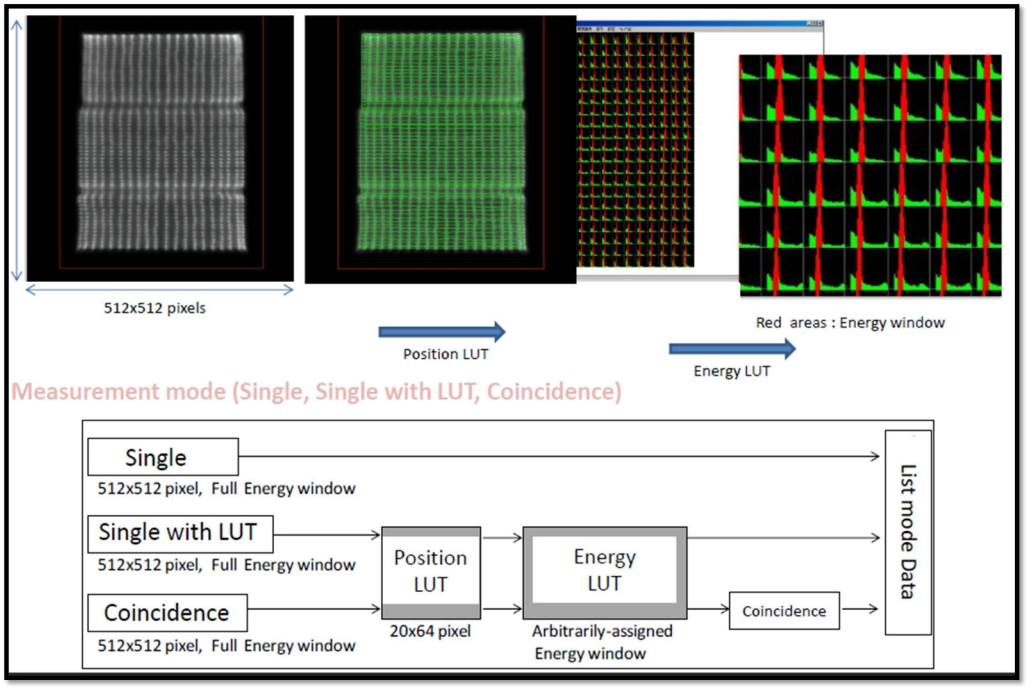

Figure 3.2: The schematic view of data acquisition system.

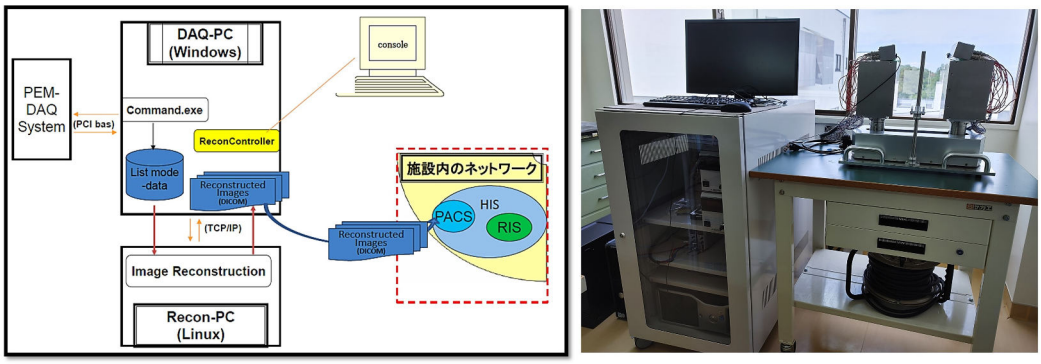

Figure 3.3: The PEMGRAPH system's network, schematic view(left image) and the real one (right image).

3.2.1 Experiments with homogeneous water-gel phantom

A homogeneous water-gel phantom was prepared following the simulation by mixing agar powder ($C_{14}H_{24}O_9$) and water, with a ratio of 1/100 (in gm) (agar powder/water). The container used was high-density polyethylene (HDPE) with dimensions of 8.0 cm $\times$ 10.0 cm $\times$ 16.0 cm and a wall thickness of 0.15 cm. The phantom geometry and PEMGRAPH are schematically shown in Figure 3.4. In addition, the material composition of the water-gel and HPDE container are listed in Table 3.1.

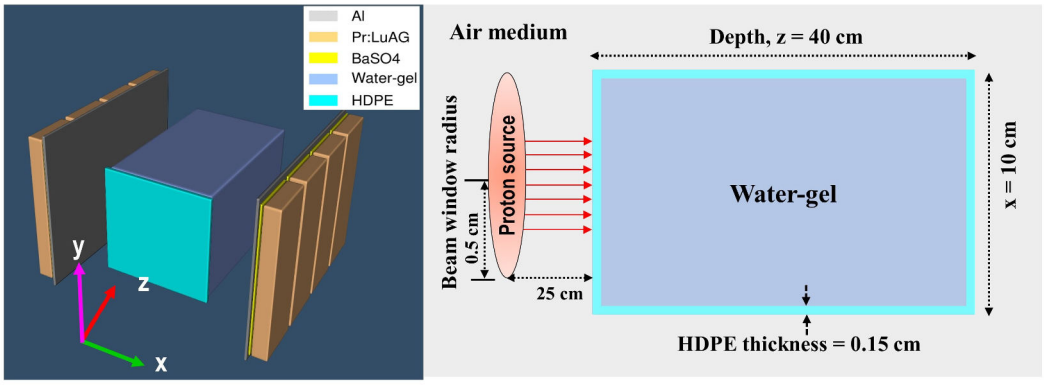

Figure 3.4: The PEM heads and an HPDE box containing water-gel are depicted in this schematic diagram.

The phantom was irradiated by a monoenergetic proton beam with 80 MeV energy for 60 s. The proton beam was pencil-like with a beam current of 10.20 nA and a diameter of $\sim$ 1.0 cm produced by an azimuthally varying field (AVF) cyclotron at the Cyclotron and Radioisotopes Centre (CYRIC) facility at Tohoku University, Japan. Considering the current that was used, about 3.8 $\times$ 10^{12} protons were used to irradiate the phantom. This value was higher than the typically used clinical beam, which was reported to be around 10^7 to 10^{10} protons. To obtain more counts during the PEM scan, more protons were used than in clinical irradiation. It is also well known that proton induced activity only depends on the target fragmentation. The experimental setup for the irradiation of the water-gel phantom is shown in

Table 3.1: Material composition and density (fraction by weight) of the HDPE container and water-gel used in the proton irradiation experiment.

Material	Density (g cm^{-3})	^{1}H (%)	^{12}C (%)	^{16}0 (%)
HDPE box	0.950	14.29	85.71	-
Water-gel	1.010	11.00	4.650	84.35

Figure 3.5 (a). The distance between the proton beam port and water-gel phantom was set to 25.0 cm. The proton beam was adjusted to irradiate the center of the water-gel phantom.

After proton irradiation, the irradiated water-gel phantom was placed in the PEMGRAPH system; this setup is shown in Figure 3.5 (b). The irradiated water-gel phantom was scanned for 40 minutes with the PEMGRAPH system. The scanning of the irradiated water-gel phantom was started 15 minutes after the irradiation, mainly due to the time taken to carry the phantom from the irradiation room to the PEMGRAPH room after stopping the proton beam irradiation.

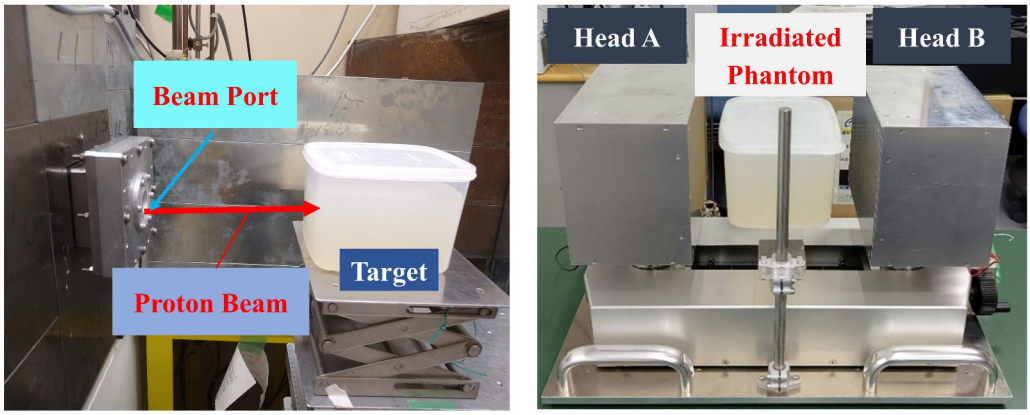

Figure 3.5: Experimental setup. (**a**) Water-gel phantom irradiation by a pencil-like proton beam with an energy of 80 MeV. (**b**) Scanning the irradiated water-gel phantom using a dual-head PEMGRAPH system.

The acquired list mode data were reconstructed to dynamic frames using the 3D iterative maximum likelihood-expectation maximization (MLEM) method [Shepp et al., 1982]. The field of view (FOV) of each reconstructed image was 20.35 cm $\times$ 14.19 cm $\times$ 14.6 cm, and the matrix size was 185 $\times$ 129 $\times$ 73. Therefore, the voxel size of each reconstructed image was 0.11 cm $\times$ 0.11 cm $\times$ 0.2 cm. Same as simulation the experimental data were then analyzed using PyBLD and AMIDE software. The one-dimensional (1D), two-dimensional (2D) and three-dimensional (3D) time-course activities for 15, 30, and 55 minutes after irradiation were obtained, which provided information on the location and distribution of activity.

3.3 Results and discussion

3.3.1 Homogeneous water-gel phantom

In this section the results from the water-gel phantom study with PEMGRAPH are presented. The Figure 3.6 shows the reconstructed PEMGRAPH image 3D (a) and 2D (b) view in DICOM (Digital Imaging and Communications in Medicine) format with background and random counts. On the other hand, the Figure 3.6(c) shows the 2D view only for true count cropped of cps(0-5s) data.

The 1D, 2D, and 3D visualizations of the time-course images are shown in Figure 3.7. These were reconstructed along the beam direction for 15, 30, and 55 minutes. In Figure 3.7, the normalized intensity is displayed along the y-axis. These were normalized with respect to 15 minutes after irradiation. From the images and 1D profiles shown in Figure 3.7, we observed two peaks along the beam direction: one at the proton beam entrance and the other near the distal dose Bragg region. In addition, a tail after the peak of the Bragg region was observed. These peaks decayed with time and remained visible for up to 55 minutes after the irradiation. Interestingly, the tail almost vanished after 30 minutes.

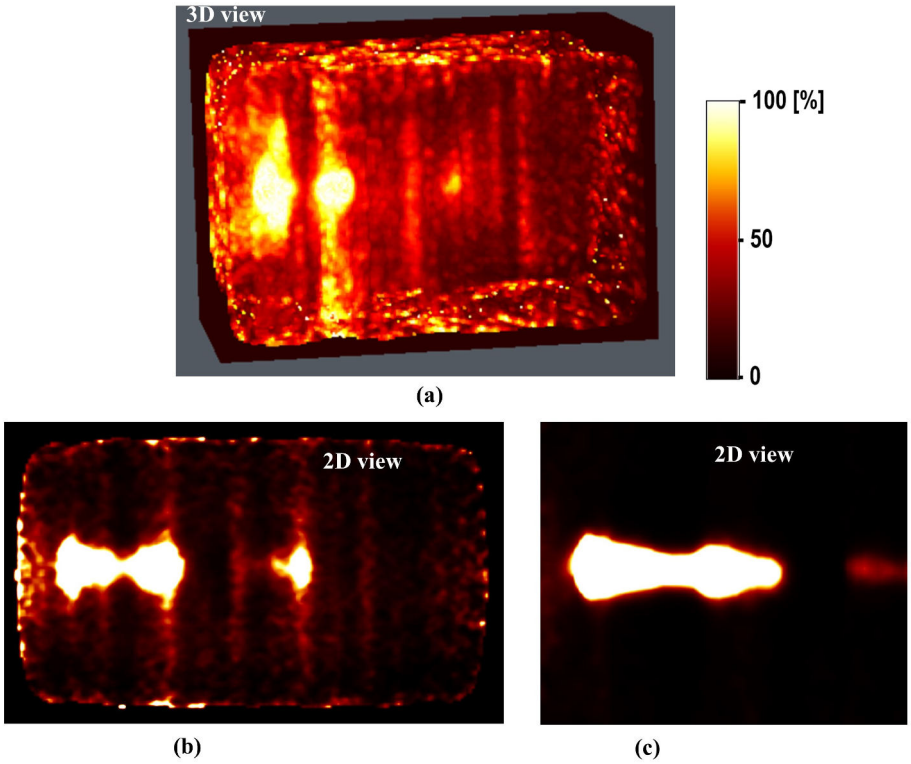

Figure 3.6: Reconstructed 3D (**a**) and 2D (**b**) PEMGRAPH images are shown on the top and left and (**c**) the cropped images for true counts on the right cps(0-5s) .

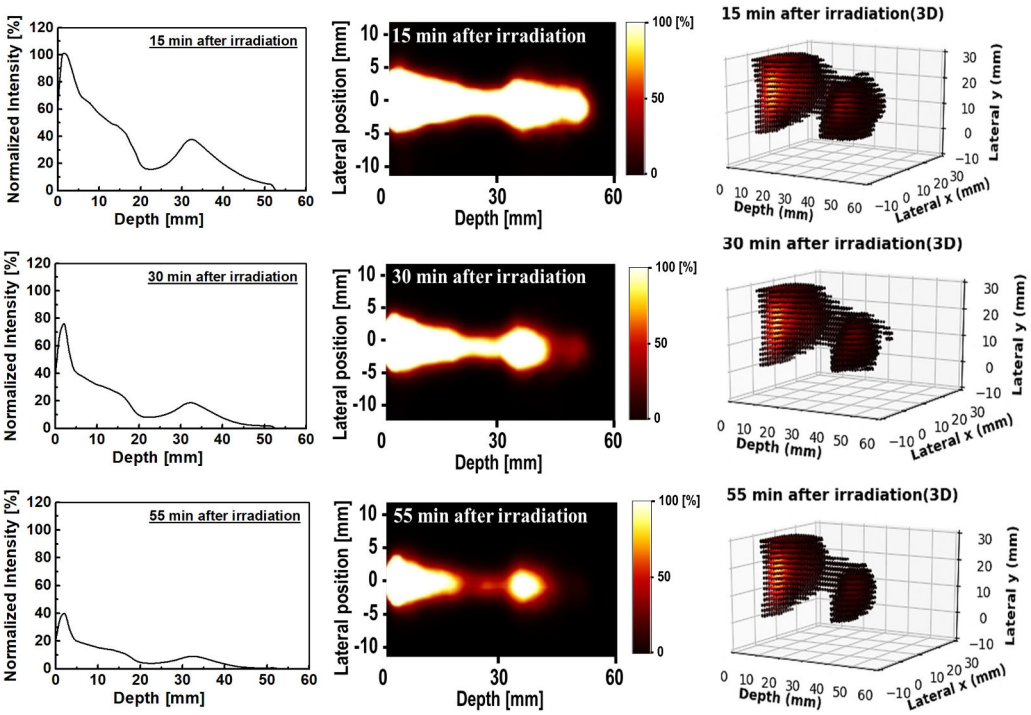

Figure 3.7: The 1D (first column), 2D (second column), and 3D (third column) time-course activity covering 15 to 55 minutes data sets obtained from the PEMGRAPH measurements.

Considering the results shown in Figure 3.7, two peaks can be observed from the PEMGRAPH measurements. In addition to these two peaks, a small tail peak was observed and vanished rather quickly. The main reason for the formation of these peaks was the proton interaction and scattering from the HDPE container used in the proton irradiation experiment; in particular, the wall effect from the HDPE container that mainly contains carbon (note that ^{1}H nuclei do not produce stable positron emitting radioisotopes). Upon the interaction of proton with matter, the protons lose energy, and hence lower energy protons should be found in the deeper parts of the water-gel phantom, and at shallow depths, there will bemore higher energy protons; this satisfies the ^{11}C and ^{15}O threshold energies for their production. The threshold energies for the creation of ^{15}O, ^{11}C, and ^{13}N, were reported to be 20.61, 16.79 and 5.660 MeV, respectively [Cho et al., 2017]. As depth increases and in turn the proton energy decreases, the main production reaction is ^{16}O(p,2p2n)^{13}N, which has a lower threshold energy compared to other positron emitting radioisotopes. The results of the current study agree with those of previous simulations.

3.4 Conclusions

In this chapter, the main features and functions of our developed PEM (PEMGRAPH) has been described. In order to verify the proton beam range, we used highly sensitive PEMGRAPH for the first measurement of the proton induced annihilation annihilation photons. Experiment was performed with the water-gel phantom that irradiated by Cyclotron produced 80 MeV monoenergetic pencil-like protons beam. From the results we found that there are two peaks can be observed from the PEMGRAPH measurements. In addition to these two peaks, a small tail peak was observed at the end of proton beam path and vanished rather quickly. The results of the experiment indicate a good agreement between the simulated and experimental reconstructed images. In the following chapter, a spectral analysis approach will be used to determine what type of radioisotopes were produced and their concentration along the beam path.

Chapter 4

Quantification of proton induced radioisotopes using SA approach

4.1 Spectral Analysis approach

In this work, the results of dynamic positron emission tomography (PET) of proton beam irradiation were examined and presented utilizing an approach known as 'Spectral Analysis'. In dynamic PET studies, the term spectral analysis indicates a single-input/single-output model used for the data quantification. Spectral analysis (SA) allows the quantification of dynamic data by relating the radioactivity measured by the scanner in time to the underlying physiological processes of the investigated system. The SA approach was initially developed in 1993 as a method for mathematical modeling for kinetic analysis of PET studies [Cunningham et al., 1993].

This approach allows a tracer's tissue time-activity curves (TACs) to be described in terms of an ideal subset of kinetic components chosen from a much larger set. It usually consists of convolution integrals of the input function with decaying exponentials, allowing the selected components to be connected to a suitable compartmental model. The SA can be used in a framework where kinetic data is measured in regions of interest (ROI) or single pixels. This approach can apply to both homogeneous and heterogeneous without any previous hypotheses; which makes it useful for the analysis of tracer kinetics of PET data with the limited spatial resolution of the scanner [Turkheimer et al., 1994]. It also provides an estimation of the rate constant of trapping of tracer in the tissue, as well as the amplitudes and decay constants of reversible components. It can also be used to estimate the total volume of distribution of the tracer, which does not depend on the model configuration. However, the spectral analysis technique cannot be used for all linear compartmental systems; a set of conditions must be met in order for it to be used.

In realistic measurements using PET system, the measured signal could be weak and therefore it generates noisy images. There are various ways to circumvent the

issue with weak signal and in turn noise-free PET images. In a recent study, Guo et al. introduced a kernel-graph filtering method that could significantly reduce the amount of noise in PET images caused by weak signal sources [Guo et al., 2021]. The study performed was tested extensively using simulated and real life in-vivo dynamic PET datasets. The authors showed that the proposed method significantly outperforms the existing methods in sinogram denoising and image enhancement of dynamic PET at all count levels, and especially at low counts which measured signal from isotopes are weak. Therefore, the issue with weak signals that may create difficulties in realistic measurements could be solved rather effectively using denoising methods. In addition, the whole body PET scanner is another system that can be used to solve the issue with weak signals; this scanner has 200.0 cm axial field of view (FOV) and 40 times higher sensitivity than conventional PET systems [Vandenberghe et al., 2020].

4.2 Application of the SA approach in proton therapy

Each voxel of the PET image contains several positron emitting radioisotopes because of the interaction between the incident proton beam and the target elements. In this study, the SA approach was applied for quantification of different isotopes of positron emitters such as ^{15}O, ^{11}C, and ^{13}N that are produced by inelastic nuclear interactions of protons with the target elements during proton irradiation.

Considering each radioisotope to be one component at time t, and its time-activity $A(t)$ of each voxel, then the concentration $C_v(t)$ which is expressed by the following equation;

$$C_v(t) = \sum_{j=1}^{M} A(t) \otimes \alpha_j e^{-\beta_j t} \tag{4.1}$$

where α_j and β_j are assumed to be real-valued and nonnegetive. M represents the maximum number of terms to be included in the model (generally between 100 and 1000). The values of β_j are predetermined and fixed in order to cover an adequate range of spectral values. The values of α_j are estimated from the time-activity curves by a nonnegative least squares (NNLS) procedure. Each $A(t) \otimes \alpha_j e^{-\beta_j t}$ (impulse response function (IRF)) is precalculated. When the IRFs are precalculated, then the estimation sets of α_j are entirely linear, and SA can instantly find groups of α_j without repeating the computation.

To extract the shorter half-life or larger β ($0.693/T_{1/2}$) radioisotopes ^{15}O and ^{13}N, a range of β 0.005 (threshold) to 0.006 (betacut) s^{-1}, and 0.001 to 0.002 s^{-1} were used, respectively. Whereas, for longer half-life or smaller β ($0.693/\mathrm{T}_{1/2}$) radioisotope ^{11}C, the range of β 0.0005 to 0.0006 s^{-1} was used. For each voxel v, the numerical

S_v values were then computed using the following equation with a threshold of $\beta >$ 1.5 to eliminate the background region:

$$S_v(t) = \sum_{j=1} \alpha_j \beta_j \tag{4.2}$$

Therefore, the SA method can be applied quickly to calculate the sets of α and β for each voxel.

4.2.1 Scheme for extraction and 3D visualization of positron emitting radioisotopes

The SA approach was used to extract ^{15}O, ^{11}C, and ^{13}N positron emitting radioisotopes from the simulated results as well as PEMGRAPH measured data. These were extracted separately from the merged images in different regions (see Figure 4.1). Firstly, the SA technique was applied to 3D merged images that contained all frames of 40 minutes images (from 15 to 55 minutes). The Appendix-A [A.5] contains the SA and 3D scatter plot scripts. Secondly, the time activity was calculated from the 3D data from the all frames with 1 minutes intervals over 40 minutes using four separate regions of interest (ROIs): (1) whole, (2) edge, (3) plateau and (4) Braggpeak region, as shown in Figure 4.1. Figure 4.1 shows these four regions, together with their corresponding heights, widths and depths, respectively. Then, the time activity data from 15 to 55 minutes were made into a single voxel image for each ROI. The whole process of SA application was done according to the following **scheme**. The presence of proton induced radioisotopes for each voxel was then confirmed using the obtained results.

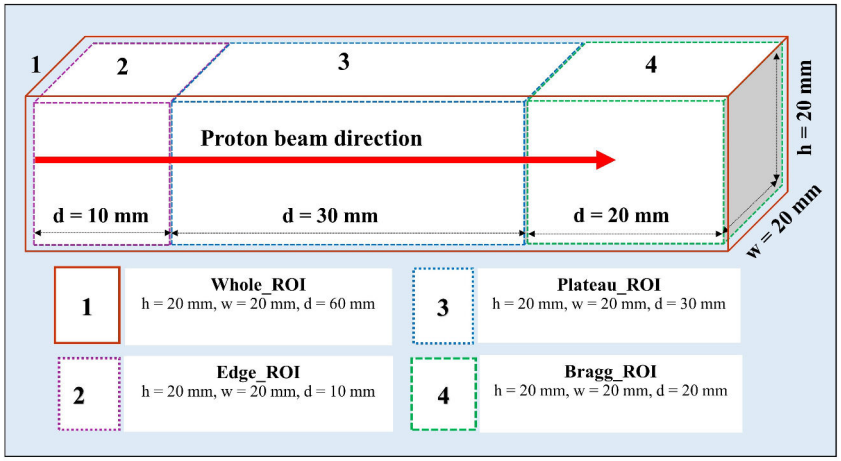

Figure 4.1: An illustration of the four regions of interest (ROIs) and their height (h), width (w) and depth (d) values used in the spectral analysis.

Scheme:

The step-by-step algorithm of the analysis scheme for the extraction and 3D visualization of positron emitting radioisotopes using SA approach from the simulations and PEMGRAPH experimental data as follows:

---

1. Data processing -
   (a) Data processing from the simulation results (in ascii format in a DAT file)
   (b) Data acquisition from the PEMGRAPH system (in ascii format in a DAT file).
   (c) Record the true coincidences as dynamic data from the raw data in case of measured data.
   (d) Sort the data into cps frames for 40 minutes.
2. In case of experiment image reconstruction using the Maximum-Likelihood Expectation-Maximization (MLEM) method (in DICOM format).
3. Convert DICOM data to HDR and IMG format using PyBLD package (using the script
   (a) Extract the 1D profile data in ascii CSV format using python script.
   (b) Plot the extracted 1D profile saved into a CSV file.
4. Merge four decay image frames for visualization of radioisotope distribution with time.
   (a) Crop the merged images in step 4
   (b) Visualize the cropped 2D images using the AMIDE software.
5. Generate the 3D scatter plots. The 3D scatter script uses the mplot3d toolkit and the ax.scatter3D () function of the matplotlib library.
6. Perform spectral analysis on the obtained images-
   (a) The total of all frames of 40 minutes image were merged by the script and saved as simg.img
   (b) Crop the merged images in step '6(a)' using the python script and saved as simg_crop.img.
   (c) The frame images were prepared in step '6(b)' by frame.py script and saved as simg_crop_f.img.
   (d) The mask images were prepared in step '6(c)' by mk_mask.py and saved as simg_crop_fmask.img.
   (e) Generate the time information for all frames of 40 minutes dynamic data as time_inf.frame file.
   (f) Extract the data for positron emitting radioisotopes using python terminal command.
7. python terminal command:

(a) **for ^{15}O radioisotope:**
time python3 spectral_analysis.py -–input = simg.img -–time = time_inf.frame -–output = analysis_o-15 -–mask= simg_crop_mfsimg.img -–betacut = 0.005 —athresh = 0.006

(b) **for ^{11}C radioisotope:**
time python3 spectral_analysis.py -–input = simg.img -–time = time_inf.frame -–output = analysis_c-11 —mask = simg_crop_mfsimg.img -–betacut = 0.0005 -–athresh = 0.0006

(c) **for ^{13}N radioisotope:**
time python3 spectral_analysis.py -–input = simg.img -–time = tim_inf.frame -–output = analysis_n-13 —mask= simg_crop_mfsimg.img -–betacut = 0.001 --athresh = 0.002

(d) Extract the 1D profile data of analysis output in ascii CSV format.

(e) Plot the extracted 1D profile saved into a CSV file.

8. For 1D spectrum the time activity were calculated as tac.dat from 40 frames with 1 minute interval for four ROIs (1) whole, (2) edge, (3) plateau, and (4) Bragg-peak region.

   (a) Generate one voxel images of each ROI's time activity in step '8' for example as onev_whole.img

   (b) Generate the spectrum of radioisotopes using the python terminal command for a whole ROI as:
   time python3 spectral_analysis.py -–input = onev_whole.img -–time = time_inf_roi.frame -–output = analysis_out-whole -–debug = 1

9. Plot the concentration (α) versus half-live (β) from the terminal output of step '8(b)'.

10. Generate the 3D dynamic visualization and movie clips for ^{15}O, ^{11}C, and ^{13}N from step '7'

4.3 Results and discussion

The SA was performed based on the "analysis scheme" to the dynamic time-course activity data findings from simulations and experimental studies. The SA technique was applied to the data set of after 15 minutes of irradiation (from 15 to 55 minutes) considering the offline PET verification.

4.3.1 Simulation studies

The SA was conducted on the simulated results of the homogeneous,inhomogeneous slab, and MIRD anthropomorphic phantoms studies. The results shown in Figures

4.2, 4.3, 4.4, 4.5 and 4.6 show 2D and 3D images with their respective 1D profiles of the SA extracted radioisotopes called SA_^{15}O SA_^{11}C, and SA_^{13}N for homogeneous and inhomogeneous slab and MIRD anthropomorphic phantoms, respectively.

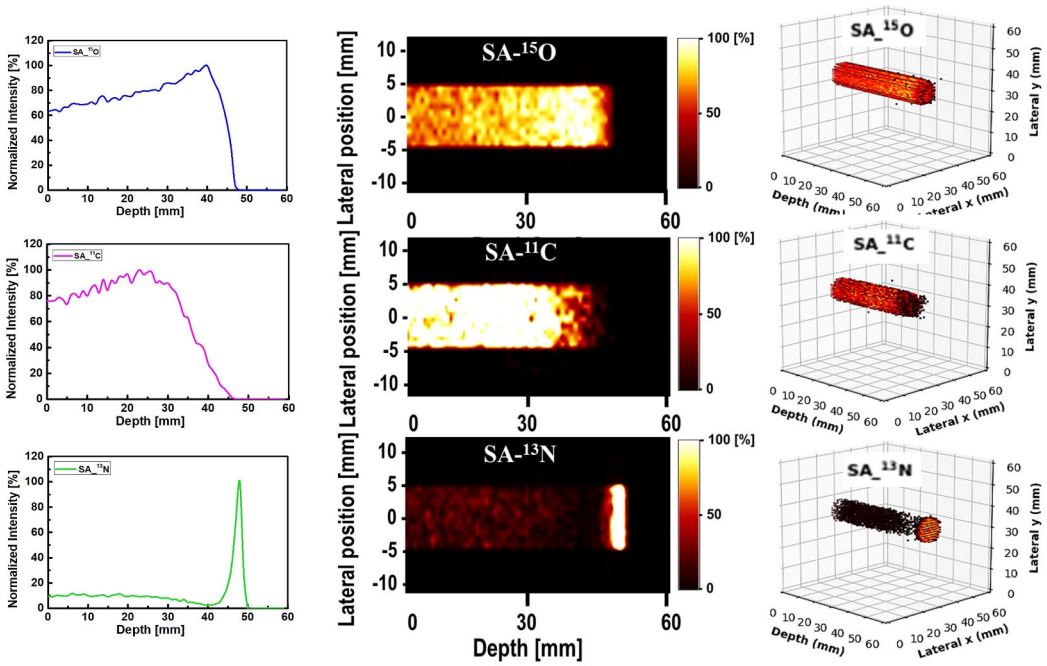

Figure 4.2: The 1D, 2D, and 3D profiles of SA extracted radioisotopes SA_^{15}O (first row), SA_^{11}C (second row), and SA_^{13}N (third row) for the homogeneous phantom that irradiated with 80 MeV pristine proton beam.

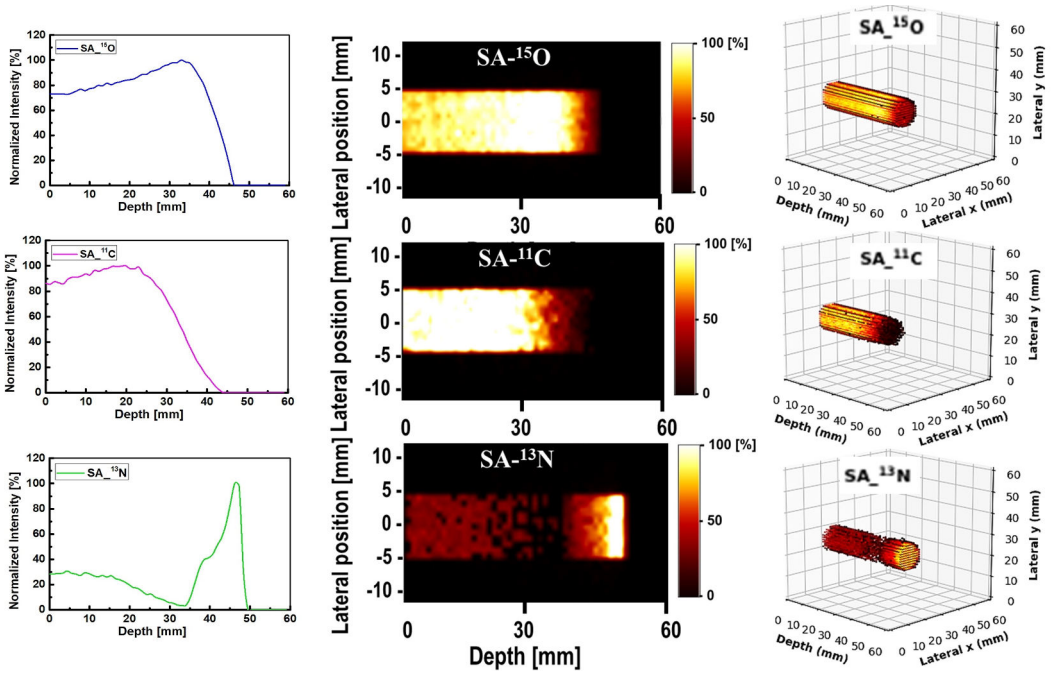

Figure 4.3: The 1D, 2D, and 3D profiles of SA extracted radioisotopes SA_^{15}O (first row), SA_^{11}C (second row), and SA_^{13}N (third row) for the homogeneous phantom irradiated with SOBP fileds.

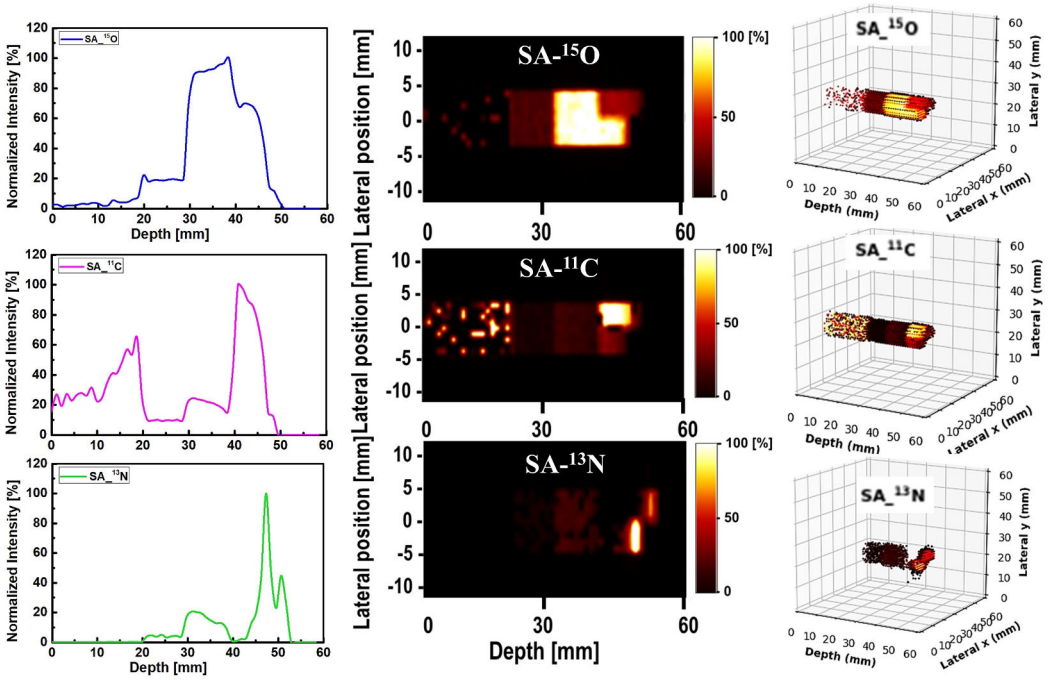

Figure 4.4: The 1D, 2D, and 3D profiles of SA extracted radioisotopes SA_^{15}O(first row), SA_^{11}C (second row), and SA_^{13}N (third row) for the inhomogeneous slab phantom irradiated with 80 MeV beam.

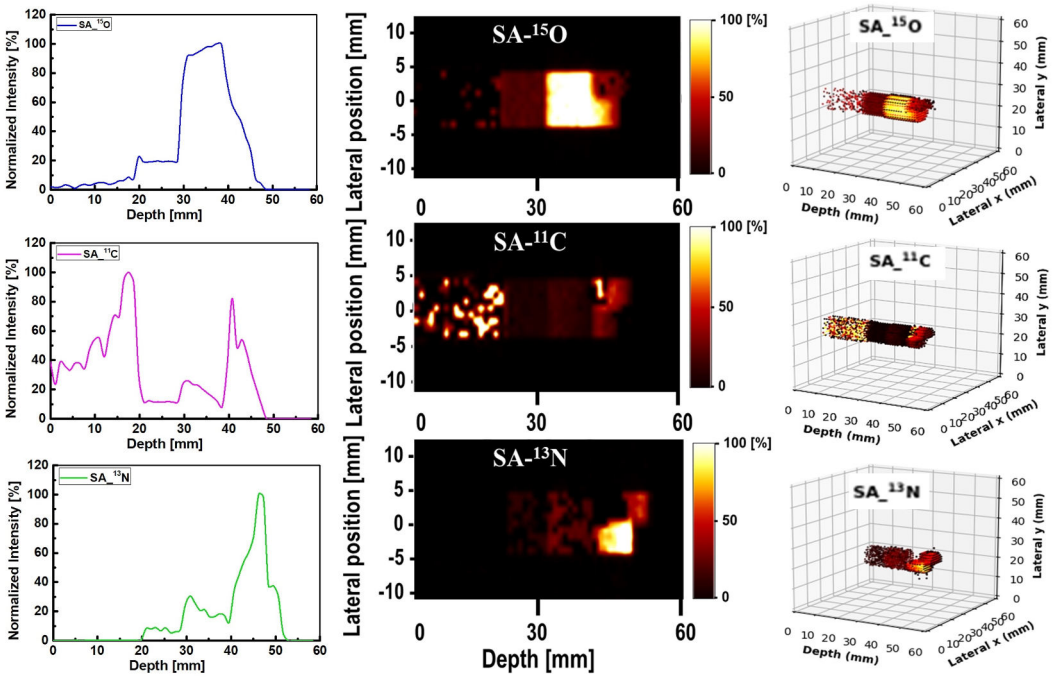

Figure 4.5: The 1D, 2D, and 3D profiles of SA extracted radioisotopes SA_^{15}O (first row), SA_^{11}C (second row), and SA_^{13}N (third row) for the inhomogeneous slab phantom irradiated with SOBP field.

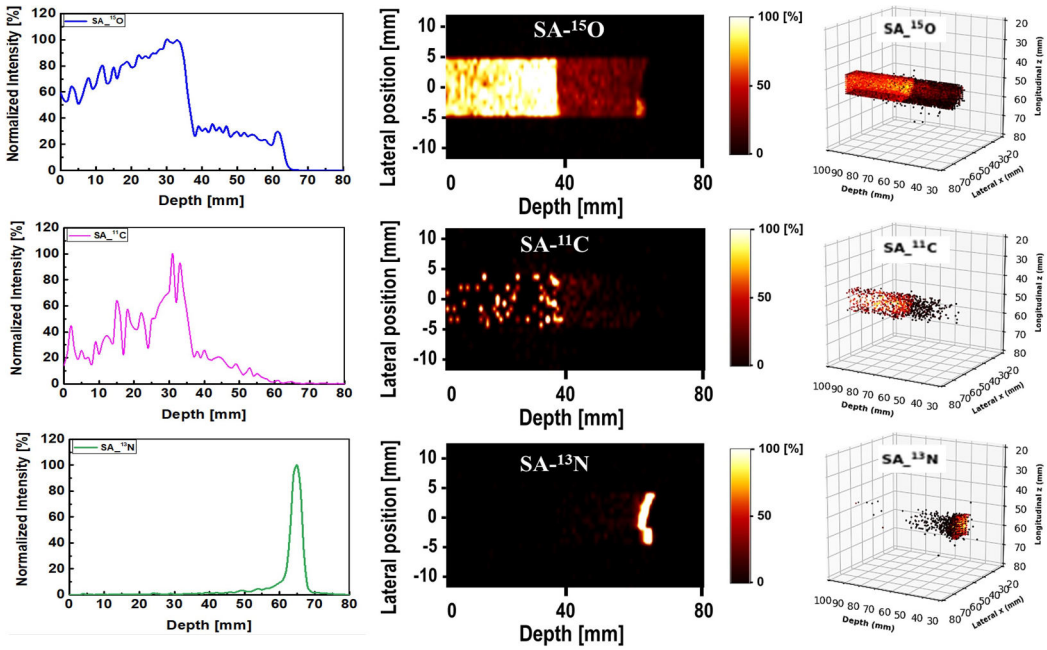

Figure 4.6: The 1D, 2D, and 3D profiles of SA extracted radioisotopes SA_^{15}O (first row), SA_^{11}C (second row), and SA_^{13}N (third row) for the MIRD anthropomorphic phantom irradiated with 80 MeV monoenergetic beam.

The Figures show the SA extracted radioisotopes were consistent with the simulated production that will be compared in the following chapter. The SA technique was also applied to the time-course datasets (from 15 to 55 minutes after irradiation) to predict the half-life of each positron emitting radioisotopes present in the different regions of interest ROIs (see in Figure 4.1). Figures 4.7, 4.8 and 4.9 show ROIs investigating SA results that confirm the half-life of the SA extracted radioisotopes for homogeneous, inhomogeneous slab, and MIRD anthropomorphic phantoms. For all ROIs, the x-axis represents the half-life (i.e., $log(2)/\beta$) for the extracted radioisotopes, and the y-axis represents the concentration of radioisotopes, labeled as normalized α.

Based on the SA results shown in Figure 4.7 for the whole region, it was clear that the majority contribution from ^{11}C and ^{13}N radioisotopes, though ^{11}C larger than ^{13}N. However, the contribution from the ^{15}O radioisotopes was approximately one-half those of ^{11}C and ^{13}N. It is expected as the SA technique was applied to the data set of after 15 minutes off irradiation (from 15 to 55 minutes) considering the offline PET verification the shorter half-life ^{15}O radioisotopes almost vanished out. The SA results of the edge ROI primarily comprised those of relatively long-lived radioisotopes; in other words, the contribution from the long-lived radioisotopes (e.g., ^{11}C) was greater than those of ^{13}N and ^{15}O. Considering the plateau ROI, it was observed that ^{11}C offered the greatest contribution, whereas ^{13}N and ^{15}O indicated similar levels of contribution. Finally, the Bragg-peak ROI indicated the greatest contribution from the ^{13}N radioisotopes, whereas the contributions from ^{11}C and ^{15}O were negligible.

From the Figure 4.8, for the both pristine and SOBP distributions in the inhomogeneous slab phantom it is observed that at the whole, edge and as well as plateau regions, contributions from long-lived radioisotope which half-life almost equal to ^{11}C were dominant. And there is a very few contributions from the relatively short-lived radioisotopes ^{13}N and ^{15}O in these regions. It is expected as in these regions a greater amount of carbon-rich materials PMMA is present, and ^{11}C was produced much more in the MC simulation. On the other hand, in the Bragg peak ROI the greatest contribution from the ^{13}N radioisotope, whereas less contribution from ^{11}C in both cases of pristine and SOBP distributions. The SA approach was applied for quantifying of different radioisotopes at any specific region. It is promising that SA can separate the ^{13}N peak at the distal falloff region among from other radioisotopes ^{13}N and ^{15}O; this method would be useful for analyzing the experimentally obtained data.

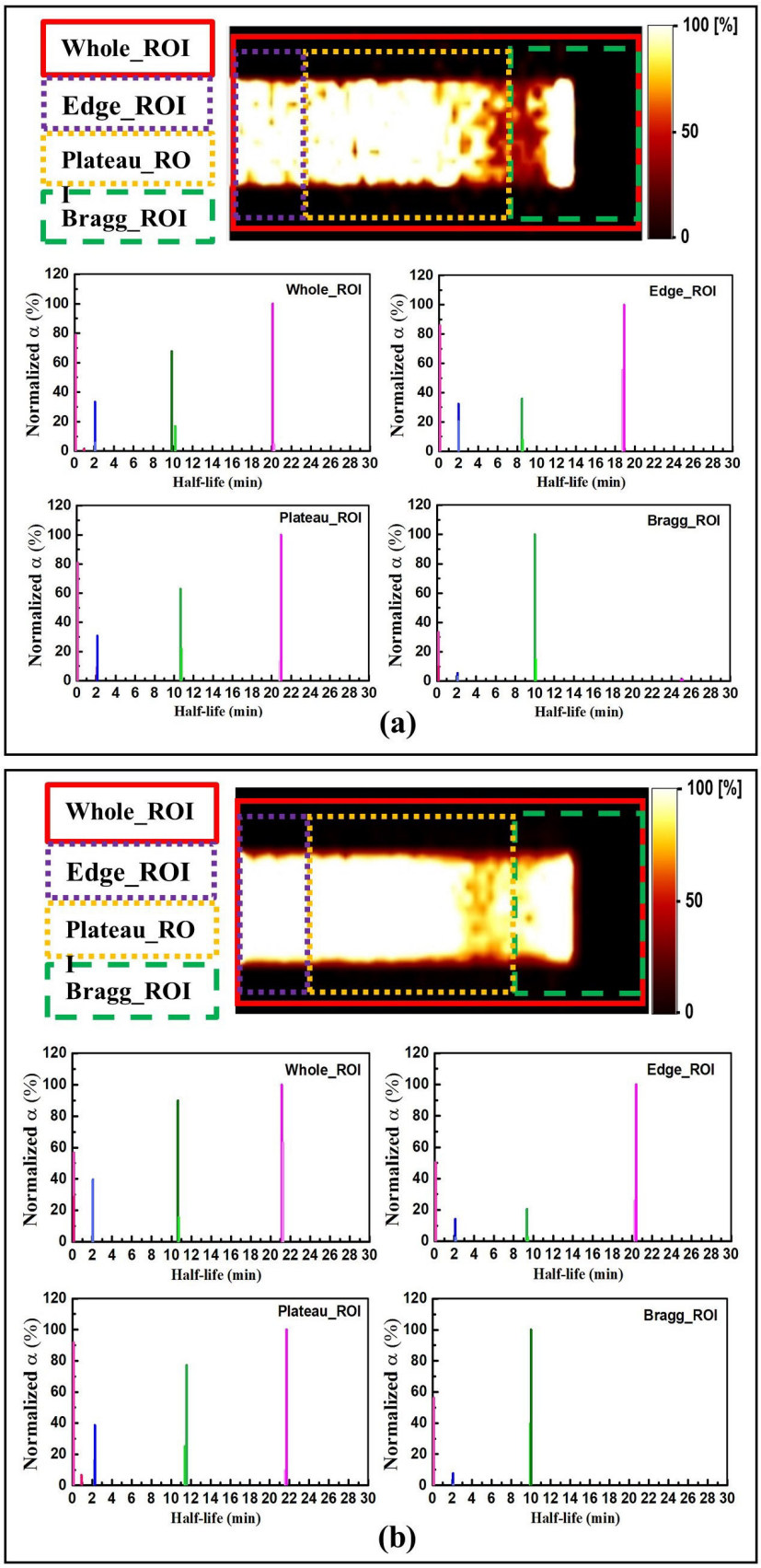

Figure 4.7: The spectral analysis (SA) results for different ROIs of the homogeneous phantom. Pink shows no radioisotope components, blue shows ^{15}O, magenta shows ^{11}C, and green shows ^{13}N radioisotopes, respectively; (**a**) for pristine and (**b**) for SOBP.

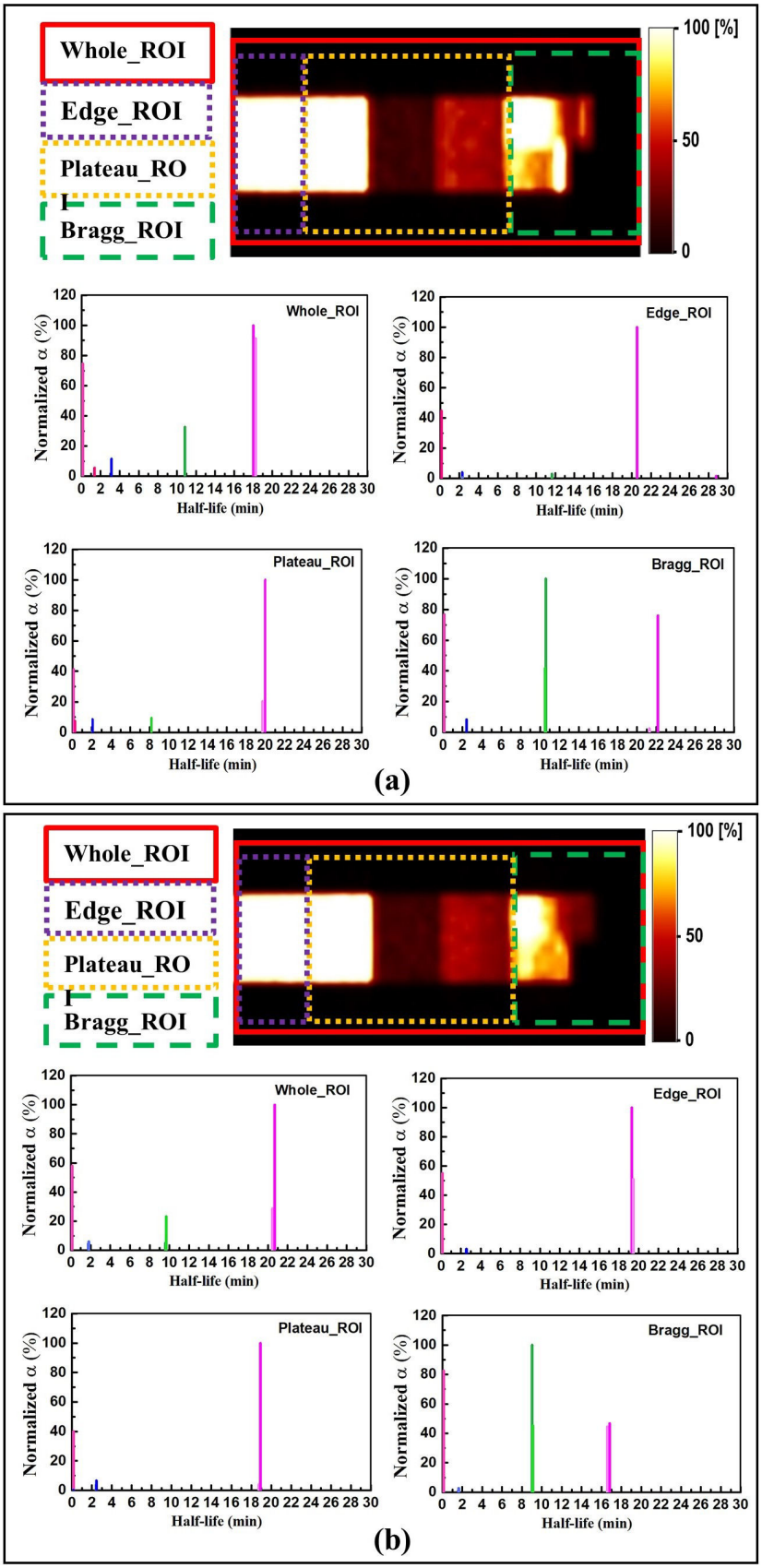

Figure 4.8: The spectral analysis (SA) results for different ROIs of the inhomogeneous phantom. Pink shows no radioisotope components, blue shows ^{15}O, magenta shows ^{11}C, and green shows ^{13}N radioisotopes, respectively; (**a**) for pristine and (**b**) for SOBP.

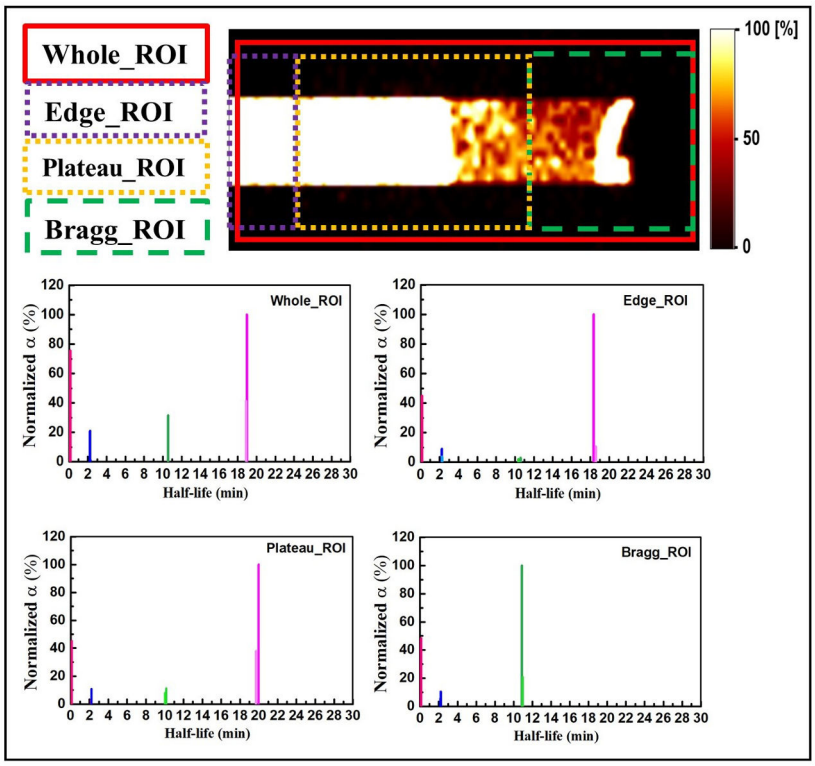

Figure 4.9: The spectral analysis (SA) results for different ROIs of the MIRD anthropomorphic phantom irradiated with 80 MeV monoenergetic beam.

From the Figure 4.9, it is observed for the MIRD anthropomorphic phantom study, at the whole, edge and as well as plateau regions, contributions from long-lived radioisotope which half-life almost equal to ^{11}C were dominated. And there is a very few contributions from the relatively short-lived radioisotopes ^{13}N and ^{15}O in these regions. It is expected as the SA technique was applied to the data set of after 15 minutes off irradiation (from 15 to 55 minutes) considering the offline PET verification the shorter half-life ^{15}O radioisotopes almost vanished out. The Bragg peak ROI, however, shows the greatest contribution from the radioisotope ^{13}N, whereas the contribution from the radioisotope ^{15}O is less. The SA approach was applied for quantifying of different radioisotopes at any specific region. It is promising that SA can separate the ^{13}N peak at the distal falloff region among from other radioisotopes ^{11}C and ^{15}O; this method would be useful for analyzing the experimentally obtained data.

4.3.2 Experimental studies

Figures 4.10 shows the 2D and 3D images with their associated 1D profiles of the SA extracted radioisotopes SA_^{15}O, SA_^{11}C, and SA_^{13}N for PEMGRAPH measurement. In Figure 4.10, the y-axis represents the normalized intensity for each radioisotope and x-axis represents the depth. From Figure 4.10, it is observed that the ^{11}C (shown as SA_^{11}C) has two peaks namely; (1) at the entrance and (2) at a higher depth. On the other hand, the ^{15}O (shown as SA_^{15}O) has a peak at a higher depth, and it appeared after the second peak of ^{11}C. The ^{13}N (shown as SA_^{13}N) peak was found to appear after the ^{15}O peak. In addition, the 1D profiles are the summation of 2D images along the y-axis (i.e., lateral position); therefore, the shape of 1D profiles would be smooth without showing any sharp cutoffs.

The SA technique was also applied to the time-course datasets (from 15 to 55 minutes after irradiation) to predict the half-life of each positron emitting radioisotopes present in the different regions of interest ROIs (see in Figure 4.1). Figure 4.11 represents radioisotopes half-life with their concentration that found from the experimental data. Same as simulations, for all ROIs, the x-axis represents the half-life (i.e., $log(2)/\beta$) for the extracted radioisotopes, and the y-axis represents the concentration of radioisotopes, labeled as normalized α. Considering Figure 4.11, we observe that for the whole ROI, the contribution from long-lived radioisotopes was dominant. It is observed that the highest contribution from long-lived radioisotopes is for the edge ROI, which is close to ^{11}C radioisotopes. In the plateau region, it is observed that the total contribution is the same as in the whole and edge regions (i.e., the greatest contribution is from long-lived radioisotopes). On the other hand, for the Bragg ROI, the half-life of radioisotopes was slightly larger than that of the ^{13}N radioisotopes. From the present analysis scheme, the activity in the distal fall-off region of proton-induced ^{13}N radioisotopes has been confirmed as the real half-life of ^{13}N is $\sim$ 10 minutes. The discretization in SA and measurement errors (background counts and contributions from multiple radioisotopes) would lead to some differences in the estimated half-life value for a specific radioisotope when compared to its known physical half-life.

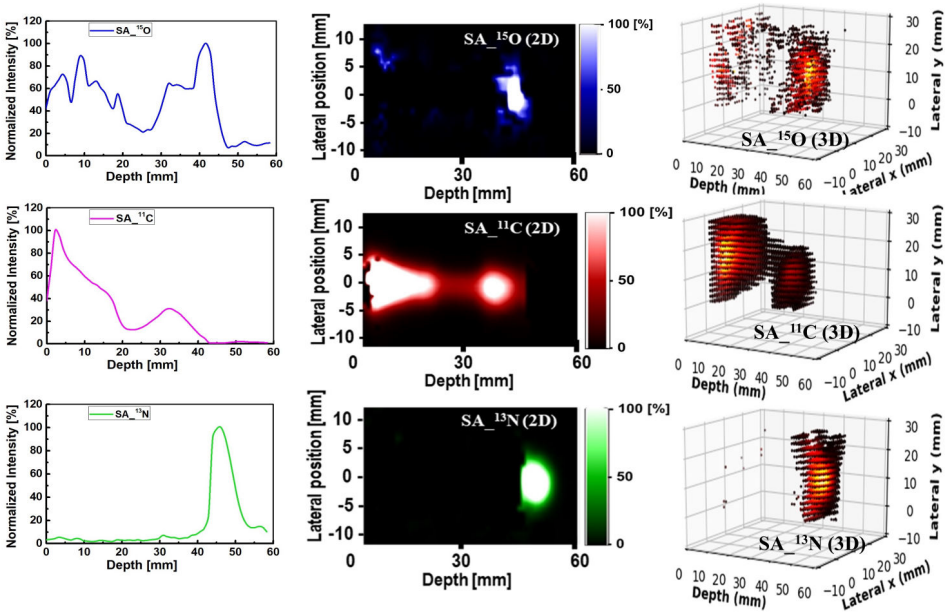

Figure 4.10: The 1D, 2D, and 3D profiles of SA extracted radioisotopes SA_^{15}O (first row), SA_^{11}C (second row), and SA_^{13}N (third row) for the PEMGRAPG measured data of the homogeneous water-gel phantom irradiated with 80 MeV proton beam.

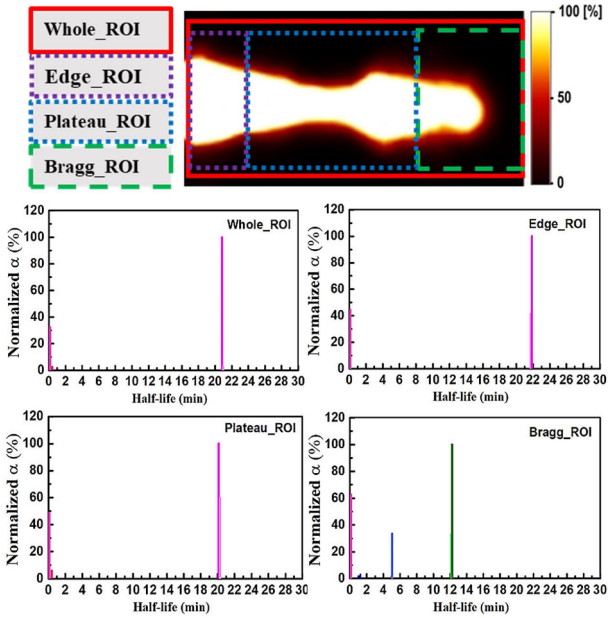

Figure 4.11: The spectral analysis (SA) results for different ROIs of the PEMGRAPH measured data. Pink shows no radioisotope components, blue shows ^{15}O, magenta shows ^{11}C, and green shows ^{13}N radioisotopes, respectively.

4.4 Conclusions

In this chapter the obtained results of an analysis are presented that were performed to the simulated and experimental results of the previous Chapter-2 and 3, respectively. An investigation was conducted to quantify proton induced radioisotopes via the simplest and fastest Spectral Analysis (SA) approach following a step-by-step analysis scheme to verify proton therapy. For this purpose, a decomposition SA approach was applied to MC simulation results from the homogeneous, inhomogenous slab and MIRD anthropomorphic targets as well as experimental results. In both simulation and experimental studies, the proposed scheme successfully extracted the 3D spatial distributions of positron emitting radioisotopes, namely ^{15}O, ^{11}C, and ^{13}N. The half-life of the SA extracted radioisotopes were confirmed by the ROIs analysis. In case of experimental data, the SA analysis confirmed the activity in the distal falloff region of proton induced ^{13}N radioisotopes. The ROIs study also confirmed that the ^{13}N radioisotope makes the highest contribution in the Bragg region.The results obtained from the present scheme showed the formation of a ^{13}N peak near the Bragg peak, which was found to be in a good agreement with the simulations studies. By utilizing the present scheme and developed tools, positron emitting radioisotopes could be extracted and visualized in 3D, which would lead to estimating the proton range and verifying it.

Chapter 5

Quantitative comparison and proton range verification

5.1 Quantitative comparison

5.1.1 Comparison between simulated and SA results

A quantitative comparison was carried out in this chapter between SA extracted and MC simulated radioisotopes. The simulated positron emitting radioisotopes were obtained using the PHITS MC code in the homogeneous, inhomogeneous slab and MIRD anthropomorphic phantoms in terms of pristine and SOBP fields. The SA was applied following the step-by-step scheme explained in the Chapter-4. The peak positions of the proton induced positron emitting radioisotopes were verified by comparing the SA extracted radioisotope with the MC simulated radioisotope as well as with simulated dose for both the simulation and experimental studies.

Figure 5.1 (a) and (b) show show a comparison of the 1D profiles between the simulated and the SA extracted radioisotopes in case of homogeneous phantom studies with pristine and SOBP distributions. The MC simulated isotopes termed as MC_^{15}O, MC_^{11}C, and MC_^{13}N whereas the SA extracted radioisotopes termed as SA_^{15}O, SA_^{11}C, and SA_^{13}N for both of pristine and SOBP, respectively. It is observed that there is a good agreement between the simulated radioisotopes and SA extracted one and also show no offset distance at the distal depth region for both pristine and SOBP distributions of homogeneous phantom studies. Though, some discrepancies observed between SA extracted ^{13}N radioisotope with MC simulated one before starting the peak in the SOBP distributions, where as a good agreement between them in case of pristine distribution. Comparing the offset distance between the Bragg peak and the MC simulated and SA extracted ^{13}N peak, an offset distance of $\sim$ 2 mm was obtained for both peaks shown in Figure 5.1 (a) that we reported [Islam et al., 2022a]. For the SOBP proton beam results shown in Figure

5.1 (b), the ^{13}N peak is within the same $\sim$ 1 to $\sim$ 2 mm shows good agreement with pristine.

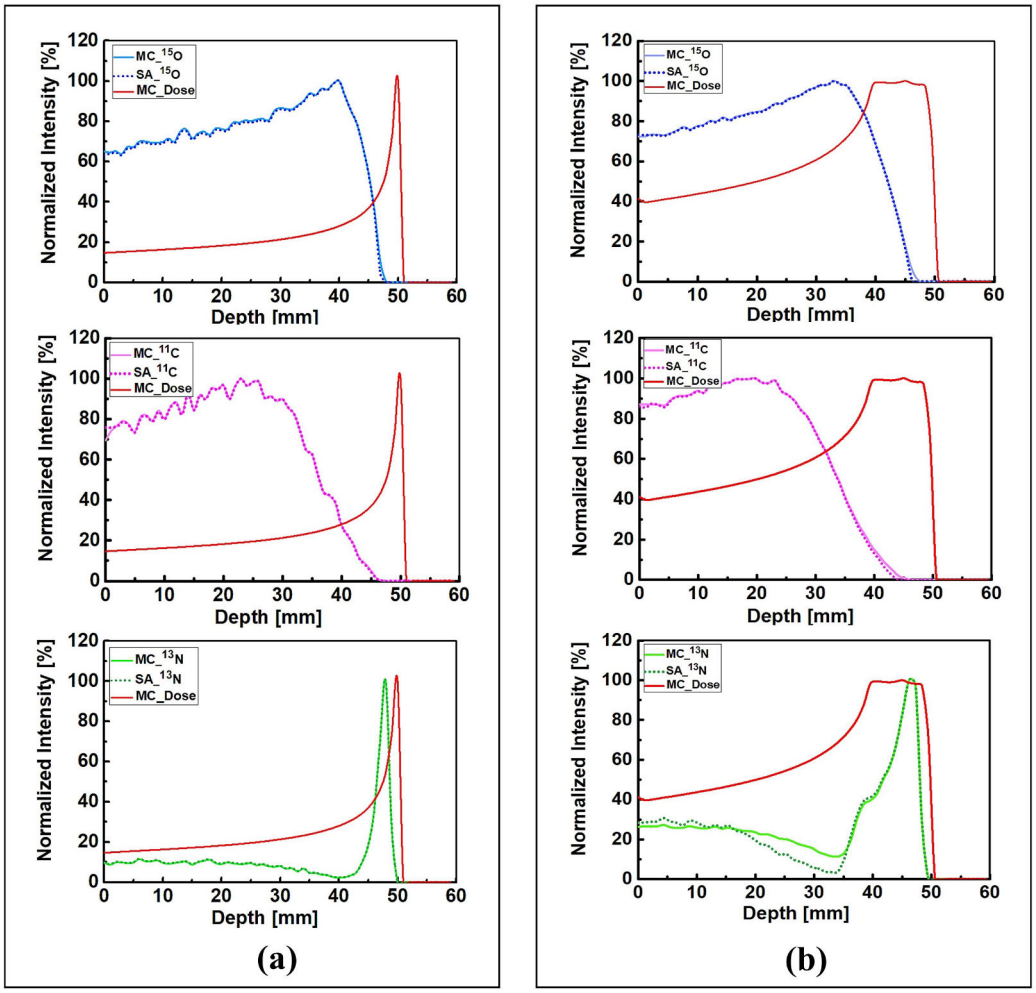

Figure 5.1: Comparisons of the 1D profiles between the MC simulated (solid line) and SA extracted (dotted line) (^{15}O, ^{11}C, and ^{13}N) radioisotopes and dose (solid red) of homogeneous phantom; (**a**) for pristine and (**b**) for SOBP distributions.

Figure 5.2 (a) and (b) show a comparison of the 1D profiles between simulated and SA extracted radioisotopes in case of inhomogeneous slab phantom studies. The MC simulated isotopes termed as MC_^{15}O, MC_^{11}C, and MC_^{13}N whereas the SA extracted radioisotopes termed as SA_^{15}O, SA_^{11}C, and SA_^{13}N in the cases of pristine and SOBP, respectively. From the Figure 5.2 (a) and (b), it is observed that there is no offset distance at the distal depth region between the SA extracted and the MC simulated radioisotopes in the beam direction. Though, some discrepancies observed between SA radioisotopes and MC simulated one in the shallow-depth region for the ^{11}C, ^{15}O, and ^{13}N radioisotope. One possible reason for the observed fluctuations in the profiles could be the higher energy of the incident proton beam

at shallow depth. Comparing the offset distance between the Bragg peak and the MC simulated and SA extracted ^{13}N peak for pristine and SOBP distributions, an offset distance of ~ 1 and ~ 2 mm were obtained for the both peaks shown in Figure 5.2 (a) and (b). The obtained offset values is in a good agreement with our previous work on irradiation of homogeneous phantoms that we have previously reported [Islam et al., 2022a].

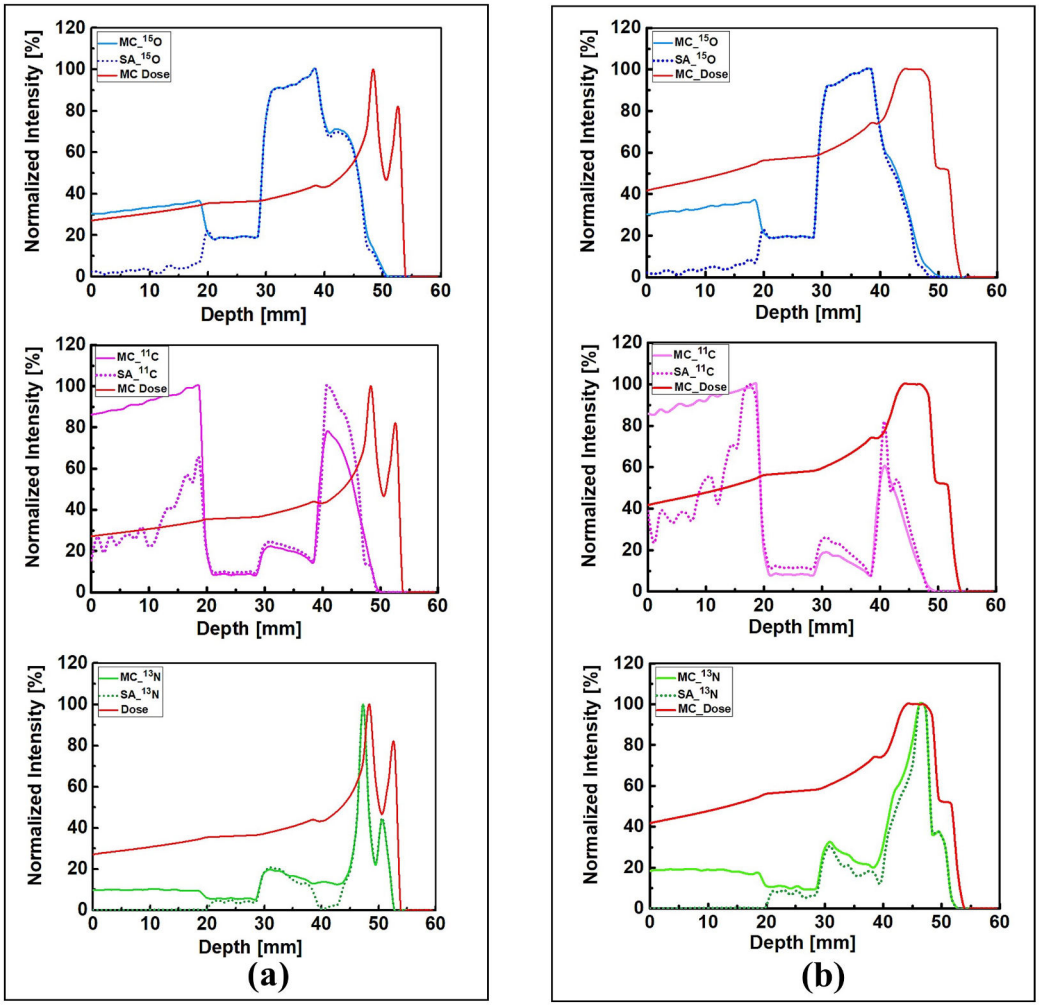

Figure 5.2: Comparisons of the 1D profiles profiles between the MC simulated (solid line) and SA extracted (dotted line) (^{15}O, ^{11}C, and ^{13}N) radioisotopes and dose (solid red) of inhomogeneous slab phantom; (**a**) for pristine and (**b**) for SOBP distributions.

Figure 5.3 shows a comparison of the 1D profiles between simulated and SA extracted radioisotopes in case of MIRD anthropomorphic phantom studies. Same as before the SA extracted radioisotopes termed as termed as SA_^{15}O, SA_^{11}C, and SA_^{13}N where as the MC simulated isotopes termed as MC_^{15}O, MC_^{11}C, and MC_^{13}N, respectively. From the Figure 5.3, it is showed that the estimated results from MC and SA methods are in good agreement, particularly for the ^{13}N positron

emitting radioisotope that would be used for proton range monitoring and verification. Some degree of discrepancies between the activity of positron emitting radioisotopes obtained from MC and SA methods can be observed at lower depths; this is mainly due to very close contribution from positron emitting radionuclides (^{15}O, ^{11}C, and ^{13}N) at the entrance region where incident proton beam initially interacts. The SA method experiences difficulties in accurately separating these at the entrance region, however the estimations from the SA approach improve at higher depths. From the results shown in Figure 5.3, it can be concluded that the predicted ^{13}N radioisotope peak using SA method is close to the peak determined by MC method, which in turn would be close to the actual Bragg peak $\sim$ 1 mm, where the Bragg peak and the generated ^{13}N peak are located at 66 and 65 mm, respectively. Therefore, the SA method found to be feasible to predict activity distribution of positron emitting radioisotopes when applied to the MIRD anthropomorphic phantoms. This obtained offset value is also in good agreement with our previously reported data [Islam et al., 2022a].

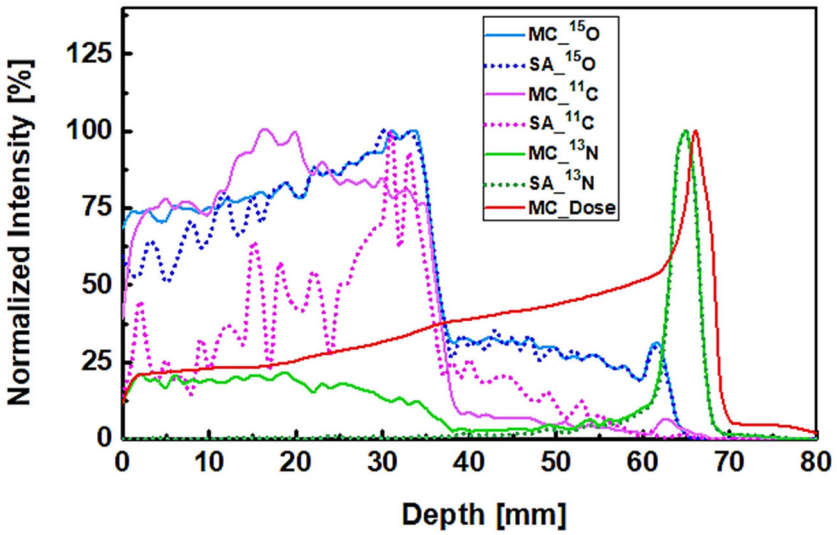

Figure 5.3: The comparison of 1D profiles between the MC simulated (solid line) and SA extracted (dotted line) (^{15}O, ^{11}C, and ^{13}N) radioisotopes and dose (solid red) of MIRD anthropomorphic phantom.

5.1.2 Comparison between experimental and SA results

The spectral analysis (SA) approach following the step-by-step scheme was applied to the experimental dynamic time-dependent activity data to quantify different positron emitting radioisotopes. Figure 5.4 shows the 1D profiles generated using the SA approach and MC simulated dose, where the the y-axis represents

the normalized intensity. Same as simulation studies the SA extracted radioisotopes termed as SA_^{15}O, SA_^{11}C, and SA_^{13}N. From the Figure 5.4, it is shown that the SA extracted SA_^{13}N peak very close to the actual Bragg peak of the MC simulated dose deposition. From the 1D profiles shown in Figure 5.4 termed as SA_^{15}O, SA_^{11}C, and SA_^{13}N peaks were found to be at 33, 39 and 46 mm depths, respectively. Furthermore, the peak of the MC simulated dose was found to be at 49 mm depth. On the other hand, comparing with the PEMGRAPH data the extracted radioisotopes produced peak at the end. Therefore, the offset between the MC simulated dose and the extracted SA_^{13}N peak was found to be 3 mm, that we reported [Islam et al., 2022b] and this value also showed a good agreements with the previous investigation [Islam et al., 2022a]. As we can see the simulated Bragg peak for 80 MeV of incident protons beam is very sharp, while the experimental SA_^{13}N peak is rather wide, indicating reasonable agreement with the simulation results.

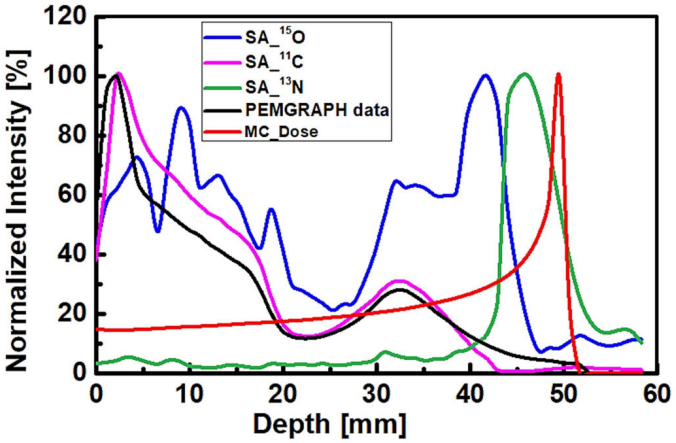

Figure 5.4: Comparison of the 1D profiles between the MC simulated dose (solid red), PEMGRAPH data (solid black) and SA extracted (SA_^{11}C, SA_^{15}O and SA_^{13}N) radioisotopes of PEMGRAPH measurement.

Figure 5.5 shows the 2D images of the extracted radioisotopes termed as termed SA_^{15}O, SA_^{11}C, and SA_^{13}N. From the Figure 5.5, it is shown that SA_^{11}C has two peaks—namely, (1) at the entrance and (2) at a higher depth. On the other hand, the SA_^{15}O has a peak at a higher depth, and it appeared after the second peak of SA_^{11}C. The SA_^{13}N peak was found to appear after the SA_^{15}O peak. In addition, the 1D profiles are the summation of 2D images (Figure 5.4) along the y-axis (i.e., lateral position); therefore, the shape of 1D profiles would be smooth without showing any sharp cutoffs.

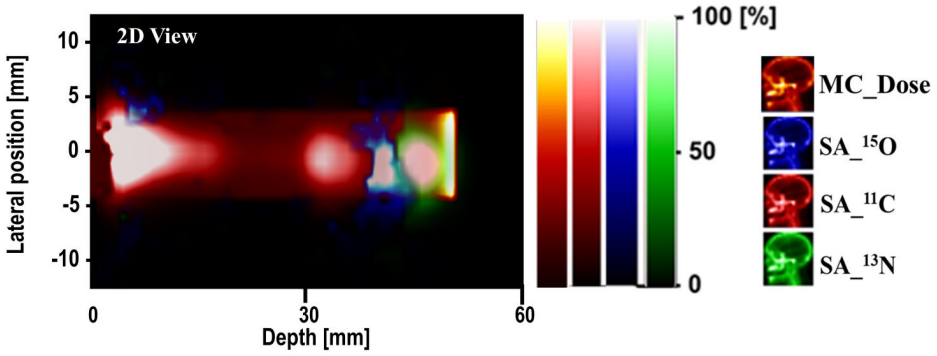

Figure 5.5: A 2D comparison the SA extracted (SA_^{11}C, SA_^{15}O and SA_^{13}N) radioisotopes.

5.2 Conclusions

In this chapter, radioisotopes that were extracted using SA and those that were simulated using MC were compared quantitatively. The peak positions of the proton induced positron emitting radioisotopes were verified by comparing the SA extracted radioisotope with the MC simulated radioisotope as well as with simulated dose for both the simulation and experimental studies. The results show there is no offset distance at the distal depth region between the SA extracted and the MC simulated radioisotopes along the beam direction. In other words, for example, the peak positions of the SA extracted ^{13}N is completely overlaid on the simulated one. Though, some discrepancies observed between SA radioisotopes and MC simulated one in the shallow-depth region. It is observed that the offset distances between the SA extracted 13N peak and the actual Bragg peak with 1 to 2 mm, but the ^{11}C and ^{15}O peaks are very far away from the real Bragg peaks for the homogeneous, inhomogeneous slab and MIRD anthropomorphic phantom studies which is a good agreement with MC radioisotopes. On the other hand, when compared to the actual Bragg peak for the simulated homogeneous water-gel, the offset distance between the SA extracted ^{13}N peak from the experimental data is 3 mm. The simulated Bragg peak is very sharp, while the experimental ^{13}N peak is rather wide, indicating reasonable agreement with the simulation results. This distinct ^{13}N followed by the lower threshold of ^{16}O(p,2p2n)^{13}N and ^{14}N(p,pn)^{13}N nuclear reaction channels as well as the offset values could be used as an index for non-invasive PEM-based proton range verification using SA approach

Chapter 6

Conclusions and future prospects

Conclusions and future prospects

In this chapter, we summarize the main conclusions of our research concerning. This PhD project is focused on the development of proton range verification framework for proton therapy with highly sensitive positron emission mammography system. For this purpose, we investigated the distal falloff production and extraction of ^{13}N positron emitters using the simplest and fastest SA approach in simulations and experiments with highly sensitive PEM system. We have successfully developed a series of simulation, experimental, and analysis tools for this purpose and applied them in this experimental campaign for the first time. In the simulation studies the productions of positron emitting radioisotopes namely ^{11}C, ^{15}O and ^{13}N were evaluated using the PHITS code. Three different phantom types were used in the simulation studies, including homogeneous, inhomogeneous slab, and MIRD anthropomorphic phantom. We irradiated homogeneous and inhomogeneous slab phantoms using two distinct incident proton beams, namely (1) pristine and (2) SOBP. On the other hand, the MIRD anthropomorphic phantom was irradiated to an 80 MeV monoenergetic proton beam. The simulation results showed the offset distances between the generated ^{13}N peak and the actual Bragg peak with 1 to 2 mm, whereas the ^{11}C and ^{15}O peaks are very far away from the real Bragg peaks for the homogeneous, inhomogeneous slab and MIRD anthropomorphic phantom studies, respectively. The experimental irradiation was performed using an azimuthally varying field (AVF) cyclotron with a 80 MeV monoenergetic pencil like beam.

The activity of positron emitting radioisotopes obtained from MC and SA methods for the homogeneous, inhomogeneous slab and MIRD anthropomorphic phantom, found to be in good agreement. Though, some discrepancies observed between SA radioisotopes and MC simulated one in the shallow-depth region for the radioisotope. The obtained 3D visualization would provide information about dispersion of ^{13}N positron emitting radionuclides in 3D cartesian space. The results showed the proposed tool with the combination of highly sensitive PEM system

and SA approach could be useful for proton range verification. From our simulation and experimental studies, we conclude that the SA approach is feasible within clinical beam delivery conditions. We therefore recommend further development towards clinical trials.

The possible improvements that have been identified for future experiments are:

- To facilitate in-beam clinical trials, further improvements of the PEM system (PEMGRAPH) are recommended, which will require a larger-scale positron annihilation photon detection system and a more efficient workflow for patient-specific modeling of positrons.

Bibliography

Abdel-Wahab, May et al. (2021), Global radiotherapy: current status and future directions—white paper. *JCO Global Oncology*. 7: p. 827–842.

Agostinelli, Sea et al. (2003), GEANT4—a simulation toolkit. *Nuclear instruments and methods in physics research section A: Accelerators, Spectrometers, Detectors and Associated Equipment*. 506(3): p. 250–303.

Amaldi, Ugo and Gerhard Kraft (2006), Particle accelerators take up the fight against cancer. *Cern Courier*. 46(10): p. 17–20.

Anderson, Herbert L (2014), MA NIA.

Beebe-Wang, JJ et al. (2002), Feasibility of positron emission tomography of dose distribution in proton beam cancer therapy. Tech. rep. Brookhaven National Lab.(BNL), Upton, NY (United States).

Beni, Mehrdad Shahmohammadi et al. (2022), Development of PHITS graphical user interface for simulation of positron emitting radioisotopes production in common biological materials during proton therapy. *Journal of Radiation Research*: p. 1–8.

Berger, MJ et al. (2017), Stopping-power and range tables for electrons, protons, and helium ions, NIST standard reference database 124. *National Institute of Standards and Technology*.

Bichsel, Hans (2013), Stochastics of energy loss and biological effects of heavy ions in radiation therapy. In: *Advances in Quantum Chemistry*. Vol. 65. Elsevier, p. 1–38.

Bortfeld, Thomas (1997), An analytical approximation of the Bragg curve for therapeutic proton beams. *Medical physics*. 24(12): p. 2024–2033.

Carson, Richard E, Sung-Cheng Huang, and Michael E Phelps (1981), BLD: a software system for physiological data handling and model analysis. In: *Proceedings of the Annual Symposium on Computer Application in Medical Care*. American Medical Informatics Association, p. 562.

Carter, Leland Lavele and Edmond Darrell Cashwell (1975), Particle-transport simulation with the Monte Carlo method. Tech. rep. Los Alamos Scientific Lab., N. Mex.(USA).

Carter, LL et al. (1974), Monte Carlo code development in Los Alamos. Tech. rep.

Charmsaz, Sara et al. (2019), Novel strategies for cancer treatment: highlights from the 55th IACR annual conference. *Cancers*. 11(8): p. 1125.

Cho, Jongmin et al. (2017), Feasibility study of using fall-off gradients of early and late PET scans for proton range verification. *Medical physics*. 44(5): p. 1734–1746.

Cunningham, Vincent J and Terry Jones (1993), Spectral analysis of dynamic PET studies. *Journal of Cerebral Blood Flow & Metabolism*. 13(1): p. 15–23.

Das, Indra J, Harald Paganetti, American Association of Physicists in Medicine, et al. (2015), Principles and practice of proton beam therapy. Medical Physics Publishing.

Del Guerra, A and G Di Domenico (1994), Positron emission tomography as an aid to in 'vivo'dosimetry for proton radiotherapy: a Monte Carlo simulation. *Nucl Instrum Meth A*. 345: p. 379–84.

Dorai, Thambi and Bharat B Aggarwal (2004), Role of chemopreventive agents in cancer therapy. *Cancer letters*. 215(2): p. 129–140.

Ferlay, J, I Soerjomataram, M Ervik, et al. (2013), Cancer incidence and mortality worldwide, international agency for research on cancer. *Cancer incidence and mortality worldwide, International agency for research on cancer*: p. 120–63.

Ferrari, Alfredo et al. (2005), FLUKA: a multi-particle transport code (Program version 2005). CERN-2005-10. Cern.

Fiorina, E et al. (2018), Monte Carlo simulation tool for online treatment monitoring in hadrontherapy with in-beam PET: a patient study. *Physica medica*. 51: p. 71–80.

Friedberg, Errol C (2003), DNA damage and repair. *Nature*. 421(6921): p. 436–440.

Gensheimer, Michael F et al. (2010), In vivo proton beam range verification using spine MRI changes. *International Journal of Radiation Oncology* Biology* Physics*. 78(1): p. 268–275.

Goitein, Michael (2007), Radiation oncology: a physicist's-eye view. Springer Science & Business Media.

Goldstone, KE (1990), Tissue substitutes in radiation dosimetry and measurement, in: ICRU report 44, international commission on radiation units and measurements, USA (1989).

Gottschalk, B (2004), Passive beam spreading in proton radiation therapy. *unpublished book*.

Grogg, Kira et al. (2015), Mapping O-15 production rate for proton therapy verification. *International Journal of Radiation Oncology* Biology* Physics*. 92(2): p. 453–459.

Guo, Shiyao et al. (2021), Kernel graph filtering—a new method for dynamic sinogram denoising. *PloS one*. 16(12): e0260374.

Hayakawa, Yoshinori et al. (1995), Acoustic pulse generated in a patient during treatment by pulsed proton radiation beam. *Radiation Oncology Investigations*. 3(1): p. 42–45.

Hensley, Frank W (2017), Present state and issues in IORT physics. *Radiation Oncology*. 12(1): p. 1–30.

Islam, M Rafiqul et al. (2022a), Proton range monitoring using N-13 peak for proton therapy applications. *PloS one*. 17(2): e0263521.

Islam, Md Rafiqul, Hiroshi Watabe, Andreoli Stefano, et al. (2020), Measurement and comparison of output factors using two detectors for NOVAC7 intra-operative radiotherapy accelerator. *International Journal of Medical Physics, Clinical Engineering and Radiation Oncology*. 9(02): p. 52.

Islam, Md Rafiqul et al. (2022b), An analysis scheme for 3D visualization of positron emitting radioisotopes using positron emission mammography system. *Applied Sciences*. 12(2): p. 823.

Iwase, Hiroshi, Koji Niita, and Takashi Nakamura (2002), Development of general-purpose particle and heavy ion transport Monte Carlo code. *Journal of Nuclear Science and Technology*. 39(11): p. 1142–1151.

Kai, Tetsuya et al. (2001), DCHAIN-SP 2001: high energy particle induced radioactivity calculation code. Tech. rep. Japan Atomic Energy Research Inst.

Kitwanga, Sindano Wa et al. (1989), Production of N-13 radioactive nuclei from (p 13, n) or O-16 (p, α) reactions. *Physical Review C*. 40(1): p. 35.

Knopf, Antje-Christin and Antony Lomax (2013), In vivo proton range verification: a review. *Physics in Medicine & Biology*. 58(15): R131.

Kraan, AC et al. (2014), Proton range monitoring with in-beam PET: Monte Carlo activity predictions and comparison with cyclotron data. *Physica Medica*. 30(5): p. 559–569.

Kraft, G, M Krämer, and M Scholz (1992), LET, track structure and models. *Radiation and environmental biophysics*. 31(3): p. 161–180.

Langner, Jens (2003), Development of a parallel computing optimized head movement correction method in positron emission tomography. *Master of computer science thesis, university of Applied sciences Dresden and research center Dresden-rossendorf*.

Litzenberg, Dale William (1997), On-line monitoring and PET imaging of the positron-emitting activity created in tissue by proton radiotherapy beams. University of Michigan.

Lu, Hsiao-Ming, Greg Mann, and Ethan Cascio (2010), Investigation of an implantable dosimeter for single-point water equivalent path length verification in proton therapy. *Medical physics*. 37(11): p. 5858–5866.

Malmer, Cynthia J (2001), ICRU report 63, nuclear data for neutron and proton radiotherapy and for radiation protection. *Medical physics*. 28(5): p. 861.

Min, Chul-Hee et al. (2006), Prompt gamma measurements for locating the dose falloff region in the proton therapy. *Applied physics letters*. 89(18): p. 183517.

Miyake, Kanae K et al. (2014), Performance evaluation of a new dedicated breast PET scanner using NEMA NU4-2008 standards. *Journal of Nuclear Medicine*. 55(7): p. 1198–1203.

Mukhopadhyay, D, A Del Guerra, and O Di Domenico (1995), For PET-monitored hadrontherapy. *TERA 95/19 TRA15*.

Mumot, M et al. (2010), Proton range verification using a range probe: definition of concept and initial analysis. *Physics in Medicine & Biology*. 55(16): p. 4771.

Murthy, Kavita et al. (2000), Results of preliminary clinical trials of the positron emission mammography system PEM-I: a dedicated breast imaging system producing glucose metabolic images using FDG. *Journal of Nuclear Medicine*. 41(11): p. 1851–1858.

Newhauser, Wayne D and Rui Zhang (2015), The physics of proton therapy. *Physics in Medicine & Biology*. 60(8): R155.

Niita, Koji et al. (2001), High-energy particle transport code NMTC/JAM. *Nuclear Instruments and Methods in Physics Research Section B: Beam Interactions with Materials and Atoms*. 184(3): p. 406–420.

Nishio, Teiji et al. (2010), The development and clinical use of a beam ON-LINE PET system mounted on a rotating gantry port in proton therapy. *International Journal of Radiation Oncology* Biology* Physics*. 76(1): p. 277–286.

Ohnishi, Seiki (2021), Gxsview: geometry and cross section viewer for calculating radiation transport. *SoftwareX*. 14: p. 100681.

Paganetti, Harald (2012), Range uncertainties in proton therapy and the role of Monte Carlo simulations. *Physics in Medicine & Biology*. 57(11): R99.

Paganetti, Harald et al. (2002), Relative biological effectiveness (RBE) values for proton beam therapy. *International Journal of Radiation Oncology* Biology* Physics*. 53(2): p. 407–421.

Parodi, K, Wolfgang Enghardt, and T Haberer (2001), In-beam PET measurements of β+ radioactivity induced by proton beams. *Physics in Medicine & Biology*. 47(1): p. 21.

Parodi, Katia and Thomas Bortfeld (2006), A filtering approach based on gaussian–powerlaw convolutions for local PET verification of proton radiotherapy. *Physics in Medicine & Biology*. 51(8): p. 1991.

Parodi, Katia et al. (2007), PET/CT imaging for treatment verification after proton therapy: a study with plastic phantoms and metallic implants. *Medical physics*. 34(2): p. 419–435.

Phelps, Michael E et al. (1975), Application of annihilation coincidence detection to transaxial reconstruction tomography. *Journal of nuclear medicine*. 16(3): p. 210–224.

Poludniowski, Gavin, NM Allinson, and PM Evans (2015), Proton radiography and tomography with application to proton therapy. *The British journal of radiology*. 88(1053): p. 20150134.

Remmele, Steffen et al. (2011), A deconvolution approach for PET-based dose reconstruction in proton radiotherapy. *Physics in Medicine & Biology*. 56(23): p. 7601.

Rohling, Heide (2015), Simulation studies for the in-vivo dose verification of particle therapy. Tech. rep. Helmholtz-Zentrum Dresden-Rossendorf eV.

Sato, Tatsuhiko et al. (2018), Features of particle and heavy ion transport code system (PHITS) version 3.02. *Journal of Nuclear Science and Technology*. 55(6): p. 684–690.

Sato, Tatsuhiko et al. (2021), Individual dosimetry system for targeted alpha therapy based on PHITS coupled with microdosimetric kinetic model. *EJNMMI physics*. 8(1): p. 1–16.

Shao, Yiping et al. (2014), In-beam PET imaging for on-line adaptive proton therapy: an initial phantom study. *Physics in Medicine & Biology*. 59(13): p. 3373.

Shepp, Lawrence A and Yehuda Vardi (1982), Maximum likelihood reconstruction for emission tomography. *IEEE transactions on medical imaging*. 1(2): p. 113–122.

Sihver, Lembit et al. (1993), Total reaction and partial cross section calculations in proton-nucleus (Z t$\leq$ 26) and nucleus-nucleus reactions (Z p and Z t$\leq$ 26). *Physical Review C*. 47(3): p. 1225.

Sportelli, Giancarlo et al. (2013), First full-beam PET acquisitions in proton therapy with a modular dual-head dedicated system. *Physics in Medicine & Biology*. 59(1): p. 43.

Sung, Hyuna et al. (2021), Global cancer statistics 2020: GLOBOCAN estimates of incidence and mortality worldwide for 36 cancers in 185 countries. *CA: a cancer journal for clinicians*. 71(3): p. 209–249.

Tashima, Hideaki et al. (2012), A single-ring OpenPET enabling PET imaging during radiotherapy. *Physics in Medicine & Biology*. 57(14): p. 4705.

Thompson, CJ et al. (1994), Feasibility study for positron emission mammography. *Medical physics*. 21(4): p. 529–538.

Thompson, CJ et al. (1995), Positron emission mammography (PEM): a promising technique for detecting breast cancer. *IEEE transactions on nuclear science*. 42(4): p. 1012–1017.

Tobias, CA et al. (1958), Pituitary irradiation with high-energy proton beams a preliminary report. *Cancer research*. 18(2): p. 121–134.

Tommasino, Francesco and Marco Durante (2015), Proton radiobiology. *Cancers*. 7(1): p. 353–381.

Turkheimer, F et al. (1994), The use of spectral analysis to determine regional cerebral glucose utilization with positron emission tomography and [18F] fluorodeoxyglucose: theory, implementation, and optimization procedures. *Journal of Cerebral Blood Flow & Metabolism*. 14(3): p. 406–422.

Vandenberghe, Stefaan, Pawel Moskal, and Joel S Karp (2020), State of the art in total body PET. *EJNMMI physics*. 7(1): p. 1–33.

Vecchio, Sara et al. (2009), A PET prototype for "in-beam" monitoring of proton therapy. *IEEE Transactions on Nuclear Science*. 56(1): p. 51–56.

Wang, G-C et al. (2006), Characterization of the LBNL PEM camera. *IEEE transactions on nuclear science*. 53(3): p. 1129–1135.

Weinberg, IN et al. (2002), PEM-2400-a biopsy-ready PEM scanner with real-time X-ray correlation capability. In: *2002 IEEE Nuclear Science Symposium Conference Record*. Vol. 2. IEEE, p. 1128–1130.

Wilson, Robert R (1946), Radiological use of fast protons. *Radiology*. 47(5): p. 487–491.

Yamaguchi, Mitsutaka et al. (2016), Secondary-electron-bremsstrahlung imaging for proton therapy. *Nuclear Instruments and Methods in Physics Research Section A: Accelerators, Spectrometers, Detectors and Associated Equipment*. 833: p. 199–207.

Yamaya, Taiga et al. (2008), A proposal of an open PET geometry. *Physics in Medicine & Biology*. 53(3): p. 757.

Yanagida, Takayuki et al. (2010), Development of Pr: LuAG scintillator array and assembly for positron emission mammography. *IEEE Transactions on Nuclear Science*. 57(3): p. 1492–1495.

Yanai, Ai et al. (2018), Newly-developed positron emission mammography (PEM) device for the detection of small breast cancer. *The Tohoku journal of experimental medicine*. 245(1): p. 13–19.

Yoshikawa, Akira et al. (2010), Positron emission mammography using Pr: LuAG scintillator–fusion of optical material study and systems engineering. *Optical Materials*. 32(10): p. 1294–1297.

Zhu, Xuping and Georges El Fakhri (2013), Proton therapy verification with PET imaging. *Theranostics*. 3(10): p. 731.

Ziegler, James F and Jochen P Biersack (1985), The stopping and range of ions in matter. In: *Treatise on heavy-ion science*. Springer, p. 93–129.

Appendix A

Input codes

A.1 Homogeneous phantom

[T i t l e]

Homogeneous phantom simulation.

[P a r a m e t e r s]

icntl = 0

maxcas = 1000

maxbch = 10

ih2o = 69

file(6) = phits.out

emin(14) = 0.50

dmax(14) = 0.60

[S o u r c e]

totfact = 1.0

s-type = 1

proj = proton

dir = 1.00

r0 = 0.50

z0 = -25.0

z1 = -25.0

e0 = 80.0 $ energy of beam [MeV/u]

[M a t e r i a l]

mat[1] $ water-gel, Density(g cm^{-3}) = 1.01 g

1H -11.00

16O -84.35

12C -4.650

[Mat Name Color]

mat name size color

1 water-gel 1 cyan

```
[ S u r f a c e ]
10   so    500.
11   rpp   -5.0  5.0   -5.0  5.0   0.0  40.0   $ water-gel
[ C e l l ]
100   -1    10
101   1    -1.01    -11
102   0    -10    #101
[ T - D e p o s i t ]
title = Deposit in xyz mesh
mesh = xyz
x-type = 2
xmin = -3.0
xmax = 3.0
nx = 60
y-type = 2
ymin = -3.0
ymax = 3.0
ny = 60
z-type = 2
zmin = 0.0
zmax = 40.0
nz = 400
unit = 0
2D-type = 3
axis = z
file = deposit.out
material = all
output = dose
epsout = 0
gshow = 1
[ T - P r o d u c t ]
title = N13 production in xyz mesh
mesh = xyz
x-type = 2
xmin = -3.0
xmax = 3.0
nx = 60
y-type = 2
```

ymin = -3.0

ymax = 3.0

ny = 60

z-type = 2

zmin = 0.0

zmax = 40.0

nz = 400

e-type = 1

ne = 1

0.0 20.0

material = all

mother = all

unit = 1

2D-type = 3

axis = z

file = N13.out

output = nuclear

part = 13N

epsout = 0

[End]

A.2 Inhomogeneous slab phantom

[T i t l e]

Inhomogeneous slab phantom simulation.

[P a r a m e t e r s]

icntl = 0

maxcas = 1000

maxbch = 10

ih2o = 69

file(6) = phits.out

emin(14) = 0.50

dmax(14) = 0.60

[S o u r c e]

totfact = 1.0

s-type = 1

proj = proton

dir = 1.00

r0 = 0.50

z0 = -25.0

z1 = -25.0

$e0 = 80.0 energy of beam [MeV/u]

e-type = 1

ne = 10

$En wt.

70 0.050 energy of beam [MeV/u] for SOBP

71 0.055

72 0.060

73 0.065

74 0.070

75 0.090

76 0.100

77 0.120

78 0.175

79 0.400

80

[M a t e r i a l]

mat[1] $PMMA (Polymethyl methacrylate) (C5H8O2), Density(g cm^{-3}) = 1.18 g

1H -8.050

12C -59.99

16O -31.96

mat[2] $lung(inflated), Density(g cm^{-3}) = 0.26

1H -10.3

12C -10.5

14N -3.10

16O -74.9

23Na -0.20

31P -0.20

32S -0.30

35Cl -0.30

39K -0.20

mat[3] $ water 1.0 g cm^{-3}

1H -11.1

16O -88.9

mat[4] $ cortical bone slab, Density(g cm^{-3}) = 1.85

1H -3.40

12C -15.5

```
14N             -4.20
16O             -43.5
23Na            -0.10
24Mg            -0.20
31P             -10.3
32S             -0.30
40Ca            -22.5
[ Mat Name Color ]
mat     name        size        color
1       PMMA        1           cyan
2       Lung        1           pastelblue
3       Water       1           pastelgreen
4       bone        0.5         gray
[ S u r f a c e ]
10    so    100.0
11    rpp    -1.50   1.50   -1.50   1.50   0.0   2.0   $ for PMMA
12    rpp    -1.50   1.50   -1.50   1.50   2.0   3.0   $ for lung
13    rpp    -1.50   1.50   -1.50   1.50   3.0   4.0   $ for water
14    rpp     0.0   1.50   -1.50   1.50   4.0   5.5   $ for PMMA
15    rpp    -1.50   0.0   -1.50   1.50   4.0   5.5   $ for bone
[ C e l l ]
100   -1   10
101   2   -1.18   -11
102   3   -0.26   -12
103   4   -1.00   -13
104   2   -1.18   -14
105   5   -1.85   -15
106   0   -10 #101 #102 #103 #104 #105
[ T - D e p o s i t ]
title = Deposit in xyz mesh
mesh = xyz
x-type = 2
xmin = -2.5
xmax = 2.5
nx = 50
y-type = 2
ymin = -2.5
ymax = 2.5
```

```
ny = 50
z-type = 2
zmin = 0.0
zmax = 6.0
nz = 60
unit = 0
2D-type = 3
axis = z
file = deposit.out
material = all
output = dose
epsout = 0
gshow = 1
[ T - P r o d u c t ]
title = N13 production in xyz mesh
mesh = xyz
x-type = 2
xmin = -2.5
xmax = 2.5
nx = 50
y-type = 2
ymin = -2.5
ymax = 2.5
ny = 50
z-type = 2
zmin = 0.0
zmax = 6.0
nz = 60
e-type = 1
ne = 1
0.0   20.0
material = all
mother = all
unit = 1
2D-type = 3
axis = z
file = N13.out
output = nuclear
```

part = 13N

epsout = 0

[E n d]

A.3 MIRD anthropomorphic phantom

[T i t l e] MIRD anthropomorphic phantom simulation.

[P a r a m e t e r s]

icntl = 0

maxcas = 1000

maxbch = 10

ireschk = 1

file(6) = phits.out

[S o u r c e]

totfact = 1.0

s-type = 1

proj = proton

r0 = 0.5

x0 = -10.0

yo = 20.0

z0 = 29.0

z1 = 30.0

dir = 0.00

e0 = 80.0

phi = 270

[M a t e r i a l]

m1 $ TISSUE, SOFT (ICRU-44), Density(g cm^{-3}) = 1.03

1000 -10.5

6000 -25.6

7000 -2.7

8000 -60.2

11000 -0.1

15000 -0.2

16000 -0.3

17000 -0.2

19000 -0.2

m2 $ Heart tissue(healthy), Density(g cm^{-3}) = 1.05

1000 -10.4

6000 -13.9

7000 -2.9

8000 -71.8

11000 -0.1

15000 -0.2

16000 -0.2

17000 -0.2

19000 -0.3

m3 $ Blood(whole), Density(g cm^{-3}) = 1.06

1000 -10.2

6000 -11.0

7000 -3.3

8000 -74.5

11000 -0.1

15000 -0.1

16000 -0.2

17000 -0.3

19000 -0.2

26000 -0.1

m4 $ Lung(healthy, inflated), Density(g cm^{-3}) = 0.26

1000 -10.3

6000 -10.5

7000 -3.1

8000 -74.9

11000 -0.2

15000 -0.2

16000 -0.3

17000 -0.3

19000 -0.2

m5 $ Brain(whole), Density(g cm^{-3}) = 1.04

1000 -10.7

6000 -14.5

7000 -2.2

8000 -71.2

11000 -0.2

15000 -0.4

16000 -0.2

17000 -0.3

19000 -0.3

m6 $ Skin, Density(g cm^{-3}) = 1.09

1000 -10.0

6000 -20.4

7000 -4.2

8000 -64.5

11000 -0.2

15000 -0.1

16000 -0.2

17000 -0.3

19000 -0.1

m7 $ Skin, Density(g cm^{-3}) = 1.09

1000 -5.0

6000 -21.2

7000 -4.0

8000 -43.5

11000 -0.1

12000 -0.2

15000 -8.1

16000 -0.3

20000 -17.6

m8 $ Leg bone, Density(g cm^{-3}) = 1.33

1000 -7.00

6000 -34.5

7000 -2.8

8000 -36.8

11000 -0.1

12000 -0.1

15000 -5.5

16000 -0.2

17000 -0.1

20000 -12.9

m9 $ Arm bone, Density (g cm^{-3}) = 1.46

1000 -6.0

6000 -31.4

7000 -3.1

8000 -36.9

11000 -0.1

12000 -0.1

15000 -7.0

16000 -0.2

20000 -15.2

m10 $ Facial bone, Density (g cm^{-3}) = 1.68

1000 -4.6

6000 -19.9

7000 -4.1

8000 -43.5

11000 -0.1

12000 -0.2

15000 -8.6

16000 -0.3

20000 -18.7

m11 $ Ribs (1st - 9th), Density (g cm^{-3}) = 1.41

1000 -6.4

6000 -26.3

7000 -3.9

8000 -43.6

11000 -0.1

12000 -0.1

15000 -6.0

16000 -0.3

17000 -0.1

19000 -0.1

20000 -13.1

m12 $ Ribs (10st - 12th), Density (g cm^{-3}) = 1.52

1000 -5.6

6000 -23.5

7000 -4.0

8000 -43.4

11000 -0.1

12000 -0.1

15000 -7.2

16000 -0.3

17000 -0.1

19000 -0.1

20000 -15.6

m13 $ Cervical vertebrea, Density (g cm^{-3}) = 1.42

1000 -6.3

6000 -26.1

7000 -3.9

8000 -43.6

11000 -0.1

12000 -0.1

15000 -6.1

16000 -0.3

17000 -0.1

19000 -0.1

20000 -13.3

m14 $ Thoracic / Lumbal vertebrea, Density (g cm^{-3}) = 1.33

1000 -7.0

6000 -28.7

7000 -3.8

8000 -43.7

12000 -0.1

15000 -5.1

16000 -0.2

17000 -0.1

19000 -0.1

20000 -11.1

m15 $ Intervertebral disks, Density (g cm^{-3}) = 1.10

1000 -9.6

6000 -9.9

7000 -2.2

8000 -74.4

11000 -0.5

15000 -2.2

16000 -0.9

17000 -0.3

m16 $ AIR, DRY (NEAR SEA LEVEL), Density (g cm^{-3}) = 1.20479E-03

6000 -0.000124

7000 -0.755267

8000 -0.231781

18000 -0.012827

m17 $ TISSUE, SOFT (ICRU-44) for Tumor, Density (g cm^{-3}) = 1.03

```
1000    -10.5
6000    -25.6
7000    -2.7
8000    -60.2
11000    -0.1
15000    -0.2
16000    -0.3
17000    -0.2
19000    -0.2
[ S u r f a c e ]
$ LUNG(Left)
100  sq  0.00444444  0.02040816  0.001720426  0  0  0  -1  -2  1  21.79084544
101  px  -2
102  pz  21.79084544
$ LUNG(Right)
110  sq  0.00444444  0.02040816  0.001784477  0  0  0  -1  2  1  22.22747566
111  px  2
112  pz  22.22747566
$ Sphere for outside of the heart in the lung(r=5.8cm)
200  s  -2  1  31.5  5.8
$ HEART(r=5.762cm)
210  s  -2  1  31.5  5.748
211  s  -2  1  31.5  4.861  $ Blood inside of the heart
$ SPINE
300  c/z  0  -7.8  2
301  pz  0
302  pz  0.4
303  pz  2.7  $1
304  pz  3.1
305  pz  5.4  $2
306  pz  5.8
307  pz  8.1  $3
308  pz  8.5
309  pz  10.8  $4
310  pz  11.2
311  pz  13.5  $5
312  pz  13.9
313  pz  16.2  $6
```

```
314  pz  16.6
315  pz  18.9  $7
316  pz  19.3
317  pz  21.6  $8
318  pz  22.0
319  pz  24.3  $9
320  pz  24.7
321  pz  27.0  $10
322  pz  27.4
323  pz  29.7  $11
324  pz  30.1
325  pz  32.4  $12
326  pz  32.8
327  pz  35.1  $13
328  pz  35.5
329  pz  37.8  $14
330  pz  38.2
331  pz  40.5  $15
332  pz  40.9
333  pz  43.2  $16
334  pz  43.6
335  pz  45.9  $17
336  pz  46.1
337  pz 47.9  $18
338  pz  48.1
339  pz  49.9  $19
340  pz  50.1
341  pz  51.9  $20 342  pz  52.1
343  pz  53.9  $21 344  pz  54.1
345  pz  55.9  $22
346  pz  56.1
347  pz  57.9  $23 348  pz  58.1
349  pz  59.9  $24 $RIBS; IB12 400  sq  0.00308642  0.010519395  0  0  0  0  -1  0  0.59  0 $inner
401  sq  0.002878115  0.009263368  0  0  0  0  -1  0  0.59  0 $outer
402  pz  15  $313
480  py  -2  $for cutting the rib
$RIB11
403  sq  0.00308642  0.010519395  0  0  0  0  -1  0  0.59  0
```

```
404  sq  0.002878115  0.009263368  0  0  0  0  -1  0  0.59  0
405  pz  17.7  $315
490  py  0.55  $for cutting the rib
$RIB10
406  sq  0.00308642  0.010519395  0  0  0  0  -1  0  0.59  0
407  sq  0.002878115  0.009263368  0  0  0  0  -1  0  0.59  0
408  pz  20.4  $317
$RIB9
409  sq  0.003121945  0.010562685  0  0  0  0  -1  0  0.57  0
410  sq  0.002910096  0.009299134  0  0  0  0  -1  0  0.57  0
411  pz  23.1  $319
$RIB8
412  sq  0.003233681  0.0107944  0  0  0  0  -1  0  0.475  0
413  sq  0.00300726  0.009471883  0  0  0  0  -1  0  0.475  0
414  pz  25.69  $321
$RIB7
415  sq  0.003439128  0.01116243  0  0  0  0  -1  0  0.405  0
416  sq  0.003158999  0.009602272  0  0  0  0  -1  0  0.405  0
417  pz  28.42  $323
$RIB6
418  sq  0.003729807  0.011574473  0  0  0  0  -1  0  0.255  0
419  sq  0.003406266  0.009890901  0  0  0  0  -1  0  0.255  0
420  pz  31.22  $325
$RIB5
421  sq  0.00421031  0.011996607  0  0  0  0  -1  0  0.05  0
422  sq  0.003842857  0.010306888  0  0  0  0  -1  0  0.05  0
423  pz  33.96  $327
$RIB4
424  sq  0.004827003  0.012667331  0  0  0  0  -1  0  -0.235  0
425  sq  0.004401307  0.010930249  0  0  0  0  -1  0  -0.235  0
426  pz  36.64  $329
$RIB3
427  sq  0.006026361  0.013679423  0  0  0  0  -1  0  -0.65  0
428  sq  0.005501892  0.01194422  0  0  0  0  -1  0  -0.65  0
429  pz  39.37  $331 $RIB2
430  sq  0.008361921  0.015431503  0  0  0  0  -1  0  -1.15  0
431  sq  0.007514695  0.013364964  0  0  0  0  -1  0  -1.15  0
432  pz  42.07  $333
```

```
$RIB1
433  sq  0.018032466  0.019837334  0  0  0  0  -1  0  -2.1  0
434  sq  0.015443598  0.016866251  0  0  0  0  -1  0  -2.1  0
435  pz  44.77  $335
$STERNUM
450  sq  0.00444444 0.02040816  0.001609643  0  0  0  -1  0  4  21.8
451  sq  0.00444444  0.02040816  0.001609643  0  0  0  -1  0  3  21.8
452  px  -2
453  px  2
454  pz  25.6
455  pz  46.2
456  py  0
$NECK
500  RCC  0  -6.5  48  0  0  8  5
$SKIN of the Neck
501  RCC  0  -6.5  48  0  0  8  5.2045
$HEAD, FACE
600  sq  0.020408163  0.01384083  0.031956196  0  0  0  -1  0  -2  66.266  $ inner
601  sq  0.015625  0.011080332  0.022998638  0  0  0  -1  0  -2  66.266  $ outer
602  sq  0.020408163  0.01384083  0  0  0  0  -1  0  -2  0  $inner cylinder
603  sq  0.015625  0.011080332  0  0  0  0  -1  0  -2  0  $outer cylinder
604  pz  56
605  pz  66.266
606  py  -0.605
$SKIN of the Head
608  sq  0.01485579  0.010618268  0.021635842  0  0  0  -1  0  -2  66.266  $outer
609  sq  0.01485579  0.010618268  0  0  0  0  -1  0  -2  0  $outer cylinder
610  pz  55.7955
$ARM(Left)
700  RCC  -25.3290  0  -12  0  0  30  4  $Fore
701  RCC  -25.3290  0  18  0  0  30  5  $Upper
$ARM Bone(Left)
702  RCC  -25.3290  0  -12  0  0  30  3  $Fore
703  RCC  -25.3290  0  18  0  0  30  3  $Upper
$ARM(Right)
704  RCC  25.3290  0  -12  0  0  30  4  $Fore
705  RCC  25.3290  0  18  0  0  30  5  $Upper
$ARM Bone(Right)
```

```
706  RCC  25.3290  0  -12  0  0  30  3  $Fore
707  RCC  25.3290  0  18  0  0  30  3  $Upper
$SKIN of Arms
$Fore
708  RCC  -25.3290  0  -12.1290  0  0  30.1290  4.1290  $Left
709  RCC  25.3290  0  -12.1290  0  0  30.1290  4.1290  $Right
$Upper
710  RCC  -25.3290  0  18  0  0  30.1245  5.1245  $Left
711  RCC  25.3290  0  18  0  0  30.1245  5.1245  $Right
$LEG(Left)
800  RCC  -11  0  -103.14  0  0  50.035  8  $Lower
801  RCC  -11  0  -53.105  0  0  50.035  9  $Thigh
$LEG Bone(Left)
802  RCC  -11  0  -103.14  0  0  50.035  5  $Lower
803  RCC  -11  0  -53.105  0  0  50.035  5  $Thigh
$LEG(Right)
804  RCC  11  0  -103.14  0  0  50.035  8  $Lower
805  RCC  11  0  -53.105  0  0  50.035  9  $Thigh
$LEG Bone(Right)
806  RCC  11  0  -103.14  0  0  50.035  5  $Lower
807  RCC  11  0  -53.105  0  0  50.035  5  $Thigh
$SKIN of legs$ Lower
808  RCC  -11  0  -103.269  0  0  50.164  8.1290  $Left
809  RCC  11  0  -103.269  0  0  50.164  8.1290  $Right
$Thigh
810  RCC  -11  0  -53.105  0  0  50.035  9.1245  $Left
81  RCC  11  0  -53.105  0  0  50.035  9.1245  $Right
$ TRUNK
900  sq  0.0025  0.00756144  0  0  0  0  -1  0  0  0
901  pz  -3.07
902  pz  48
$ SKIN of Trunk
903  sq  0.002449649  0.007299523  0  0  0  0  -1  0  0  0
904  pz  -3.2745
905  pz  48.2045
$ Outer boundary
990  so  2000
$tumor
```

```
2222  SPH  -10  3.0  29.75  1
[ C e l l ]
$Lung(Left)
100  4  -0.26  -100  -101  102  200  #3000
$Lung(Right)
101  4  -0.26  -110  111  112  200
$ Heart
200  2  -1.05  -210  211  $heart tissue
201  3  -1.06  -211  $blood
$ Spine
300  15  -1.10  -300  301  -302  $Disc 24
301  14  -1.33  -300  302  -303  $Vertebrae lumbale 5
302  15  -1.10  -300  303  -304  $Disc 23
303  14  -1.33  -300  304  -305  $Vertebrae lumbale 4
304  15  -1.10  -300  305  -306  $Disc 22
305  14  -1.33  -300  306  -307  $Vertebrae lumbale 3
306  15  -1.10  -300  307  -308  $Disc 21
307  14  -1.33  -300  308  -309  $Vertebrae lumbale 2
308  15  -1.10  -300  309  -310  $Disc 20
309  14  -1.33  -300  310  -311  $Vertebrae lumbale 1
310  15  -1.10  -300  311  -312  $Disc 19
311  14  -1.33  -300  312  -313  $Thoracic vertebrae 2
312  15  -1.10  -300  313  -314  $Disc 18
313  14  -1.33  -300  314  -315  $Thoracic vertebrae 11
314  15  -1.10  -300  315  -316  $Disc 17
315  14  -1.33  -300  316  -317  $Thoracic vertebrae 10
316  15  -1.10  -300  317  -318  $Disc 16
317  14  -1.33  -300  318  -319  $Thoracic vertebrae 9
318  15  -1.10  -300  319  -320  $Disc 15
319  14  -1.33  -300  320  -321  $Thoracic vertebrae 8
320  15  -1.10  -300  321  -322  $Disc 14
321  14  -1.33  -300  322  -323  $Thoracic vertebrae 7
322  15  -1.10  -300  323  -324  $Disc 13
323  14  -1.33  -300  324  -325  $Thoracic vertebrae 6
324  15  -1.10  -300  325  -326  $Disc 12
325  14  -1.33  -300  326  -327  $Thoracic vertebrae 5
326  15  -1.10  -300  327  -328  $Disc 11
327  14  -1.33  -300  328  -329  $Thoracic vertebrae 4
```

328 15 -1.10 -300 329 -330 $Disc 10

329 14 -1.33 -300 330 -331 $Thoracic vertebrae 3

330 15 -1.10 -300 331 -332 $Disc 9

331 14 -1.33 -300 332 -333 $Thoracic vertebrae 2

332 15 -1.10 -300 333 -334 $Disc 8

333 14 -1.33 -300 334 -335 $Thoracic vertebrae 1

334 15 -1.10 -300 335 -336 $Disc 7

335 13 -1.42 -300 336 -337 $Cervical vertebrae 7

336 15 -1.10 -300 337 -338 $Disc 6

337 13 -1.42 -300 338 -339 $Cervical vertebrae 6

338 15 -1.10 -300 339 -340 $Disc 5

339 13 -1.42 -300 340 -341 $Cervical vertebrae 5

340 15 -1.10 -300 341 -342 $Disc 4

341 13 -1.42 -300 342 -343 $Cervical vertebrae 4

342 15 -1.10 -300 343 -344 $Disc 3

343 13 -1.42 -300 344 -345 $Cervical vertebrae 3

344 15 -1.10 -300 345 -346 $Disc 2

345 13 -1.42 -300 346 -347 $Cervical vertebrae 2

346 15 -1.10 -300 347 -348 $Disc 1

347 13 -1.42 -300 348 -349 $Cervical vertebrae 1

$ RIB CAGE

400 12 -1.52 300 400 -401 402 -313 -480 $Rib12

401 12 -1.52 300 403 -404 405 -315 -490 $Rib11

402 12 -1.52 300 406 -407 408 -317 $Rib10

403 11 -1.41 300 409 -410 411 -319 $Rib9

404 11 -1.41 300 412 -413 414 -321 $Rib8

405 11 -1.41 300 415 -416 417 -323 $Rib7

406 11 -1.41 300 418 -419 420 -325 $Rib6

407 11 -1.41 300 421 -422 423 -327 $Rib5

408 11 -1.41 300 424 -425 426 -329 $Rib4

409 11 -1.41 300 427 -428 429 -331 $Rib3

410 11 -1.41 300 430 -431 432 -333 $Rib2

411 11 -1.41 300 433 -434 435 -335 $Rib1

$ STERNUM

450 11 -1.41 -450 451 452 -453 454 -455 456

$ NECK

500 1 -1.03 -500 #335 #336 #337 #338 #339 #340 #341 #342 #343 #344 #345 #346 #347

501 6 -1.09 500 -501 $Neck skin

```
$ HEAD-FACE
600  7  -1.61  600  -601  $SKULL
601  5  -1.04  -600  $ Brain
602  10  -1.68  602  -603  -605  604  606  #600 $ Facial bone
603  1  -1.03  -603  -605  604  #600 #601 #602 #344 #345 #346 #347 $Soft tissue
604  6  -1.09  -608  601  605  $ Head skin
605  6  -1.09  -609  603  604  -605  $ Face skin
606  6  -1.09  -609  -604  610  #344 #345 #346 #347 #500 #501 $Lower face skin
$ ARMS,LEGS
$ ARMS
700  1  -1.03  -700  702  $ Lower Left arm soft tissue
701  1  -1.03  -701  703  $ Upper Left arm soft tissue
702  9  -1.46  -702  $ Lower Left arm bone
703  9  -1.46  -703  $ Upper Left arm bone
704  1  -1.03  -704  706  $ Lower Right arm soft tissue
705  1  -1.03  -705  707  $ Upper Right arm soft tissue
706  9  -1.46  -706  $ Lower Right arm bone
707  9  -1.46  -707  $ Upper Right arm bone
$ Skin of arms
708  6  -1.09  700  -708  $Lower, left
709  6  -1.09  704  -709  $Lower, right
710  6  -1.09  701  -710  $Upper, left
711  6  -1.09  705  -711  $Upper, right
$ LEGS
800  1  -1.03  -800  802  $ Lower Left leg soft tissue
801  1  -1.03  -801  803  $ Upper Left leg soft tissue
802  8  -1.33  -802  $ Lowr Left leg bone
803  8  -1.33  -803  $ Upper Left leg bone
804  1  -1.03  -804  806  $ Lower Right leg soft tissue
805  1  -1.03  -805  807  $ Upper Right leg soft tissue
806  8  -1.33  -806  $ Lower Right leg bone
807  8  -1.33  -807  $ Upper Right leg bone
$ Skin of legs
808  6  -1.09  800  -808  $Lower, left
809  6  -1.09  804  -809  $Lower, right
810  6  -1.09  801  -810  $Upper, left
811  6  -1.09  805  -811  $Upper, right
$ TRUNK
```

```
900   1   -1.03   -900   901   -902   #100 #101 #200 #201 #300 #301 #302 #303 #304 #305 #306 #307 #308 #309
#310 #311 #312 #313 #314 #315 #316 #317 #318 #319 #320 #321 #322 #323 #324 #325 #326 #327 #328 #329
#330 #331 #332 #333 #334 #335 #336 #337 #338 #339 #340 #341 #342 #343 #344 #345 #346 #347 #400 #401
#402 #403 #404 #405 #406 #407 #408 #409 #410 #411 #450
$ Skin of trunk
901   6   -1.09   900   -903   901   -902
902   6   -1.09   -903   904   -901   #801 #803 #805 #807 #810 #811
903   6   -1.09   -903   902   -905   #344 #345 #346 #347 #500 #501
$tumor
3000   17   -1.03   -2222
$ Vaccuum (Or the Air)
990   0   -990   #100 #101 #200 #201 #300 #301 #302 #303 #304 #305 #306 #307 #308 #309 #310 #311 #312
#313 #314 #315 #316 #317 #318 #319 #320 #321 #322 #323 #324 #325 #326 #327 #328 #329 #330 #331 #332
#333 #334 #335 #336 #337 #338 #339 #340 #341 #342 #343 #344 #345 #346 #347 #400 #401 #402 #403 #404
#405 #406 #407 #408 #409 #410 #411 #450 #500 #501 #600 #601 #602 #603 #604 #605 #606 #700 #701 #702
#703 #704 #705 #706 #707 #708 #709 #710 #711 #800 #801 #802 #803 #804 #805 #806 #807 #808 #809 #810
#811 #900 #901 #902 #903 #3000
$ Outer universe
999   -1   #990
[ T - D e p o s i t ]
title = Deposit in xyz mesh
mesh = xyz
x-type = 2
xmin = -30.0
xmax = 30.0
nx = 600
y-type = 2
ymin = -15.0
ymax = 15.0
ny = 300
z-type = 2
zmin = 25.0
zmax = 35.0
nz = 100
unit = 0
2D-type = 3
axis = z
file = deposit.out
```

material = all

output = dose

epsout = 0

gshow = 1

[T - P r o d u c t]

title = N13 production in xyz mesh

mesh = xyz

x-type = 2

xmin = -30.0

xmax = 30.0

nx = 600

y-type = 2

ymin = -15.0

ymax = 15.0

ny = 300

z-type = 2

zmin = 25.0

zmax = 35.0

nz = 100

e-type = 1

ne = 1

0.0 20.0

material = all

mother = all

unit = 1

2D-type = 3

axis = z

file = N13.out

output = nuclear

part = 13N

epsout = 0

[E n d]

A.4 PeakCalib

The PeakCalib is a standalone open-source computer program that performs linear and non-linear cubic spline interpolation of the obtained data from PHITS Monte Carlo package. PeakCalib software and source code (mentioned to the last paragraph of this section) can be downloaded from: `https://`

`figshare.com/articles/software/Studies_on_proton_range_monitoring_by_utilizing_13N_peak_for_proton_therapy_applications/16635697/2`. The program reads the input data obtained from the MC model with incident proton energy interval of 5 MeV. All data used in the fitting function were obtained from PHITS simulation package. The proposed fitting function can be used for data extraction. The incident energy range and increment chosen in present fitting function covers most widely reported proton irradiation facilities. It uses two different interpolation techniques to reconstruct data with incident proton energy interval of 0.1 MeV. The linear interpolation uses linear polynomial to generate new set of data points in between known sets of data as;

$$d_{offset} = \frac{d_0(E_1 - E_{inp}) + d_1(E_{inp} - E_0)}{E_1 - E_o} \tag{A.1}$$

where d_{offset}, d_0 and d_1 are the new offset distance, offset distance of preceding and following points, respectively. Similarly, E_{inp}, E_0 and E_1 are the user input incident proton energy, energy of preceding and following points, respectively. Considering the cubic spline interpolation, the value of function $f(x)$ are calculated in n base points. Furthermore, the coefficient for the cubic spline interpolation (i.e., spline coefficients) are computed. Then spline interpolation would be performed based on the obtained coefficient for the set of base points. Since the polynomial used here is cubic, there will be three coefficients that needs to be determined that are; $b(i)$, $c(i)$ and $d(i)$ which i = 1,2,3,...,n. The following function shown in Eq. (A2) has been used in the present spline interpolation;

$$s(x) = y(i) + b(i) \times (x - x(i)) + c(i) \times (x - x(i))^2 + d(i) \times (x - x(i))^3 \tag{A.2}$$

The results of linear and non-linear cubic spline fitting of distance offset for various incident proton energies are shown in Fig. A1. From the results shown in Fig. A1, the linear and non-linear trend of fitting the Monte Carlo data can be clearly seen. Employing both of these interpolation techniques would help further increase the precision and accuracy of the estimated peak offset distances.

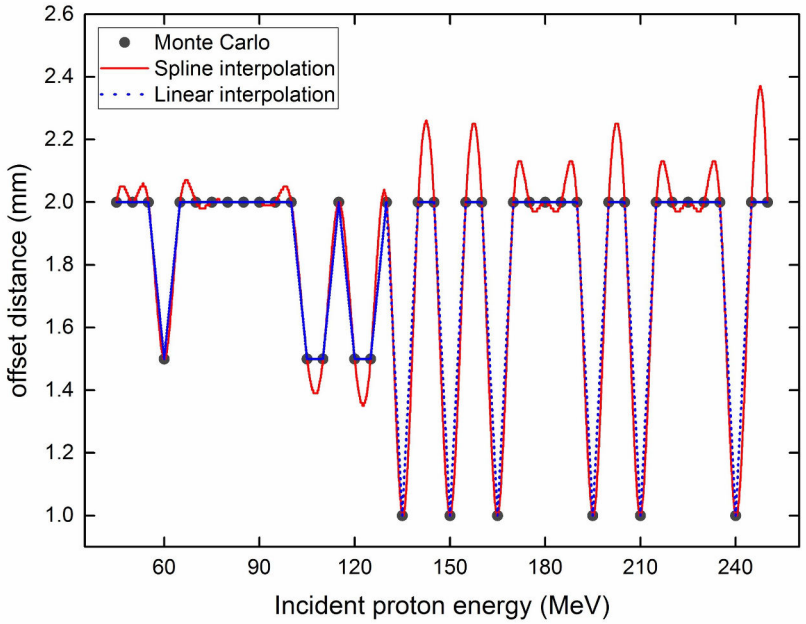

Figure A.1: Linear and spline interpolation of Monte Carlo data for ^{13}N and Bragg-peak offset distance.

FORTRAN Code:

```
program peakcalib
integer, parameter :: n=47 !base points for interpolation
double precision, dimension(n) :: E
double precision, dimension(n) :: brgg
double precision, dimension(n) :: n13
double precision, dimension(n) :: ffst
double precision :: en
integer, parameter :: nint=2301 !compute interpolation in nint points
double precision :: xmin !given interval of x()
double precision :: xmax
double precision, dimension (n) :: xi(n)
double precision, dimension (n) :: yi(n)
double precision, dimension (n) :: b(n)
double precision, dimension (n) :: c(n)
double precision, dimension (n) :: d(n)
double precision, dimension(nint) :: xl(nint)
double precision, dimension(nint) :: yl(nint)
double precision :: x
double precision :: y
double precision :: step
double precision :: ys(nint)
integer :: i
double precision :: ispline
real*4, dimension(nint) :: eng
real*4, dimension(nint) ::loff
real*4, dimension(nint) ::soff
character(256) :: banner
integer :: lop
open(10,file='offset_data.dat')
open(20,file='inp.tmp')
do i =1,47
read(20,*) E(i),brgg(i),n13(i)
!print*, depth(i),brgg(i),n13(i)
end do
do i =1,47
!read(20,*) depth(i),brgg(i),n13(i)
ffst(i) = abs(brgg(i)-n13(i)) !stricly speaking abs is needed
!print*, depth(i)
end do
!do i =1,47
!read(20,*) depth(i),brgg(i),n13(i)
!print*, depth(i),brgg(i),n13(i),ffst(i)
!end do
xmin = minval(E) !20.0
xmax = maxval(E) !30.0
print*, " "
```

```
print*, "****************************************"
print*, "****************************************"
print*, " "
print*, " N-13 peak to Bragg-peak calibration program "
print*, " "
print*, "****************************************"
print*, "****************************************"
print*, " "
write(*,777) "minimum energy: ",xmin, " MeV"
write(*,777) "minimum energy: ",xmax, " MeV"
777 format (A,X,f6.2,X,A)
write(*,778) "Energy interval: 0.1 MeV"
778 format(A)
22 print*, " "
print*, "Enter incident proton energy (MeV): "
read*, en
!generate xi and yi from f(x), xmin, xmax, n
step = (xmax-xmin)/(n-1)
do i=1,n
xi(i) = E(i) !xmin + step*float(i-1)
yi(i) = ffst(i) !f(xi(i))
! write (*,200) xi(i), yi(i)
end do
!here we calculate spline coeficients cubic function
call spline (xi, yi, b, c, d,n)
!interpolation for nint (can be changed) points
step = (xmax-xmin)/(nint-1)
do i=1, nint
x = xmin + step*float(i-1)
ys(i) = ispline(x, xi, yi, b, c, d, n)
!if(en==x)then
!write (10,200) x, ys(i) !, error
!end if
end do
!200 format (3f12.5)
!the new x-grid data
do i=1,nint
xl(i) = xmin + step*float(i-1)
end do
call lintp(xi,yi,xl,yl,n,nint)
!the title comment section
write(10,222) "Energy","spline","linear"
222 format(A,2X,A,2X,A)
do i=1,nint
!print*, xl(i), yl(i)
write (10,200) xl(i), ys(i), yl(i)
200 format (f6.1,X,f6.2,X,f6.2)
```

```
print*,xl(i), ys(i), yl(i)
#pause
!write(10,*) xl(i), yl(i)
end do
close(10)
open(11,file='offset_data.dat')
read(11,*) banner
do i=1,nint
read(11,*) eng(i), soff(i), loff(i)
!210 format (f6.1,X,f6.2,X,f6.2)
!print*, eng(i), soff(i), loff(i)
end do
en = AINT(en * 1000.0 + 0.5) / 1000.0
print*, " "
print*, "—The results:"
lop = 1
do i=1,nint
eng(i) = AINT(eng(i) * 1000.0 + 0.5) / 1000.0
!print*, eng(i)
if(en>(eng(i)-1E-4).AND.en<(eng(i)+1E-4))then
write(*,211) "Energy(MeV):",eng(i),"|", "spline peak(mm):",soff(i),"|","linear peak(mm):", loff(i)
211 format (X,A,f6.1,X,A,2X,A,f6.2,X,A,2X,A,f6.2)
lop = lop +1
else if(lop==1.AND.i==nint)then
33 write(*,779) "no results for this energy, make sure you have 0.1 MeV interval"
779 format(A)
end if
end do
!if(i==nint)then
!goto 33
!print*, eng(i), soff(i), loff(i)
!end if
!print*, en
!print*, xl(kl), ys(kl), yl(kl)
!if(xl(i)==en)then
!kl = i
!end if
!do i = 1,3
!if(en==E(i))then
!print*, ffst(i)
!end if
!end do
close(11)
close(20)
goto 22
end program peakcalib
subroutine lintp(xi,yi,xl,yl,n,nint)
```

```
implicit none
integer n
integer i
integer j
integer nint
double precision :: xi(n)
double precision :: yi(n)
double precision :: xl(nint)
double precision :: yl(nint)
double precision :: x0
double precision :: y0
double precision :: x1
double precision :: y1
do j=1,nint
do i=1,n
if(xl(j).ne.xi(i))then
if(xl(j) > xi(i).AND. xl(j) < xi(i+1))then
x0=xi(i)
y0=yi(i)
x1=xi(i+1)
y1=yi(i+1)
yl(j) = ( y0*(x1-xl(j)) + y1 *(xl(j)-x0) )/(x1-x0)
end if
else
yl(j) = yi(i)
end if
end do
end do
end subroutine lintp
subroutine spline (x, y, b, c, d, n)
implicit none
integer :: n
double precision :: x(n)
double precision :: y(n)
double precision :: b(n)
double precision :: c(n)
double precision :: d(n)
integer :: i
integer :: j
integer :: gap
double precision :: h
gap = n-1
if ( n < 2 ) return
if ( n < 3 ) then
b(1) = (y(2)-y(1))/(x(2)-x(1)) ! linear interpolation
c(1) = 0.
d(1) = 0.
```

```
b(2) = b(1)
c(2) = 0.
d(2) = 0.
return
end if
d(1) = x(2) - x(1)
c(2) = (y(2) - y(1))/d(1)
do i = 2, gap
d(i) = x(i+1) - x(i)
b(i) = 2.0*(d(i-1) + d(i))
c(i+1) = (y(i+1) - y(i))/d(i)
c(i) = c(i+1) - c(i)
end do
b(1) = -d(1)
b(n) = -d(n-1)
c(1) = 0.0
c(n) = 0.0
if(n /= 3) then
c(1) = c(3)/(x(4)-x(2)) - c(2)/(x(3)-x(1))
c(n) = c(n-1)/(x(n)-x(n-2)) - c(n-2)/(x(n-1)-x(n-3))
c(1) = c(1)*d(1)**2/(x(4)-x(1))
c(n) = -c(n)*d(n-1)**2/(x(n)-x(n-3))
end if
do i = 2, n
h = d(i-1)/b(i-1)
b(i) = b(i) - h*d(i-1)
c(i) = c(i) - h*c(i-1)
end do
c(n) = c(n)/b(n)
do j = 1, gap
i = n-j
c(i) = (c(i) - d(i)*c(i+1))/b(i)
end do
b(n) = (y(n) - y(gap))/d(gap) + d(gap)*(c(gap) + 2.0*c(n))
do i = 1, gap
b(i) = (y(i+1) - y(i))/d(i) - d(i)*(c(i+1) + 2.0*c(i))
d(i) = (c(i+1) - c(i))/d(i)
c(i) = 3.*c(i)
end do
c(n) = 3.0*c(n)
d(n) = d(n-1)
end subroutine spline
function ispline(u, x, y, b, c, d, n)
implicit none
double precision :: ispline
integer :: n
double precision :: u
```

```
double precision :: x(n)
double precision :: y(n)
double precision :: b(n)
double precision :: c(n)
double precision :: d(n)
integer :: i
integer :: j
integer :: k
double precision :: dx
!the boundary value
if(u <= x(1)) then
ispline = y(1)
return
end if
if(u >= x(n)) then
ispline = y(n)
return
end if
i = 1
j = n+1
do while (j > i+1)
k = (i+j)/2
if(u < x(k)) then
j=k
else
i=k
end if
end do
dx = u - x(i)
ispline = y(i) + dx*(b(i) + dx*(c(i) + dx*d(i)))
end function ispline
```

A.5 Scripts

All data available in the link `https://figshare.com/articles/software/Studies_on_proton_range_monitoring_by_utilizing_13N_peak_for_proton_therapy_applications/16635697/2`.

SA scripts

```
#!/usr/bin/env python3
#Id
#Spectral Analysis for PEM image
from pybld import *
```

```
import sys
from scipy import optimize
import optparse
#import calc_a
bld = PYBLD()
def spectral_analysis(A2,tac,lbeta1):
ans2_2 = optimize.nnls(A2,tac)[0]
clbeta1_2 = compress(ans2_2,lbeta1) #remove 0 def spectral_analysis(A2,tac,lbeta1):
ans2_2 = optimize.nnls(A2,tac)[0]
clbeta1_2 = compress(ans2_2,lbeta1) #remove 0
cans2_2 = compress(ans2_2,ans2_2)
alpha_beta_2 = cans2_2/clbeta1_2
aindex_2 = argsort(alpha_beta_2)[::-1] #sort
alpha_2 = cans2_2[aindex_2]
beta_2 = clbeta1_2[aindex_2]
return alpha_2,beta_2
if __name__ == '__main__':
option_parser = optparse.OptionParser()
option_parser.add_option('–input',help='Dynamic Analyze file for Input',type='str',default='')
option_parser.add_option('–time',help='Time info file (start end in sec)',type='str',default='')
option_parser.add_option('–output',help='Time info file (start end in sec)',type='str',default='')
option_parser.add_option('–mask',help='Mask image',type='str',default='')
option_parser.add_option('–debug',help='Debug option 1',type='int',default=0)
option_parser.add_option('–nbeta',help='No of Beta 1000',type='int',default=1000)
option_parser.add_option('–betamax',help='Max Beta 0.1',type='float',default=0.1)
option_parser.add_option('–betamin',help='Min Beta 1E-4',type='float',default=1e-4)
option_parser.add_option('–betacut',help='Cut-off for Beta',type='float',default=0)
option_parser.add_option('–thresh',help='Threshold to remove background Default 1.5.
betamin*threshold',type='float',default=1.5)
option_parser.add_option('–athresh',help='Absolute Threshold to remove background. If athresh is
set, thresh option is ignored',type='float',default=0)
options,args = option_parser.parse_args()
if len(sys.argv)==1:
option_parser.print_help()
bld.exit()
if len(options.input)==0:
print("please give input image by –input")
bld.exit()
```

```
if len(options.time)==0:
print("please give time info file by –time")
bld.exit()
if len(options.output)==0:
print("please give output image file by –output")
bld.exit()
img = bld.img()
img.read(options.input)
oimg = bld.img()
oimg.hdr = img.hdr()
oimg.hdr.dim[4] = 1
oimg.zeros()
stime,etime = bld.input(options.time)
mtime = stime + (etime - stime)*0.5
#make input of bolus
fatm = arange(0,max(etime),1,dtype='float')
fainp = zeros(fatm.shape,dtype='float')
fainp[0] = 1.0
xdim = img.hdr.dim[1]
ydim = img.hdr.dim[2]
zdim = img.hdr.dim[3]
tdim = img.hdr.dim[4]
if tdim!=len(mtime):
print("No of Frames and Time frames are different!\n")
bld.exit()
nbeta = options.nbeta
betamax = options.betamax
betamin = options.betamin
thresh = options.thresh
athresh = options.athresh
mask_flag = 0
if len(options.mask)!=0:
mask = bld.img()
mask.read(options.mask)
mask_flag = 1
no_basis_functions = nbeta
theta4min = betamin #1e-4
theta4max = betamax
```

```
beta1=arange(log(theta4min),log(theta4max),(log(theta4max)-log(theta4min))/(no_basis_functions))
if len(beta1)!=no_basis_functions:
beta1 = beta1[0:no_basis_functions]
lbeta1=exp(beta1);
no_frame = tdim
#A2 = calc_a.pass_src(lbeta1,mtime,fatm,fainp);
A2=ones((no_frame,no_basis_functions),dtype='float64');
for i in range(no_basis_functions):
vec1=bld.conv_exp(mtime,array([1.0,lbeta1[i]]),fatm,fainp)
A2[:,i] = vec1[:]
for iz in range(zdim):
for iy in range(ydim):
for ix in range(xdim):
if mask_flag==1:
if mask.img[iz,iy,ix]==0:
continue
tac = img.img[:,iz,iy,ix]
if options.debug==1:
print("x,y,z = ",ix,iy,iz)
alpha,beta = spectral_analysis(A2,tac,lbeta1)
#print(tac,alpha,beta)
if athresh>0:
if len(beta)==1 and beta[0]<athresh:
v = 0.0
else:
if options.betacut>0:
beta = less(beta,options.betacut)*beta
beta = greater(beta,athresh)*beta
v = sum(alpha*beta)
else:
if len(beta)==1 and beta[0]<thresh*betamin:
v = 0.0
else:
if options.betacut>0:
beta = less(beta,options.betacut)*beta
v = sum(alpha*beta)
oimg.img[iz,iy,ix] = v
#print(ix,iy,iz)
```

```
if options.debug==1:
print("#sum of alpha*beta %g" % v)
print("#beta,halflife(min),alpha")
sbeta = beta[argsort(-beta)]
salpha = alpha[argsort(-beta)]
for j in range(len(beta)):
if sbeta[j]!=0:
print(sbeta[j],log(2)/sbeta[j]/60.0,salpha[j])
#print(alpha,beta,v,len(beta),beta[0]) #sum(alpha*beta))
oimg.write(options.output)
```

3D plot scripts

```
#!/usr/bin/env python3
# Import libraries
from pybld import *
import sys
import matplotlib.pyplot as plt
from mpl_toolkits.mplot3d import Axes3D
import matplotlib as mpl
bld = PYBLD()
fig = plt.figure(figsize = (4, 2))
ax = fig.add_subplot(111, projection='3d')
if len(sys.argv)!=3:
print("usage:%s image threshold (%%)" % (sys.argv[0]))
bld.exit()
img = bld.img()
img.read(sys.argv[1])
xdim = img.hdr.dim[1]
ydim = img.hdr.dim[2]
zdim = img.hdr.dim[3]
px = img.hdr.pixdim[1]
py = img.hdr.pixdim[2]
pz = img.hdr.pixdim[3]
thresh = float(sys.argv[2])*0.01
mask = greater(img.img,img.img.max()*thresh)
X = []
Y = []
```

```
Z = []
dat = []
for iz in range(zdim):
for iy in range(ydim):
for ix in range(xdim):
if mask[iz,iy,ix]>0:
X.append(ix*px)
Y.append(iy*py)
Z.append(iz*pz)
dat.append(img.img[iz,iy,ix])
X = array(X)
Y = array(Y)
Z = array(Z)
adat = array(dat)
ax.set_xlim(0,60)
ax.set_ylim(-10,30)
ax.set_zlim(-10,30)
sctt= ax.scatter(X,Y,Z,c=adat,cmap='hot',s=1)
plt.title("3D scatter plot of SA_$ \mathregular^{15}O $", fontweight ='bold')
ax.set_xlabel('Depth (mm)', fontweight ='bold')
ax.set_ylabel('Lateral x (mm)', fontweight ='bold')
ax.set_zlabel('Lateral y (mm)', fontweight ='bold')
ax.set_facecolor('white')
ax.view_init(14, -60)
cb = plt.colorbar(sctt, pad=0.15, shrink = 0.8, aspect = 10)
cb.set_ticks([0,100])
cb.set_ticklabels(["min", "max(%)"])
plt.savefig('3D Scatter Plot.png')
plt.show()
for angle in range(0, 360):
ax.view_init(14, angle)
plt.draw()
plt.pause(.001)
```

Appendix B

Research achievements

B.1 Journal papers

1. **Md. Rafiqul Islam**, Mehrdad Shahmohammadi Beni, Akihito Inamura, Nursel Safakatti, Masayasu Miyake, Mahabubur Rahman, A.K.F. Haque, Shigeki Ito, Shinichi Gotoh, Taiga Yamaya, and Hiroshi Watabe. "A feasibility study on proton range monitoring using N-13 peak in inhomogeneous targets." *Tomography*. (Submitted).

2. Mehrdad Shahmohammadi Beni, Hiroshi Watabe, Wing Sum Kwan, **Md. Rafiqul Islam**, and Kwan Ngok Yu. "RadStat: An open-source statistical analysis tool for counts obtained by a GM counter." *PloS one*, **2022**, 17 (5), e0267610. (http://dx.doi.org/10.1371/journal.pone.0267610)

3. Mehrdad Shahmohammadi Beni, Kwan Ngok Yu, **Md. Rafiqul Islam**, and Hiroshi Watabe. "Development of PHITS graphical user interface for simulation of positron emitting radioisotopes production in common biological materials during proton therapy." *Journal of Radiation Research*, **2022**, 63 (3), 385-392. (http://dx.doi.org/10.1093/jrr/rrac010)

4. **Md. Rafiqul Islam**, Mehrdad Shahmohammadi Beni, Shigeki Ito, Shinichi Gotoh, Taiga Yamaya, and Hiroshi Watabe. "An analysis scheme for 3D visualization of positron emitting radioisotopes using positron emission mammography system." *Applied Sciences*, **2022**, 12 (2), 823. (https://doi.org/10.3390/app12020823)

5. **Md. Rafiqul Islam**, Mehrdad Shahmohammadi Beni, Chor-yi Ng, Masayasu Miyake, Mahabubur Rahman, Shigeki Ito, Shinichi Gotoh, Taiga Yamaya, and Hiroshi Watabe. "Proton range monitoring using N-13 peak for proton therapy applications." *PloS one*, **2022**, 17 (2), e0263521. (https://doi.org/10.1371/journal.pone.0263521)

6. **Md. Rafiqul Islam**, Hiroshi Watabe, and Andreoli Stefano. "Measurement and comparison of output factors using two detectors for NOVAC7 intraOperative radiotherapy accelerator." *International Journal of Medical Physics, Clinical Engineering and Radiation Oncology*, **2022**, 9 (2), 52-61. (`https://doi.org/10.4236/ijmpcero.2020.92006`)

B.2 Conference abstracts and presentations

1. **Md. Rafiqul Islam**, Masayasu Miyake, Mahabubur Rahman, Shigeki Ito, Shinichi Gotoh, Hiroshi Watabe. Spectral Analysis technique to extract N-13 distribution from in-bean PET images for range verification in proton therapy. *IEEE-NSS-MIC*; 16-23 October 2021, Yokohama, Japan. (Online oral presentation)

2. **Md. Rafiqul Islam**, Masayasu Miyake, Mahabubur Rahman, Shigeki Ito, Shinichi Gotoh, TaigaYamaya, Hiroshi Watabe. Extraction of 3D N-13 distribution in inhomogeneous phantom by Spectral Analysis technique for proton therapy verification. *National conference on Physics-2021*; 6-7 August 2021, Bangladesh Physical Society, Dhaka, Bangladesh. (Online oral presentation)

3. **Md. Rafiqul Islam**, Masayasu Miyake, Mahabubur Rahman, Shigeki Ito, Shinichi Gotoh, Hiroshi Watabe. "Bragg peak verification in proton beam therapy with PEM." *121-st Scientific Meeting of the Japan Society of Medical Physics (JSMP121)*; 15–18 April 2021, Yokohama, Japan. (Online oral presentation)

4. **Md. Rafiqul Islam**, Hiroshi Watabe, Andreoli Stefano. "Measurement and comparison of output factors using two detectors for NOVAC7 intraOperative radiotherapy accelerator." *19-th International Conference on Solid State Dosimetry (SSD19)*; 15-20 September 2019, Hiroshima, Japan. (Poster presentation)